University of Puerto Rico

Faculty of Natural Sciences

Department of Environmental Sciences

Rio Piedras, Puerto Rico

African Dust Days across the Northeast Caribbean:
An Analysis of Enhanced Transport, Microphysical Properties, and Atmospheric Thermodynamics

by

Odalys Martínez-Sánchez

A Dissertation Submitted in Partial

Fulfillment of the Requirements

For the Degree of

Doctor of Philosophy

May 2020

ACCEPTED BY THE FACULTY OF

THE DEPARTMENT OF ENVIRONMENTAL SCIENCES

OF THE UNIVERSITY OF PUERTO RICO

IN PARTIAL FULFILLMENT OF

THE REQUIREMENTS FOR THE DEGREE OF

DOCTOR OF PHILOSOPHY

DR. OLGA L. MAYOL BRACERO	_____
Name of Advisor	Signature
DR. ANDREW HEYMSFIELD	_____
Committee Member	Signature
DR. CARLOS U. PABON-ORTIZ	_____
Committee Member	Signature
DR. RAFAEL A. RIOS	_____
Committee Member	Signature
DR. JORGE R. ORTIZ ZAYAS	_____
Committee Member	Signature
DR. ELIZABETH DVORSKY	_____
Chairman	Signature

May 2020

Odalys Martínez-Sánchez
© All rights reserved

Dedication

To my dad whom taught me perseverance,
to my mom whom taught me discipline,
to my beloved husband for his unconditional love and support,
and to my grandpa whom unknowingly instilled the scientific curiosity
the day he showed me the Great Comet of 1997.

Acknowledgments

I would like to express my special appreciation and thanks to my advisor Professor Dr. Olga L. Mayol-Bracero. She allowed me to be part of her research team, although I never was the traditional full-time Ph. D. student. She contributed to a rewarding graduate school experience by giving me intellectual freedom, supporting my attendance at various conferences, engaging me in new ideas, and demanding a high quality of work. A very special thanks to Professor Dr. Carlos U. Pabón-Ortiz and the former Meteorologist in Charge of the National Weather Service Israel Matos for all the advice, ideas, moral support, and patience throughout my undergraduate and early career stages which are the foundation of this research. My gratitude to the rest of my dissertation committee, Dr. Andy Heymsfield, Professor Dr. Jorge Ortiz, and Professor Dr. Rafael Ríos, for their interest in my work, insightful comments, and encouragement. I would also like to express my deepest gratitude to Dr. Emilio Cuevas-Agulló and Dr. Rosa García Cabrera for their advice and guidance, which have been extremely important during the final stages of this journey.

A special thanks to my parents, brothers, sisters-in-law, and grandma, all of you were always there to support me. Love You All. To my beloved husband, I cannot thank you enough for encouraging me every single day. I would like to recognize the invaluable support that all my coworkers at WFO SJU gave me as well, my deepest thanks. Finally, I thank God for giving me the strength, knowledge, ability, and opportunity to undertake this research study and to persevere and complete it satisfactorily.

Biographical Sketch

Odalys Martínez Sánchez was born on November 23rd, 1983, in Arecibo, Puerto Rico (PR). She is the oldest daughter of Marisol Sánchez Rivera and Edgardo Martínez Gerena. In May 2001, Odalys earned her high school diploma from Colegio de La Inmaculada Concepcion in Manatí, PR, showing interest and mastery in science and mathematics from a very young age. She began undergraduate studies at the University of Puerto Rico, Mayagüez Campus, in August 2001 after being accepted in the College of Natural Sciences. As an undergraduate student from the Theoretical Physics Department, Odalys participated in two internships that defined her career and modeled her future. She was a summer intern at the National Weather Service Forecast Office in San Juan, PR (WFO SJU), during the year 2004, followed by a second internship at Isla de Magueyes Research Station, Lajas, PR. During her internship at the WFO SJU, she learned about operational meteorology and hydrology. The following year, her internship focused on atmospheric aerosols and African dust. Her love for operational meteorology and atmospheric sciences led her to apply to a full-time position as a Met Intern at the WFO SJU after completing the requirements for a degree in Theoretical Physics with a minor in Meteorology and Atmospheric Sciences. In October 2008, she began to work as a full-time employee at the WFO SJU, being the first female to reach a supervisory position in April 2013. As a full-time employee, she decided to pursue a Ph.D. in Environmental Sciences and joined the Atmospheric Chemistry and Aerosol Research (ACAR) group of Dr. Olga L. Mayol-Bracero. Her research work and platform provided by the WFO SJU allowed her to develop new knowledge through collaboration with the local and international scientific community.

Abstract

Although field campaigns have been conducted to improve the understanding of African dust across the Caribbean, there are still fundamental unanswered questions regarding frequency and magnitude over the Puerto Rico area, which is located at the north edge of the dust corridor. This study aims to identify the African Dust Days (ADD) across Puerto Rico between 2004 and 2018; to assess trends in the frequency and magnitude during June, July, and August (JJA) when the strong seasonal cycle of dust transport into the Caribbean is observed; to show how the intra-seasonal variations of dust transport into the northeast Caribbean is modulated by the North African Dipole Intensity (NAFDI) index, and to identify impacts on rainfall patterns.

A day was classified as ADD if the Aerosol Optical Depth (AOD) was equal to or greater than 0.20 combined with an Extinction Ångström Exponent equal to or lower than 0.60. These optical properties were retrieved from the AErosol RObotic NETwork at Cape San Juan and La Parguera, Puerto Rico. The frequency of ADD was the number of ADD divided by the total number of observations. The magnitude was the mean AOD during ADD. The AOD monthly anomaly, which was calculated as well, was then correlated with the NAFDI index to determine if the NAFDI index modulates the AOD anomaly.

A total of 674 days was identified as ADD between 2004 and 2018, with 505 of them observed during JJA (75%). Although no quantifiable trend in the frequency or magnitude of ADD is observed, data suggest that the NAFDI index modulates the intra-seasonal variation in dust transport into the northeast Caribbean and associated AOD anomaly. Meteorological data retrieved at the Weather Service Forecast Office in San Juan, Puerto Rico, during the days classified as ADD also suggest that rainfall activity occurs if the static energy values are equal to or greater than 334 kJ kg^{-1} combined with mixing ratio values equal to or greater than 12 g kg^{-1} at 850 mb.

Table of Contents

Chapter 1 INTRODUCTION: STATE OF KNOWLEDGE ……1

1.1 Aerosols ……1

1.1.1 Atmospheric Aerosols Particles ……...1

1.1.2 Atmospheric Aerosols Particles and their Impacts on Weather and Climate ……...2

1.2 Aerosol Physical Properties ……...4

1.3 Aerosol Optical Properties ……5

1.4 African Mineral Dust ……...8

1.4.1 Dust Sources ……...8

1.4.2 Dust Mobilization ……9

1.4.3 Dust Emission, Transport, and the Saharan Air Layer ……10

1.4.4 Dust Seasonal Patterns ……12

1.4.5 Enhanced Dust Transport ……13

1.5 Dust as Cloud Condensation Nuclei and Ice Nuclei ……16

1.6 Rainfall Patterns and the Standardized Precipitation Index ……17

1.7 African Dust across the Caribbean ……...18

1.8 Statement of the Problem and Intellectual Merit ……23

1.9 Thesis Outline ……25

Chapter 2 EXPERIMENTAL DESIGN ……26

2.1 Assessment of Aerosol Optical Properties across the Northeast Caribbean ….26

2.1.1 Software and Models ……26

2.1.1.a Igor Pro ® ……26

2.1.2 Instrumentation Platforms ……26

2.1.2.a AErosol RObotic NETwork ……26

2.1.2.b MODerate Resolution Imaging Spectroradiometer ……28

2.1.2.c Meteorological Soundings ……29

2.1.3 Sampling Strategy ……30

2.1.4 Statistical Analysis for the Aerosol Optical Properties across the Northeast Caribbean ……33

2.2 African Dust Days ……35

2.2.1 Software and Models ……35

2.2.1.a Igor Pro ® ……35

2.2.1.b Hybrid Single-Particle Lagrangian Integrated Trajectory (HYSPLIT) ……35

2.2.2 Frequency and Magnitude of African Dust Days ……35

2.3 Enhanced Dust Transport into the Northeast Caribbean Basin ……37

2.3.1 Software and Models ……37

2.3.1.a Igor Pro ® ……37

2.3.1.b National Center for Environmental Prediction (NCEP) and National Center for Atmospheric Research (NCAR) Reanalysis Tool ……37

2.3.2 The North African Dipole Intensity Index and the Caribbean Dustiness ……37

2.4 Dust as Cloud Condensation Nuclei ……...39

2.4.1 Software and Models …….……39

2.4.1.a Igor Pro® …….……...39

2.4.1.b Hybrid Single-Particle Lagrangian Integrated Trajectory (HYSPLIT) …….……...39

2.4.2 Instrumentation Platforms: Ice in Clouds -Tropical ….……39

2.4.2.a Aerosol Particle Counters and Sizers ……..…..……40

2.4.2.a.i Aerosol Particle Spectrometer with Polarization Detection ……41

2.4.2.a.ii High-flow Dual Channel Differential Mobility Analyzer …….……42

2.4.2.b Nuclei Counters …….…….……43

2.4.2.b.i Cloud Condensation Nuclei Counter …….……43

2.4.2.b.ii Continuous Flow Diffusion Chamber ……..…44

2.4.2.c Cloud Droplet Counters …….……45

2.4.2.c.i Forward Scattering Spectrometer Probe …...…45

2.4.3 Sampling Strategy …….……46

2.5 Rainfall Patterns and Atmospheric Thermodynamics under African Dust ….47

2.5.1 Software and Models …….……47

2.5.1.a Goddard Earth Sciences Data and Information Services Center …….…….……47

2.5.1.b Igor Pro ® ……...47

2.5.1.c Standardized Precipitation Index Software ……47

2.5.2 Sampling Strategy and Rainfall Analysis ……48

2.5.2.a Land-based Rainfall Totals ……...48

2.5.2.b Satellite-based Rainfall Estimates ……50

2.5.2.c Vertical Profile of the Atmospheric Thermodynamics …51

2.5.2.d Advanced Hydrologic Prediction Service ……52

Chapter 3 RESULTS AND DISCUSSION ……53

3.1 Aerosol Optical Depth and Extinction Ångström Exponent ……53

3.1.1 Correlation between Cape San Juan and La Parguera Sites……...53

3.1.2 Statistical Analysis: Probability Density Function ……56

3.1.3 Climatology ……59

3.1.4 Aerosol Optical Depth and Extinction Ångström Exponent Thresholds …… 63

3.1.4 How does AOD ≥ 0.20 look? ……63

3.2 African Dust Days Across the Northeast Caribbean ……...……66

3.3 Trends in Frequency and Magnitude of African Dust Days ……70

3.4 North African Dipole Intensity Index and its Correlation with the Northeast Caribbean Dustiness ……72

3.5 Aerosol Particle Size and Number Distributions ……89

3.6 Nuclei Activation ……...……93

3.7 Cloud Droplet Concentration ……...94

3.8 Observed Rainfall Patterns ……95

3.9 Vertical Profile of Atmospheric Thermodynamics ……98

Chapter 4 CONCLUSIONS AND FUTURE WORK ……104

Chapter 5 BIBLIOGRAPHY ……107

Appendix A: Saharan Air Layer (SAL) 1995 - 2002 climatology and other air masses .118

Appendix B: Repository of African Dust Days ……119

Appendix C: Ice in Clouds - Tropical, Supplemental Material ……135

Appendix D: Rainfall and the Standardized Precipitation Index ……137

Appendix E: Publications of Odalys Martínez-Sánchez ……...147

List of Abbreviations

ACAR	Atmospheric Chemistry and Aerosol Research
ADD	African Dust Days
ADD – D	African Dust Days - Dry
ADD – W	African Dust Days - Wet
AEJ	African Easterly Jet
AERONET	Aerosol Robotic NETwork
AHPTS	Advanced Hydrologic Prediction Service
AOD	Aerosol Optical Depth
APSPD	Aerosol Particle Spectrometer with Polarization Detection
C6	Collection 6
CBL	Convective Boundary Layer
CCN	Cloud Condensation Nuclei
CCNC	Cloud Condensation Nuclei Counter
CFDC	Continuous Flow Diffusion Chamber
COOP	Cooperative Observer Program
CSJ	Cabezas de San Juan
CSU	Colorado State University
D75	Percentile 75th
DB	Deep Blue
DJF	December January February
DMA	Differential Mobility Analyzer
DT	Dark Target
DTM	Droplet Measurement Technology
Dust- ATTACk	Dust Aging and Transport from Africa to the Caribbean
EDD	Extreme Dust Days
ENSO	El Niño Southern Oscillation
F	Frequency

FSSP	Forward Scattering Spectrometer Probe
GCCN	Giant Cloud Condensation Nuclei
GES DISC	Goddard Earth Sciences Data and Information Services Center
Giovanni	Geospatial Interactive Online Visualization ANd aNalysis Infrastructure
HDD	High Dust Days
HDMMA	High-flow Dual-channel Differential Mobility Analyzer
HYSPLIT	Hybrid Single-Particle Lagrangian Integrated Trajectory
ICE T	Ice in Clouds – Tropical
IN	Ice Nuclei
ITCZ	Inter Tropical Convergence Zone
JJA	June July August
JJAS	June July August September
LLJ	Low Level Jet
LN	Log-Normal
LP	La Parguera
LRT	Long Range Transport
M	Magnitude
MAM	March April May
MBL	Mixing Boundary Layer
MLDAI	Midlatitude day air intrusion
MODIS	Moderate Resolution Imaging Spectroradiometer
MT	Moist Tropical
NAFDI	North African Dipole Intensity
NAO	North Atlantic Oscillation
NASA	National Aeronautics and Space Administration
NCAR	National Center for Atmospheric Research
NCEP	National Center for Environmental Prediction

NOAA	National Oceanic and Atmospheric Administration
NSF/NCAR	National Science Foundation/National Center for Atmospheric Research
NWS	National Weather Service
PRADACTS	Puerto Rico African Dust and Cloud Study
PRIDE	Puerto Rico Dust Experiment
RF	Research flight
RMSE	Root Mean Squared Error
ROC	Rate of Change
SAL	Saharan Air Layer
SALTRACE	Saharan Aerosol Long-range Transport and Aerosol-Cloud-interaction Experiment
SHL	Saharan Heat Low
SON	September October November
SPI	Standardized Precipitation Index
SS	Super Saturation
TOA	Top of the Atmosphere
TOT	Total
TRMM	Tropical Rainfall Measuring Mission
UTC	Coordinated Universal Time
XDD	Exceptional Dust Days
W	Weibull
WFO SJU	National Weather Service Forecast Office San Juan

List of Tables

Table 1.1 Characterization of present-day anthropogenic and natural background atmospheric aerosols in the Hadley Centre climate model (Bellouin et al., 2011) ……..…1

Table 1.2 Standardized Precipitation Index (SPI) values and its corresponding observed rainfall pattern ……..……..……18

Table 1.3 Field campaigns across the Caribbean, including Puerto Rico, intended to analyze chemical, physical, and optical properties of the mineral dust …….……19

Table 1.4 Physical properties of African dust after Long-Range Transport (LRT) **.....**20

Table 1.5 Chemical properties of African dust after Long-Range Transport (LRT) …..20

Table 1.6 Optical properties of African dust after Long-Range Transport (LRT) ……21

Table 2.1 Ice in Clouds - Tropical (ICE-T) Research Flights (RFs) analyzed throughout this research ……..……46

Table 2.2 Weather stations from the National Weather Service COoperative Observer Program (COOP) used throughout this research ……..……49

Table 3.1 Number of African Dust Days (ADD) across Puerto Rico between 2004 and 2018 ……...……68

Table A.1 Saharan Air Layer (SAL) 1995 - 2002 climatology and other air masses……..……..……118

Table B.1 Repository of African Dust Days (ADD) with its corresponding Aerosol Optical Depth (AOD) and extinction Ångström exponent (***å***) ……..……119

List of Figures

Figure 1.1 Mean positive and negative radiative forcing of gases, aerosols, and precursors between 1750 and 2011 (Myhre et al., 2013) ……...3

Figure 1.2 Schematic diagram showing an increased number of smaller cloud droplet sizes, increased albedo, longer lifetime of cloud, and reduced precipitation; mechanisms that are significant concerning atmospheric aerosols (Kirkby, 2001) ……..…….3

Figure 1.3 Schematic diagram of aerosol sizes and processes adapted from Lagzi et al. (2013) ……..…….5

Figure 1.4 Rayleigh and Mie scattering regimes. Under the Rayleigh regime, light is scattered at all directions [http://hyperphysics.phy-astr.gsu.edu] ..……...……6

Figure 1.5 Sequence of three thermodynamic soundings, *Right side*, sounding over west Sahara, showing a barotropic environment (no temperature gradient). *Center*; sounding for a location over the tropical Atlantic Ocean showing the dust layer overlying the shallow marine boundary layer. The SAL base has been lifted encountering a baroclinic region (a zone of deep horizontal temperature gradient), resulting in extensive saturation at various levels and a decreased SAL depth due to condensation (left side). Shading suggests the relative concentration of SAL and its associated potential temperature ***(θ)*** and mixing ratio ***(w)*** (Carlson, 2016) ……11

Figure 1.6 North African Dipole Intensity (NAFDI) Index during its positive phase (July) (Cuevas et al., 2017). The image shows the anomalies of Aerosol Optical Depth (AOD) retrieved from the Moderate Resolution Imaging Spectroradiometer (MODIS) ……..….15

Figure 1.7 North African Dipole Intensity (NAFDI) Index during its negative phase (July) (Cuevas et al., 2017). The image shows the anomalies of Aerosol Optical Depth (AOD) retrieved from the Moderate Resolution Imaging Spectroradiometer (MODIS) ……..….15

Figure 1.8 2007 – 2018 climatological monthly values and associated standard deviation of Aerosol Optical Depth (AOD) over Puerto Rico and Barbados ……..……22

Figure 1.9 2007 – 2018 climatological monthly values and associated standard deviation of extinction Ångström exponent (***å***) over Puerto Rico and Barbados ……22

Figure 2.1 Global distribution of Aerosol Robotic Network (AERONET) ground-based sun photometers supported by the National Aeronautics and Space Administration (NASA) [https://aeronet.gsfc.nasa.gov/] ……..27

Figure 2.2 Google Earth Image of the sampling sites at Cape San Juan (CSJ), La Parguera (LP), and the National Weather Service Forecast Office in San Juan (WFO SJU) …….31

Figure 2.3 Principle of operation for the Aerosol Particle Spectrometer with Polarization Detection (APSPD) (Raga, Baumgardner, & Mayol-Bracero, 2016) **..**……41

Figure 2.4 Principle of operation for the Differential Mobility Analyzer (DMA) adapted from Holmgre (2011) **..**…….……..42

Figure 2.5 Principle of operations Cloud Condensation Nuclei Counter (CCN counter) [http://www.dropletmeasurement.com] **..**…….……..43

Figure 2.6 Principle of operations of Continuous-Flow thermal gradient Diffusion Chamber (CFDC) (Rogers, DeMott, Kreidenweis, & Chen, 2001) **..**…….……..44

Figure 2.7 Principle of operations of Forward Scattering Spectrometer Probe (FSSP) (Baumgardner, Dye, Knollenberg, & Gandrud, 1992) …….……45

Figure 2.8 Google Earth Image of the study area focused on the Weather Stations from the National Weather Service COoperative Observer Program (COOP) used to retrieve rainfall data **..**……..……49

Figure 3.1 Correlation between Aerosol Optical Depth (AOD) AERONET-retrieved at Cape San Juan (CSJ) and La Parguera (LP). Period of Record: 2004 to 2018 …….53

Figure 3.2 Correlation between extinction Ångström exponent (***å***) AERONET-retrieved at Cape San Juan (CSJ) and La Parguera (LP). Period of Record: 2004 to 2018 ……54

Figure 3.3 Correlation between the mid-visible Aerosol Optical Depth (AOD) MODIS-retrieved and AERONET-derived during June. Period of Record: 2004 to 2018 **..**…**.....**55

Figure 3.4 Correlation between the mid-visible Aerosol Optical Depth (AOD) MODIS-retrieved and AERONET-derived during July. Period of Record: 2004 to 2018 **.**……55

Figure 3.5 Correlation between the mid-visible Aerosol Optical Depth (AOD) MODIS-retrieved and AERONET-derived during August. Period of Record: 2004 to 2018 ……56

Figure 3.6 Frequency of Aerosol Optical Depth (AOD) retrieved from the Aerosol Robotic Network (AERONET) at La Parguera (LP) and Cape San Juan (CSJ) (combined time series)**.** Period of Record: 2004 to 2018 **.**…….……...57

Figure 3.7 Frequency of extinction Ångström exponent (***å***) retrieved from the Aerosol Robotic Network (AERONET) at La Parguera (LP) and Cape San Juan (CSJ) (combined time series)**.** Period of Record: 2004 to 2018 **.**…….……...57

Figure 3.8 Probability Density Function (PDF) of Aerosol Optical Depth (AOD) retrieved from the Aerosol Robotic Network (AERONET) at La Parguera (LP) and Cape San Juan (CSJ) (combined time series). Period of Record: 2004 to 2018 ……..……...58

Figure 3.9 Probability Density Function (PDF) of extinction Ångström exponent (***å***) retrieved from the Aerosol Robotic Network (AERONET) at La Parguera (LP) and Cape San Juan (CSJ) (combined time series). Period of Record: 2004 to 2018 ……...59

Figure 3.10 Time series of Aerosol Optical Depth (AOD) retrieved from the Aerosol Robotic Network (AERONET) at La Parguera (LP) and Cape San Juan (CSJ) (combined time series). Period of Record: 2004 to 2018 ……...60

Figure 3.11 Monthly mean and associated standard deviation of Aerosol Optical Depth (AOD) retrieved from the Aerosol Robotic Network (AERONET) at La Parguera (LP) and Cape San Juan (CSJ) (combined series). Period of Record: 2004 to 2018 ……61

Figure 3.12 Time series of extinction Ångström exponent (***å***) retrieved from the Aerosol Robotic Network (AERONET) at La Parguera (LP) and Cape San Juan (CSJ) (combined series). Period of Record: 2004 to 2018 ……62

Figure 3.13 Monthly mean and associated standard deviation of extinction Ångström exponent (***å***) retrieved from the Aerosol Robotic Network (AERONET) at La Parguera (LP) and Cape San Juan (CSJ) (combined series). Period of Record: 2004 to 2018 ……62

Figure 3.14 Time Series of Aerosol Optical Depth (AOD) and extinction Ångström exponent (***å***) retrieved from the Aerosol Robotic Network (AERONET) at La Parguera (LP). Period of Record: June 2019 ……64

Figure 3.15 Photograph of the San Juan Metropolitan Area taken from Parque Escorial on June 11th, 2019, 3 PM. Aerosol Optical Depth (AOD) of 0.32 and (***å***) of 0.12 ……65

Figure 3.16 Photograph of the San Juan Metropolitan Area taken from Parque Escorial on June 19th, 2019, 3 PM. Aerosol Optical Depth (AOD) of 0.25 and (***å***) of 0.22 ……65

Figure 3.17 Photograph of the San Juan Metropolitan Area taken from Parque Escorial on June 23rd, 2019, 3 PM. Aerosol Optical Depth (AOD) of 0.11 and (***å***) of 0.19 ……65

Figure 3.18 Number of African Dust Days (ADD) across Puerto Rico per climatological season between 2004 and 2018. ……67

Figure 3.19 10-day HYSPLIT backward trajectories of days classified as African Dust Days (ADD) during the summer months between 2004 and 2018, a) June, b) July and c) August, respectively ……69

Figure 3.20 Frequency and magnitude of African Dust Days (ADD) during June (top), July (center) and August (bottom) between 2004 and 2018 71

Figure 3.21 Correlation between Aerosol Optical Depth (AOD) monthly anomalies over Puerto Rico and the North African Dipole Intensity (NAFDI) index 73

Figure 3.22 HYSPLIT cluster analysis of 10-day backward trajectories of days classified as African Dust Days (ADD) between 2004 and 2018, June (top), July (center) and August (bottom), respectively 75

Figure 3.23 MODIS-aqua Aerosol Optical Depth (AOD) monthly average 2004-2018 over the tropical Atlantic, June (top), July (center) and August (bottom), respectively 76

Figure 3.24 Geopotential heights at 700 mb from NCEP/NCAR reanalysis during June: (a) years with the highest frequency of African Dust Days (ADD) and (b) years with the lowest frequency of ADD, respectively 78

Figure 3.25 Winds at 700 mb from NCEP/NCAR reanalysis during June: (a) years with the highest frequency of African Dust Days (ADD) and (b) years with the lowest frequency of ADD, respectively..... 79

Figure 3.26 (a) and (c) Geopotential heights and winds at 700 mb June 2012 to 2015. (b) and (d) Geopotential heights and winds at 700 mb during the months of June except 2012 to 2015 81

Figure 3.27 Geopotential heights at 700 mb from NCEP/NCAR reanalysis during July: (a) years with the highest frequency of African Dust Days (ADD) and (b) years with the lowest frequency of ADD, respectively 83

Figure 3.28 Winds at 700 mb from NCEP/NCAR reanalysis during July: (a) years with the highest frequency of African Dust Days (ADD) and (b) years with the lowest frequency of ADD, respectively 84

Figure 3.29 Geopotential heights at 700 mb from NCEP/NCAR reanalysis during August: (a) years with the highest frequency of African Dust Days (ADD) and (b) years with the lowest frequency of ADD, respectively 87

Figure 3.30 Winds at 700 mb from NCEP/NCAR reanalysis during August: (a) years with the highest frequency of African Dust Days (ADD) and (b) years with the lowest frequency of ADD, respectively 88

Figure 3.31 HYSPLIT 7-day backward trajectory of air mass arriving on July 6th, 2011 corresponding to Research Flight 03 (RF03) ……89

Figure 3.32 HYSPLIT 7-day backward trajectory of air mass arriving on July 15th, 2011 corresponding to Research Flight 06 (RF06) ……90

Figure 3.33 HYSPLIT 7-day backward trajectory of air mass on July 30th, 2011 corresponding to Research Flight 13 (RF13) ……90

Figure 3.34 Aerosol particle size distribution retrieved from the Aerosol Particle Spectrometer with Polarization Detection (APSPD) and High-flow Dual-channel Differential Mobility Analyzer (HDDMA) during Ice in Clouds - Tropical (ICE-T) experiment ……91

Figure 3.35 Vertical profile of aerosol particle number concentration retrieved from the Aerosol Particle Spectrometer with Polarization Detection (APSPD) during Ice in Clouds - Tropical (ICE-T) ……92

Figure 3.36 Cloud Condensation Nuclei (CCN) activation retrieved from the Cloud Condensation Nuclei Counter (CCN counter) during Ice in Clouds - Tropical (ICE-T) ...93

Figure 3.37 Ice Nuclei concentration retrieved from the Continuous-Flow thermal gradient Diffusion Chamber (CFDC) during Ice in Clouds - Tropical (ICE-T)……94

Figure 3.38 Droplet concentration retrieved from the Forward Scattering Spectrometer Probe (FSSP) during Ice in Clouds - Tropical (ICE-T) ……95

Figure 3.39 Correlation between frequency of African Dust Days (ADD) during Jun-Jul-Aug (JJA) and its corresponding 3-month standardized precipitation index (SPI) ending in August at Luis Muñoz Marin Airport ……96

Figure 3.40 Correlation between magnitude of African Dust Days (ADD) during June-July and August (JJA) and its corresponding 3-month standardized precipitation index (SPI) ending in August at Luis Muñoz Marin Airport ……97

Figure 3.41 Vertical profile of potential temperature ($\boldsymbol{\theta}$) during African Dust Days (ADD). Comparison between the Saharan Air Layer (SAL) 1995 - 2002 climatology and days classified as ADD -D (Dry) and ADD -W (Wet) ……98

Figure 3.42 Vertical profile of mixing ratio ($\boldsymbol{w}$) during African Dust Days (ADD). Comparison between the Saharan Air Layer (SAL) 1995 - 2002 climatology and days classified as ADD -D (Dry) and ADD -W (Wet) ……99

Figure 3.43 Vertical profile of relative humidity (**RH**) during African Dust Days (ADD). Comparison between the Saharan Air Layer (SAL) 1995 - 2002 climatology and days classified as ADD -D (Dry) and ADD -W (Wet) ……..…..……100

Figure 3.44 Vertical profile of the static energy (***E_s***) during African Dust Days (ADD). Comparison between the Saharan Air Layer (SAL) 1995 - 2002 climatology and days classified as ADD -D (Dry) and ADD -W (Wet) …….……..……101

Figure 3.45 Rainfall totals retrieved from Advanced Hydrologic Prediction Service (AHPS) between July 6th, 2011, 8 AM AST, and July 7th, 2011, 8 AM AST, which corresponds to Research Flight 03 (RF03) …….……....102

Figure 3.46 Rainfall total retrieved from Advanced Hydrologic Prediction Service (AHPS) between July 15th, 2011, 8 AM AST, and July 16th, 2011, 8 AM AST, which corresponds to Research Flight 06 (RF06) ……..……...102

Figure 3.47 Rainfall accumulation retrieved from Advanced Hydrologic Prediction Service (AHPS) between July 30th, 2011, 8 AM AST, and July 31st, 2011, 8 AM AST, which corresponds to Research Flight 13 (RF13) ……..…...……103

Figure C.1 Ice in Clouds -Tropical (ICE-T) flight paths during Research Flights (RF), a) RF03, b) RF06, and c) RF13. **Yellow line** – *cumulus clouds analyzed*. **Red line** – *no cumulus clouds observed* ……...…...……135

Figure C.2 Snapshot (visible imagery) retrieved from the MODerate Resolution Imaging Spectroradiometer (MODIS) during the days corresponding to Research Flights (RF), a) RF03, b) RF06 and c) RF13. Brownish/darker colors suggest African dust. **No data** – *black area*. **Sunglint,** which is a phenomenon that occurs when sunlight reflects off the surface of the ocean at the same angle that a satellite is viewing the surface – *almost a vertical gray area* ……..……136

Figure D.1 Correlation between Frequency of African Dust Days (ADD) during Jun-Jul-Aug (JJA) and its corresponding 3-month standardized precipitation index (SPI) ending in August at Adjuntas Substation ……...……137

Figure D.2 Correlation between Magnitude of African Dust Days (ADD) during Jun-Jul-Aug (JJA) and its corresponding 3-month standardized precipitation index (SPI) ending in August at Adjuntas Substation ……...……137

Figure D.3 Correlation between Frequency of African Dust Days (ADD) during Jun-Jul-Aug (JJA) and its corresponding 3-month standardized precipitation index (SPI) ending in August at Arecibo Observatory …….……..……....138

Figure D.4 Correlation between Magnitude of African Dust Days (ADD) during Jun-Jul-Aug (JJA) and its corresponding 3-month standardized precipitation index (SPI) ending in August at Arecibo Observatory ……..……..……...138

Figure D.5 Correlation between Frequency of African Dust Days (ADD) during Jun-Jul-Aug (JJA) and its corresponding 3-month standardized precipitation index (SPI) ending in August at Coloso ……...……...139

Figure D.6 Correlation between Magnitude of African Dust Days (ADD) during Jun-Jul-Aug (JJA) and its corresponding 3-month standardized precipitation index (SPI) ending in August at Coloso ……...……...139

Figure D.7 Correlation between Frequency of African Dust Days (ADD) during Jun-Jul-Aug (JJA) and its corresponding 3-month standardized precipitation index (SPI) ending in August at Hacienda Constanza ……...…….……140

Figure D.8 Correlation between Magnitude of African Dust Days (ADD) during Jun-Jul-Aug (JJA) and its corresponding 3-month standardized precipitation index (SPI) ending in August at Hacienda Constanza …….....……140

Figure D.9 Correlation between Frequency of African Dust Days (ADD) during Jun-Jul-Aug (JJA) and its corresponding 3-month standardized precipitation index (SPI) ending in August at Manati 2E ……...……..141

Figure D.10 Correlation between Magnitude of African Dust Days (ADD) during Jun-Jul-Aug (JJA) and its corresponding 3-month standardized precipitation index (SPI) ending in August at Manati 2E ……..…...……141

Figure D.11 Correlation between Frequency of African Dust Days (ADD) during Jun-Jul-Aug (JJA) and its corresponding 3-month standardized precipitation index (SPI) ending in August at Ponce 4E ……...……..……142

Figure D.12 Correlation between Magnitude of African Dust Days (ADD) during Jun-Jul-Aug (JJA) and its corresponding 3-month standardized precipitation index (SPI) ending in August at Ponce 4E ……...……...……142

Figure D.13 Correlation between Frequency of African Dust Days (ADD) during Jun-Jul-Aug (JJA) and its corresponding 3-month standardized precipitation index (SPI) ending in August at Lajas Substation ……..……..……....143

Figure D.14 Correlation between Magnitude of African Dust Days (ADD) during Jun-Jul-Aug (JJA) and its corresponding 3-month standardized precipitation index (SPI) ending in August at Lajas Substation ……...……....143

Figure D.15 Correlation between Frequency of African Dust Days (ADD) during Jun-Jul-Aug (JJA) and its corresponding 3-month standardized precipitation index (SPI) ending in August at Guayama 2E 144

Figure D.16 Correlation between Magnitude of African Dust Days (ADD) during Jun-Jul-Aug (JJA) and its corresponding 3-month standardized precipitation index (SPI) ending in August at Guayama 2E 144

Figure D.17 Correlation between Frequency of African Dust Days (ADD) during Jun-Jul-Aug (JJA) and its corresponding 3-month standardized precipitation index (SPI) ending in August at Juncos 145

Figure D.18 Correlation between Magnitude of African Dust Days (ADD) during Jun-Jul-Aug (JJA) and its corresponding 3-month standardized precipitation index (SPI) ending in August at Juncos 145

Figure D.19 Correlation between Frequency of African Dust Days (ADD) during Jun-Jul-Aug (JJA) and its corresponding 3-month standardized precipitation index (SPI) ending in August at Paraiso 146

Figure D.20 Correlation between Magnitude of African Dust Days (ADD) during Jun-Jul-Aug (JJA) and its corresponding 3-month standardized precipitation index (SPI) ending in August at Paraiso 146

Chapter 1 INTRODUCTION: STATE OF KNOWLEDGE

1.1 Aerosols

1.1.1 Atmospheric Aerosol Particles

Atmospheric aerosol particles are a mixture of solid and liquid particles suspended in the air. Pollen from flowers, sea salt spray, mineral dust, and ash from wildfires and volcanoes are considered the natural background atmospheric aerosols. In contrast, the atmospheric aerosols, which are the result of the burning of fossil fuels such as oil, coal, and natural gas, are considered the anthropogenic or man-made aerosols.

In both cases, primary aerosol particles are continuously emitted into the atmosphere, while secondary aerosol particles are formed in the atmosphere. Table 1.1 shows the anthropogenic and natural emission rates of primary atmospheric aerosols as well as aerosol loads.

Table 1.1 Characterization of present-day anthropogenic and natural background atmospheric aerosols in the Hadley Centre climate model (Bellouin et al., 2011).

Primary Aerosol	Emission Rate (Tg yr^{-1})	Aerosol Loads (mg m^{-2})
Sulfate	60.3 ± 0.8	1.0 ± 0.0
Mineral Dust	8192 ± 399	88.2 ± 7.3
Sea Salt	NA	50.3 ± 0.1
Fossil Fuel Black Carbon	5.2 ± 0.1	0.5 ± 0.0
Biomass burning	25.9 ± 0.1	1.8 ± 0.1
Biogenic	NA	2.2 ± 0.0
Fossil Fuel Organic Carbon	12.7 ± 0.1	0.4 ± 0.0
Nitrate	42.1 ± 0.3	0.2 ± 0.0

1.1.2 Atmospheric Aerosol Particles and their Impacts on Weather and Climate

The atmospheric aerosol particles can alter the Earth's radiative forcing directly, by scattering and absorbing solar and terrestrial radiation, and indirectly by altering cloud microphysical properties (Forster et al., 2007).

The direct effect of these particles involves the balance between the incoming shortwave solar radiation and the outgoing longwave terrestrial radiation. The incoming or outgoing radiation can be absorbed, reflected, refracted, diffracted, or transmitted, depending on size, chemical composition, shape, and orientation (if non-spherical) of the atmospheric particles. If the incoming solar radiation exceeds the outgoing terrestrial radiation, there is a positive radiative forcing (i.e., warming at the troposphere) (Figure 1.1). Conversely, if the outgoing terrestrial radiation is exceeding the incoming solar radiation, there is a negative radiative forcing (i.e., cooling at troposphere).

The indirect effect of these atmospheric particles on the Earth's radiative forcing involves the aerosol particles that can nucleate into cloud droplets. An increased number of aerosol particles increases the **C**loud **C**ondensation **N**uclei (**CCN**), and **I**ce **N**uclei (**IN**) number concentration. Consequently, an increased CCN and IN number concentration lead to smaller cloud droplet sizes that reduce the amount of precipitation (Twohy et al., 2009) (Figure 1.2). A smaller cloud droplet sizes increase the albedo of the cloud due to a longer cloud lifetime, which results in a cooling effect as well (Twomey, 1977).

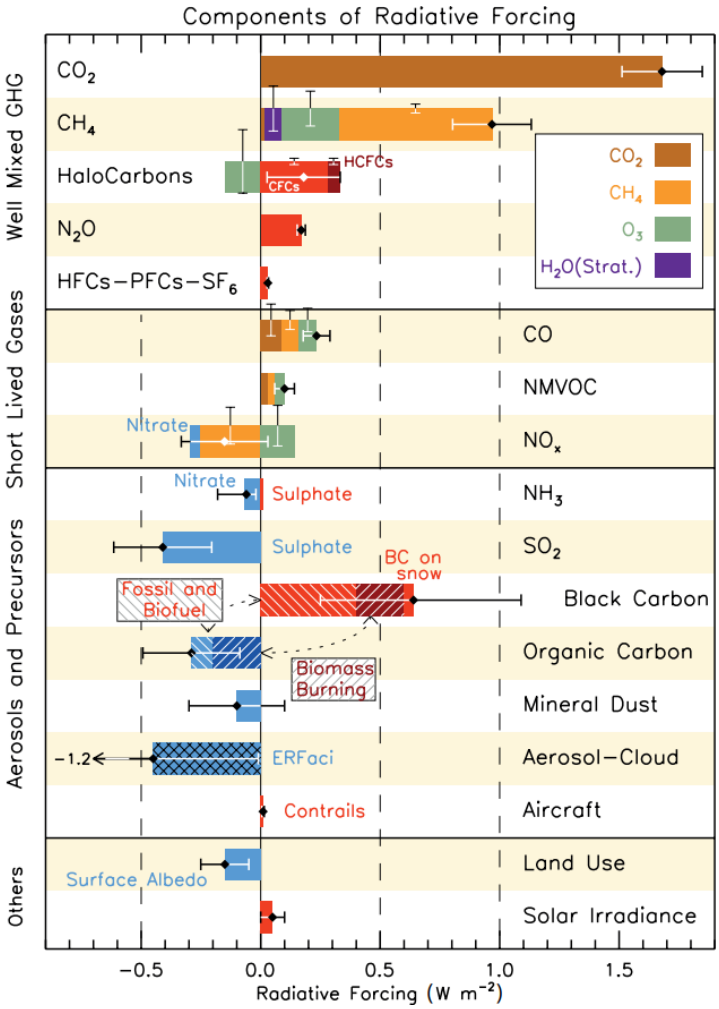

Figure 1.1 Mean positive and negative radiative forcing of gases, aerosols, and precursors between 1750 and 2011 (Myhre et al., 2013).

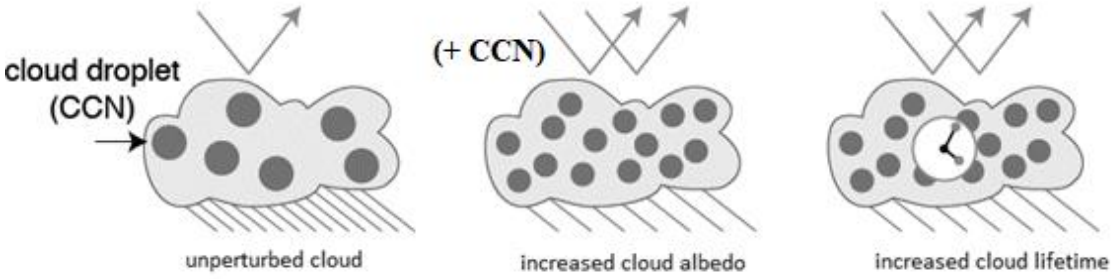

Figure 1.2 Schematic diagram showing an increased number of smaller cloud droplet sizes, increased albedo, longer lifetime of cloud, and reduced precipitation; mechanisms that are significant concerning atmospheric aerosols (Kirkby, 2001).

1.2 Aerosol Physical Properties

The diameter of the atmospheric aerosol particles spans over four orders of magnitude (Figure 1.3). Particles with diameters larger than 1.0 μm are classified as *coarse mode particles*. These particles are mainly produced by mechanical processes and are introduced directly into the atmosphere from both natural and anthropogenic sources. The coarse particles settle out of the atmosphere in a short period (days to hours) by sedimentation.

Particles with diameters between 0.1 and 1.0 μm are classified as *accumulation mode particles,* which represent a region of particle growth mainly due to the coagulation between particles. These particles can also be introduced directly into the atmosphere, mainly through the incomplete combustion of fossil fuels. These particles stay suspended in the air until they are washed away through wet deposition.

The *Aitken* mode particles extend from 0.01 to 0.1 μm diameter. These particles are formed from ambient-temperature gas-to-particle conversion as well as condensation of hot vapors during combustion processes. The lifetime of these particles is short, as they are lost by coagulation with larger particles.

Aerosol particles with diameters less than 0.01 μm are known as *ultrafine* particles. They are generated by gas-to-particle conversion and have a very short lifetime, sometimes on the order of minutes due to evaporation or coagulation with larger particles.

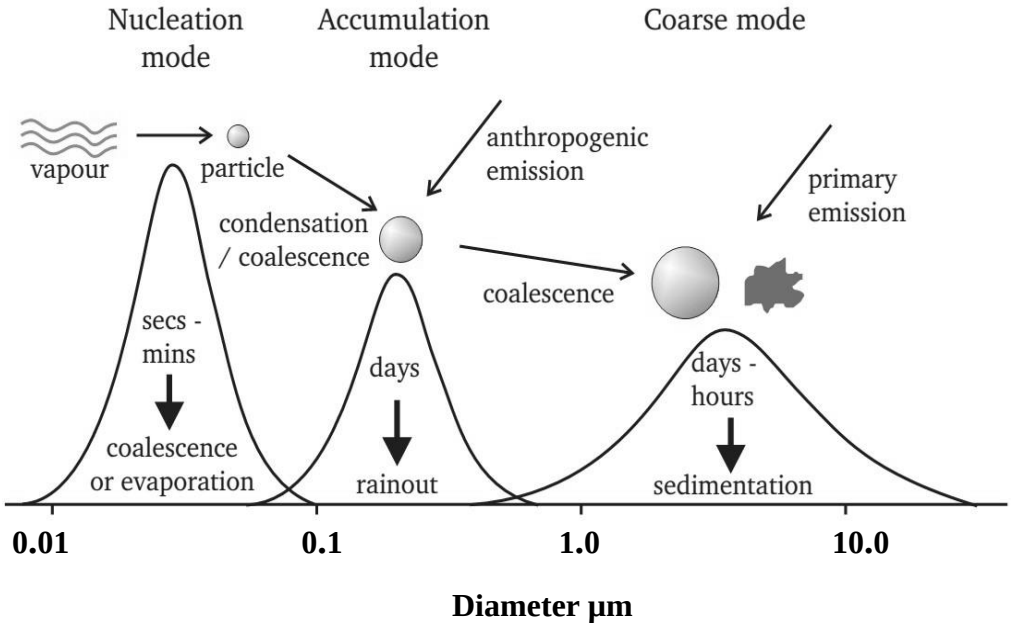

Figure 1.3 Schematic diagram of aerosol sizes and processes adapted from Lagzi et al. (2013).

The ultrafine and Aitken particles, both under the nucleation mode, have the most significant contribution to the particle number distribution. In contrast, the accumulation mode has the most significant contribution to the particle surface distribution (Hinds, 1999). Most of the aerosol volume distribution, however, is determined by the contribution of the coarse mode particles.

1.3 Aerosol Optical Properties

The size, shape, morphology, and refractive index of the atmospheric aerosols determine the amount of scattering and absorption. The scattering from atomic and molecular particles (particle size << incident wavelength) is known as Rayleigh scattering while the scattering from larger particles (particle size ≃ incident

wavelength) such as pollen, dust, smoke and water droplets is known as Mie scattering (Figure 1.4).

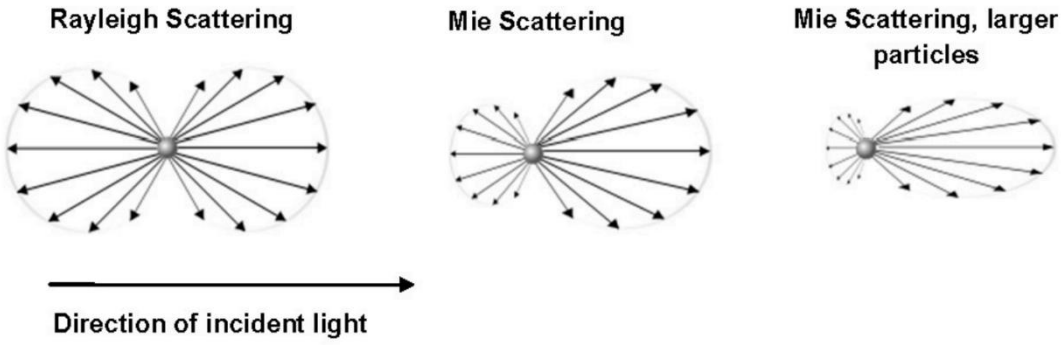

Figure 1.4 Rayleigh and Mie scattering regimes. Under the Rayleigh regime, light is scattered at all directions [http://hyperphysics.phy-astr.gsu.edu].

Scattering Coefficients

The scattering coefficient (σ_{sp}) expresses the attenuation of solar and terrestrial radiation due to reflection, refraction, and diffraction by the atmospheric particles. It is expressed in units of reciprocal distance (m^{-1}) and refers to scattering intensity in all directions. The total backscattering coefficient (σ_{bsp}) refers to the scattering intensity redirected into the backward hemisphere of the scattering particle.

The difference between σ_{sp} and σ_{bsp} gives the forward scattering coefficient that is occurring in the forward hemisphere of the particle.

Absorption Coefficient

The total absorption coefficient ($\boldsymbol{\sigma_{ap}}$) is a measure of the attenuation of radiation due to absorbed electromagnetic radiation by the atmospheric particles converted into thermal energy. It is expressed in units of reciprocal distance (m^{-1}).

Total Extinction and Aerosol Optical Depth

The total extinction ($\boldsymbol{\sigma_{ext}}$) coefficient is the sum of the total scattering and the total absorption, $\boldsymbol{\sigma_{sp}}$, and $\boldsymbol{\sigma_{ap}}$, respectively. It is expressed in units of reciprocal distance (m^{-1}) and represents the total attenuation of the solar and terrestrial radiation due to scattering and absorption processes by the atmospheric particles.

The **A**erosol **O**ptical **D**epth (**AOD**), which is unitless, is a measure of how much atmospheric aerosol particles are preventing the transmission of light through the atmosphere. The higher the value, the higher the extinction of solar radiation. The AOD is given by

$$\frac{I}{I_0} = e^{(-\sigma_{ext} z)} \qquad (1.1)$$

where $\boldsymbol{I}$ is the spectral irradiance that reaches the earth's surface, $\boldsymbol{I_o}$ is the spectral irradiance at the **T**op **O**f the **A**tmosphere (**TOA**), $\boldsymbol{\sigma_{ext}}$ is the total extinction, and $\boldsymbol{z}$ is the height of the atmospheric column.

The extinction Ångström exponent ($\boldsymbol{å}$) describes the wavelength (λ) dependence of AOD, $\boldsymbol{\sigma_{ext}}$, $\boldsymbol{\sigma_{ap}}$, $\boldsymbol{\sigma_{sp}}$ by a negative power law. The particle size, which is an indicator of the aerosol type, can be estimated through $\boldsymbol{å}$. Values higher than two are associated with fine

mode particles such as smoke particles and sulfates, while values near zero indicate the presence of coarse mode particles like mineral dust (Eck et al., 1999).

$$\mathring{a} = -\frac{d\,In\,AOD}{d\,In\,\lambda} \qquad (1.2)$$

1.4 African Mineral Dust

1.4.1 Dust Sources

Mineral dust emissions occur from multiple sources around the globe; however, 78% of them are located north of the equator (Engelstaedter & Washington, 2007). The other 22% are in dry regions of South America, southern Africa, and Australia, being the latest the most significant source in the Southern Hemisphere (Shao et al., 2011). The most significant dust sources are located along an area known as the dust belt, which extends from northern Africa across the Middle East and Central Asia to northern India, as well as into China and Mongolia.

The Sahara Desert in northern Africa is considered the largest mineral dust source, estimated to produce about 70% of the total global mass and six times more than the next largest source, the Gobi Desert in China and Mongolia (Huneeus et al., 2011). The mineral dust particles that are injected into the atmosphere can be transported southward over the Sahel and Gulf of Guinea (60%), westward to the Atlantic (25%), northward to Europe (10%) and eastward to the Middle East (5%) (d'Almeida, 1986).

In northern Africa, Prospero (2002) identified two primary dust sources; the Bodélé Depression in Chad and an area in west Africa, comprising portions of Mauritania, Mali, and southern Algeria. Secondary dust sources in northern Africa are Tunisia and northeast Algeria.

The dust uplifted in Tunisia and northeast Algeria is predominantly transported northward to the western Mediterranean and western Europe while dust uplifted in Western Sahara, western Mauritania, southern Argelia and northern Mali is transported westward towards the Atlantic coast (Scheuvens, Schütz, Kandler, Ebert, & Weinbruch, 2013). The dust uplifted in the Bodélé depression, which is the most active dust source, advects towards west Africa and the Gulf of Guinea (Kalu, 1979).

1.4.2 Dust Mobilization

Dust mobilization occurs if the near-surface wind speeds are above the local emission threshold. The emission threshold corresponds to the minimum wind velocity that must be reached for the initiation of soil particle horizontal motion. This threshold depends on soil properties (size distribution and moisture) and roughness (Gillete, 1974). Smooth surfaces with dry and sandy soils, in general, have the lowest erosion thresholds, while the highest erosion thresholds characterize the rough surfaces.

The movement of soil particles close to the surface is mainly by saltation, where soil particles rebound on the surface and initiate the movement of other particles. These rebounds also lead to the ejection of fine dust particles from the surface or salting

aggregates. Once in motion, the movement of mineral dust particles depends on its size, shape, and density, being controlled by the balance between their terminal fall velocity and the air vertical velocity (Gillette, 1974).

1.4.3 Dust Emission, Transport, and the Saharan Air Layer

Dust emission from the African continent requires a mesoscale driver, such as a surface thermal low, while transport requires a synoptic-scale pattern such as an anticyclone. The surface thermal low, also known as the **S**aharan **H**eat **L**ow (**SHL**) (surface to 925 mb at ~20N), is the thermal response of the lower troposphere to the intense and prolonged surface warming over the desert (Lavaysse et al., 2009). The SHL and its associated dry convection are responsible for dust mobilization over Africa due to density currents or **l**ow-**l**evel **j**ets (**LLJ**) (Fiedler, Schepanski, Heinold, Knippertz, & Tegen, 2013; Lavaysse, Flamant, & Janicot, 2010). The SHL is coupled with the **A**frican **E**asterly **J**et (**AEJ**), which forms at ~600 mb near the 15-20˚N latitude, and the North African anticyclone typically present at 700 mb and aloft. The strengthening of the North African anticyclone has implications in wind speeds north of the **I**nter-**T**ropical **C**onvergence **Z**one (**ITCZ**), which results in enhanced dust transport toward the Subtropical North Atlantic (Rodríguez et al., 2015).

The Saharan Air Layer (SAL)

The **S**aharan **A**ir **L**ayer (**SAL**) describes the dry, warm, and sometimes dust-laden layer of the atmosphere overlying the cooler and more-humid surface marine layer west

of the African continent. This layer can be recognized across the Caribbean at 600-800 mb as a layer with a potential temperature ***(Θ)*** of about 40 ˚C and a constant water vapor mixing ratio ***(w)*** of 2 to 4 g kg^{-1} (Carlson & Prospero, 1972).

Figure 1.5 shows the typical SAL vertical profile with pressure ***(p)*** against temperature ***(T)*** and ***w***. As the hot and dry air mass over west Sahara moves into the Atlantic Ocean, it is affected by heat and moisture exchange with the ocean surface. There is heat exchange at the lower levels of the atmosphere whenever there is a temperature gradient in the horizontal.

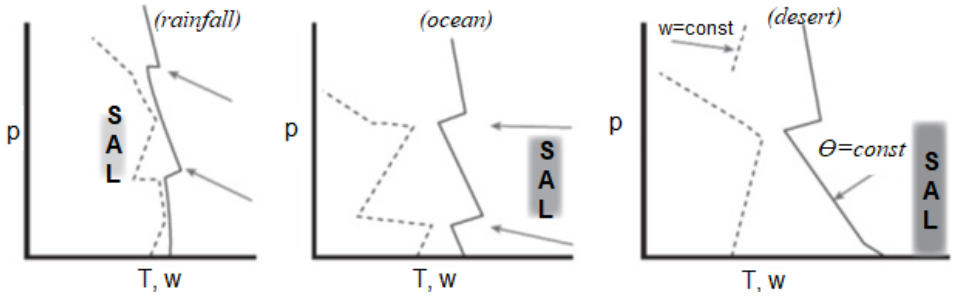

Figure 1.5 Sequence of three thermodynamic soundings, *Right side*, sounding over west Sahara, showing a barotropic environment (no temperature gradient). *Center*; sounding for a location over the tropical Atlantic Ocean showing the dust layer overlying the shallow marine boundary layer. The SAL base has been lifted encountering a baroclinic region (a zone of deep horizontal temperature gradient), resulting in extensive saturation at various levels and a decreased SAL depth due to condensation (left side). Shading suggests the relative concentration of SAL and its associated potential temperature ***(Θ)*** and mixing ratio ***(w)*** (Carlson, 2016).

Besides ***Θ*** and ***w,*** the static energy E_s is used as well to characterize the African air masses through the atmospheric stability.

The static energy, E_s, is given by

$$E_s = gz + C_p T + Lw \quad (1.3)$$

where ***Cp*** is the specific heat at constant pressure, ***T*** is the absolute air temperature, ***g*** is the gravitational constant, ***z*** is the height above the surface, and ***L*** is the latent heat of water condensation.

Aspliden (1972) deduced a minimum in the E_s profile at 750 mb. He found that a very dry and stable African air mass has a value of E_s lower than 330 kJ kg^{-1}. Petit et al. (2005) also used E_s to identify the dry, stable, and dusty air masses but with a slight adaptation, a threshold value of 325 kJ kg^{-1} at 850 mb.

1.4.4 Dust Seasonal Patterns

The **L**ong-**R**ange **T**ransport (**LRT**) of mineral dust from North Africa is the most intense and the best documented in the world (Marticorena & Formenti, 2013). Dust emission over the entire Sahara Desert is characterized by a maximum in the spring and a minimum in the fall (Marticorena & Formenti, 2013). Decades of satellite imagery, however, show the strong seasonal cycle of dust transport into the Caribbean during the Northern Hemisphere summer as the ITCZ reaches its most northern position (Prospero et al., 2014).

The seasonal progression of the ITCZ is also linked to the intensification of dust source regions (Prospero, 2002). Although the Bodélé Depression is the most active single dust source on Earth and delivers large quantities of dust towards west Africa and

the Gulf of Guinea (Kalu, 1979); Western Sahara, western Mauritania, southern Algeria, and northern Mali are the major sources of dust transported across the Atlantic Ocean to America (Scheuvens et al., 2013).

Besides the inter-seasonal variations, there are also inter-annual variations that have been studied and linked to dust activity. Prospero and Lamb (2003) found that there is a maximum in dust emission during El Niño years due to the strengthening of the West African monsoon. Also, Ginoux et al. (2004) indicated increasing opportunities for dust mobilization during the positive phase of the **N**orth **A**tlantic **O**scillation (**NAO**) due to the strengthening of the Azores High and a much drier pattern over North Africa. Although the NAO is useful to explain the variability of dust during the winter, it is less useful during the summer (Ginoux et al., 2004) when the dust is transported towards the Caribbean region.

1.4.5 Enhanced Dust Transport

The enhanced dust transport toward the Subtropical North Atlantic can be described with the **N**orth **A**frican **D**ipole **I**ntensity (**NAFDI**) index established by Rodriguez et al. (2015) and modified by Cuevas et al. (2017) who explained the connections between dust transport and the longitudinal shift of the SHL.

The NAFDI values have been classified as positive ($\geq +0.4$), negative (≤ -0.4), or neutral (between -0.4 and +0.4). Under a positive NAFDI phase, the Azores High and the North African anticyclone strengthen and get closer at 700 mb with the SHL shifting

west. This results in dust source intensification over central Algeria and enhanced dust transport over Western Sahara into the Subtropical North Atlantic (Figure 1.6) (Cuevas et al., 2017). Conversely, under a negative NAFDI phase, a trough displaces an elongated Azores High from North African anticyclone with the SHL shifting east. This results in dust source intensification east-central Sahara and enhanced transport to the Mediterranean (Figure 1.7) (Cuevas et al., 2017).

Essentially, the NAFDI index represents a large-scale geostrophic wind anomaly over Northern Africa (Cuevas et al., 2017) and helps us to quantify how strong the gradient in moisture and temperature is between the hot and dry desert and the cooler and wet Gulf of Guinea.

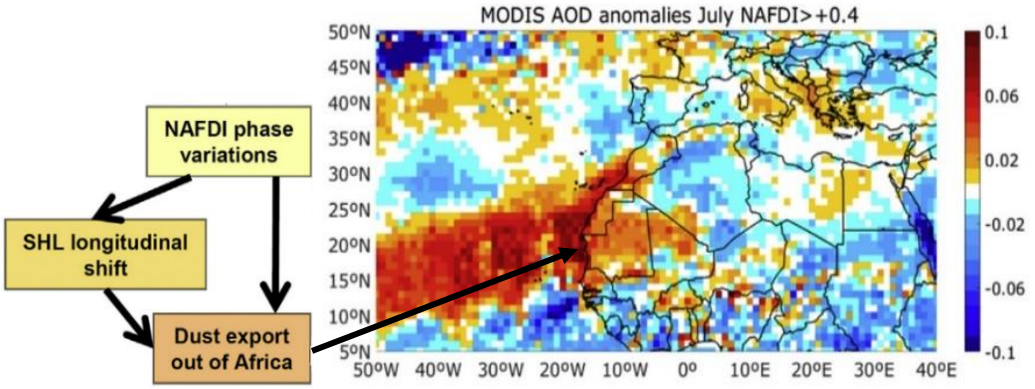

Figure 1.6 North African Dipole Intensity (NAFDI) Index during its positive phase (July) (Cuevas et al., 2017). The image shows the anomalies of Aerosol Optical Depth (AOD) retrieved from the Moderate Resolution Imaging Spectroradiometer (MODIS).

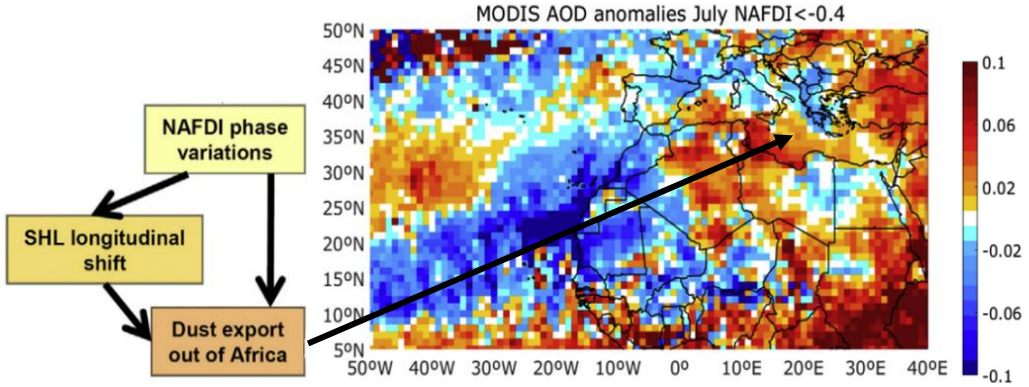

Figure 1.7 North African Dipole Intensity (NAFDI) Index during its negative phase (July) (Cuevas et al., 2017). The image shows the anomalies of Aerosol Optical Depth (AOD) retrieved from the Moderate Resolution Imaging Spectroradiometer (MODIS).

1.5 Dust as Cloud Condensation Nuclei and Ice Nuclei

Cloud droplet formation depends on water vapor condensation on soluble atmospheric particles under conditions that favor the formation of a liquid phase. The main physical-chemical principles involved in the activation of condensation nuclei into cloud droplets depends on whether the atmospheric particles can experience unconstrained water uptake from the water vapor phase. Water uptake from the water vapor phase occurs if the ambient water vapor pressure persistently exceeds the equilibrium water vapor pressure over the particles (Knippertz & Stuut, 2014). This process of droplet activation and subsequent growth is known as condensational growth.

Although mineral dust remains non-hygroscopic after LRT (Denjean et al., 2015), dust particles can still act as CCN or IN under subsaturated conditions due to their relatively large size (Choobari, Zawar-Reza, & Sturman, 2014). In general, to activate cloud droplets, an insoluble but wettable dust particle must be larger than ~ 0.7 μm (Koehler, Kreidenweis, DeMott, Prenni, & Petters, 2007).

Increased concentrations of **G**iant **C**loud **C**ondensation **N**uclei (**GCCN**) (nuclei ≥ 1 μm) may act as efficient collector drops and promote the formation of precipitation (Cheng, Carrió, Cotton, & Saleeby, 2009). Conversely, increased concentrations of CCN result in higher droplet concentrations and small droplet sizes, unlikely to form precipitation (Twohy et al., 2009). These smaller droplets, when lifted above the freezing level, can subsequently release latent heat through ice formation and growth

(Jenkins & Pratt, 2008; Khain et al., 2008). This effect can strengthen the updraft and prolong the storm life cycle (Andreae et al., 2004).

1.6 Rainfall Patterns and the Standardized Precipitation Index

A wet or dry pattern can be identified using the **S**tandardized **P**recipitation **I**ndex (**SPI**) (Table 1.2). The SPI calculation is based on the long-term rainfall record for a desired period and location. This long-term rainfall record is fitted to a gamma distribution, then transformed into a normal distribution, which was then transformed into an index (Edwards & Mckee, 1997).

As a result, the mean SPI for the desired period and location is zero. Positive SPI values indicate higher than the mean (wetter conditions), while negative values indicate less than the mean (drier conditions). The SPI values can be interpreted as the number of standard deviations by which the observed rainfall anomaly deviates from the long-term mean (Keyantash, John & National Center for Atmospheric Research Staff (Eds), 2018).

Table 1.2 Standardized Precipitation Index (SPI) values and its corresponding observed rainfall pattern.

Standardized Precipitation Index	Rainfall Pattern Observed
2.0+	Extremely wet
1.5 to 1.99	Severely wet
1.0 to 1.49	Moderately wet
-0.99 to 0.99	Near normal
-1.0 to -1.49	Moderately dry
-1.5 to 1.99	Severely dry
-2 and less	Extremely dry

The SPI can be calculated from 1 month up to 72 months. The 1-month SPI assesses the short-term rainfall while the 3- to 6- month provides information about the seasonal to inter-seasonal observed rainfall. The 9- month and up reflects long-term rainfall patterns.

1.7 African Dust across the Caribbean

Previous studies and field campaigns intended to analyze the physical, chemical, and optical properties of dust aerosols across the Caribbean are described in Table 1.3.

Table 1.3 Field campaigns across the Caribbean, including Puerto Rico, intended to analyze chemical, physical, and optical properties of the mineral dust.

Campaign	Period	Objective
Puerto **Ri**co **D**ust **E**xperiment **(PRIDE)**	Summer 2000	Surface, airborne, and satellite measurements of African dust properties focused across the Caribbean.
Puerto **R**ico **A**frican **D**ust **a**nd **C**louds **S**tudy (**PRADACS**)	Summer 2010 - 2011	Intended to understand the role of long-range African dust in cloud formation processes across the Caribbean.
Ice in Clouds - **T**ropical (**ICE-T**)	Summer 2011	Aircraft measurements intended to analyze chemical, physical, and cloud activating properties of aerosols during dust outbreaks.
Dust Aging and **T**ranspor**t** from **A**frica to the **C**aribbean **(Dust-ATTACk)**	Summer 2012	Ground-based measurements that studied size distributions and optical properties of African dust across the Caribbean.
Saharan **A**erosol **L**ong-range **Tr**ansport and **A**erosol-**C**loud-interaction **E**xperiment **(SALTRACE)**	Summer 2013	Intended to combine ground-based, airborne, in-situ, and lidar measurements across the eastern Atlantic and the Caribbean to investigate the long-range transport of Saharan mineral dust.

Physical, chemical, and optical properties found after LRT between Africa and the Caribbean are summarized in Tables 1.4, 1.5, and 1.6.

Table 1.4 Physical properties of African dust after Long-Range Transport (LRT).

Physical Properties	Characteristics
Size	• A shift to a smaller size spectrum associated with the loss of larger particles during the first 1-3 days and an increase in particles under the accumulation mode. There is a little variation in the volume distribution between Africa and the Caribbean. (Weinzierl et al., 2017). *Field Campaign: SALTRACE, 2013*. The volume distribution peak at 2-3 µm (Denjean et al., 2016).
Shape	• Preferential removal by dry deposition of spherical particles during transit. (Marticorena & Formenti, 2013)

Table 1.5 Chemical properties of African dust after Long-Range Transport (LRT).

Chemical Properties	Characteristics
Mixing State	• Most of the mineral dust remains externally mixed. A minor portion of mineral dust was internally mixed with sulfate and chloride (~13–24%) or aggregated with sea-salt particles (~3–6%) (Denjean et al., 2015). *Field Campaign: Dust- ATTACk 2012*.
Hygroscopicity and Solubility	• Dust remains non-hygroscopic. The enhancement of dust hygroscopicity is associated with aggregation with NaCl particles (Denjean et al., 2015). *Field Campaign: Dust-ATTACk 2012*

Table 1.6 Optical properties of African dust after Long-Range Transport (LRT).

Optical Properties	Characteristics
Scattering Coefficient **Single Scattering Albedo** **Mass efficiency**	• Little change in the scattering coefficient; however, there are changes in scattering efficiency per unit mass due to smaller particles. • Single Scattering Albedo at visible wavelengths ranges 0.97-0.98 for $PM_{10.}$ These values are consistent with measurements at short time after emission (< 3 days). • Mass Extinction Efficiency at visible wavelengths ranges 1.1 -1.5 m^2/g. (Denjean et al., 2016) *Field Campaign: Dust-ATTACk 2012*

African dust particles have a maximum transport into the Caribbean during the boreal summer (Prospero et al., 2014). These dust particles are found up to ~5 km over the African coast; however, as they are transported westward by the trade winds, a decrease in altitude from 5 to 3 km is observed (Huang, Zhang, & Prospero, 2010).

The 2007-2018 climatological values of AOD and ***å*** across the northeast and the southeast Caribbean are shown in Figure 1.8 and 1.9. The AOD and ***å*** values retrieved over the northeast Caribbean correspond to measurements retrieved over Puerto Rico. In contrast, the AOD and ***å*** values retrieved over the southeast Caribbean correspond to measurements in Barbados.

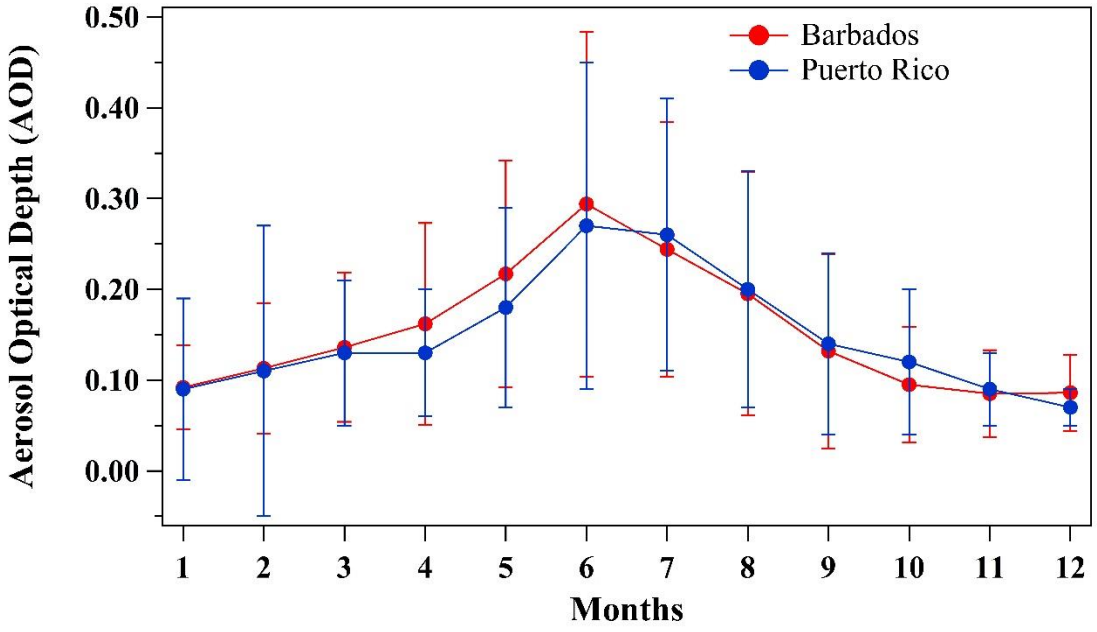

Figure 1.8 2007 – 2018 climatological monthly values and associated standard deviation of Aerosol Optical Depth (AOD) over Puerto Rico and Barbados.

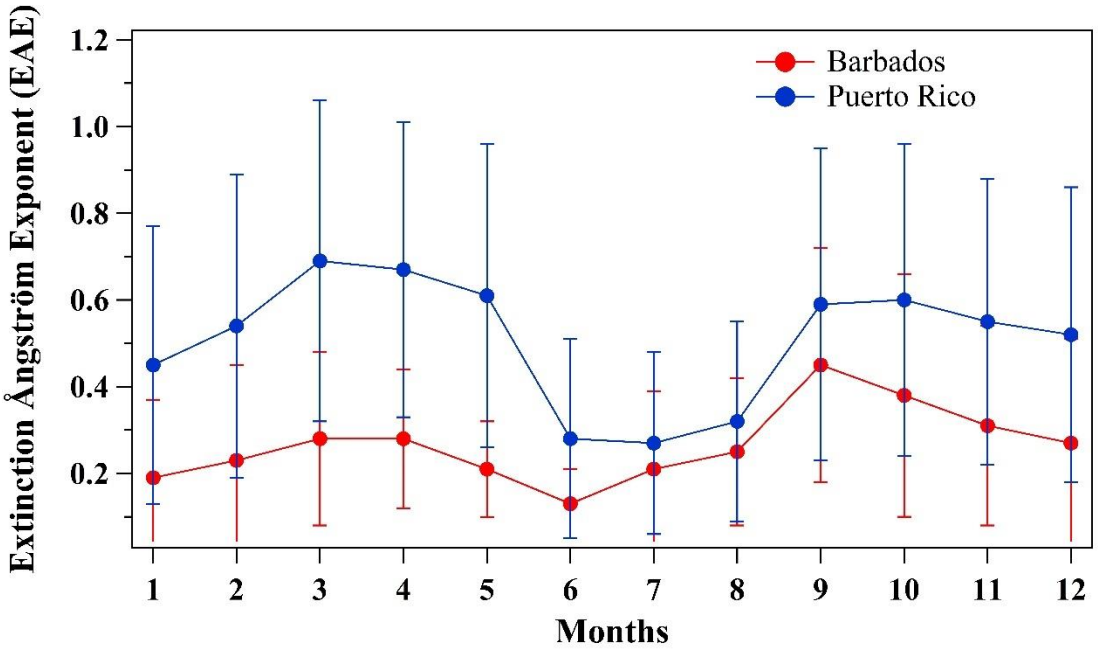

Figure 1.9 2007 – 2018 climatological monthly values and associated standard deviation of extinction Ångström exponent (***å***) over Puerto Rico and Barbados.

1.8 Statement of the Problem and the Intellectual Merit

Although there have been several field campaigns conducted to improve the understanding of aerosol dust load across the Caribbean, most of them have been focused near the island of Barbados. Therefore, there are still fundamental unanswered questions across the Puerto Rico area, which is located on the northern edge of the 'dust corridor' (Moreno et al., 2006).

This study aims to identify the **A**frican **D**ust **D**ays (**ADD**) across the Puerto Rico area between 2004 and 2018; to assess trends in the frequency and magnitude during June, July and August (JJA) when the strong seasonal cycle of dust transport into the Caribbean is observed (Prospero et al., 2014); to show how the intra-seasonal variations of dust transport into the northeast Caribbean is modulated by the NAFDI index, and to identify impacts on rainfall patterns.

This will be achieved by answering the following **scientific questions**:

1- *Is the frequency and magnitude of African dust days changing across the Puerto Rico area?*

2- *Is it possible to identify atmospheric patterns that enhance African dust days across the northeast Caribbean?*

3- *Is mineral dust, after aging during its transport from Africa, affecting the local rainfall pattern through mineral dust acting as Cloud Condensation Nuclei (CCN)?*

The **objectives** of this study are:

- To identify trends in frequency and magnitude of African Dust Days across the Puerto Rico area.
- To identify atmospheric patterns that enhance the frequency of African Dust Days across the northeast Caribbean.
- To characterize aerosol particle size and number distributions as well as cloud condensation nuclei, ice nuclei, and cloud droplet concentrations during dust outbreaks with its associated impacts on rainfall patterns.

As a result, the following **hypotheses** are tested:

Hypothesis 1: "There is an increasing trend in the frequency and magnitude of African dust days across Puerto Rico, and it can be assessed through aerosol optical properties."

Hypothesis 2: "African dust plays an important role in weather and climate by suppressing rainfall across Puerto Rico through the addition of more aerosol particles which can lead to smaller cloud droplets that reduce the amount of precipitation."

The **originality** and **intellectual merit** of this research rely on the following:

- It is the first time that African Dust Days between 2004 and 2018 are accurately identified across the Puerto Rico area with trends in frequency and magnitude assessed.
- It is the first time that a conceptual model of African dust transport into the northeast Caribbean is developed through the NAFDI index.

- It is the first time that the thermodynamic characteristics of the local atmosphere during African Dust Days with and without rainfall are assessed.

1.9 Thesis Outline

Chapter I introduces the statement of the problem with its corresponding scientific questions, relevance, and previous work. **Chapter II** describes the sampling area, collection methods, and analysis performed to the retrieved data. **Chapter III** presents and discusses the characterization of aerosol optical properties, microphysical properties of aerosol particles, and thermodynamic characteristics of the local atmosphere with its impacts on rainfall. **Chapter IV** addresses the general conclusions of this research and presents recommendations for future work. All references cited in this work are listed in **Chapter V**.

Chapter 2 EXPERIMENTAL DESIGN

2.1 Assessment of Aerosol Optical Properties across the Northeast Caribbean

2.1.1 Software and Models

2.1.1.a Igor Pro ®

The data analysis software used throughout this research was Igor Pro ®, developed by WaveMetrics. This software allows to import, graph, and apply statistical analysis to a large volume of data.

2.1.2 Instrumentation Platforms

2.1.2.a Aerosol Robotic NETwork

The **A**erosol **R**obotic **NET**work (**AERONET**) is a globally distributed network of ground-based solar-powered CIMEL Electronique sun photometers. The sun photometers measure radiances at seven wavelengths in the range of 0.340-1.02 μm (Figure 2.1).

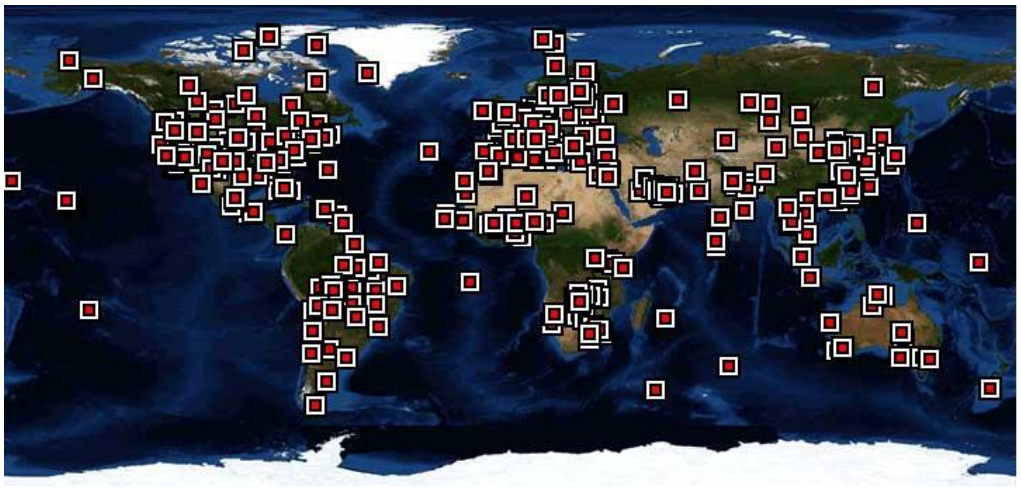

Figure 2.1 Global distribution of Aerosol Robotic Network (AERONET) ground-based sun photometers supported by the National Aeronautics and Space Administration (NASA) [https://aeronet.gsfc.nasa.gov/].

The network provides quality-assured (Level 2) datasets for scientific analysis at each site. However, there are real-time data that are not quality assured [Level 1(unscreened) and Level 1.5 (quality controlled and cloud screened)] yet provide relevant information on the optical properties of the atmospheric aerosols.

The voltage ***(V)*** measured by the CIMEL is proportional to the spectral irradiance ***(I)*** that reaches the Earth's surface. The spectral irradiance estimated at the top of the atmosphere ***(I_o)*** in terms of voltage ***(V_o)*** is obtained by sunphotometer measurements at Mauna Loa Observatory in Hawaii (elevation: 3,397 m).

With the spectral irradiance at the Earth's surface and the top of the atmosphere; the total optical depth ***(τ_{TOT})*** is calculated using the Beer-Lambert-Bouguer Law equation:

$$V(\lambda) = V_0(\lambda) d^2 e^{-\tau(\lambda)_{TOT} * m} \qquad (2.1)$$

where V is the digital voltage measured at wavelength λ, Vo is the extraterrestrial voltage, d is the ratio of the average to the actual Earth-Sun distance, τ_{TOT} is the total optical depth, and m is the optical air mass (Holben, 1998).

To obtain the aerosol component or AOD, however, the optical depth due to water vapor, Rayleigh scattering, and other wavelength-dependent trace gases must be subtracted from (τ_{TOT}). Besides AOD, the AERONET also provides derived aerosol properties such as single scattering albedo (ω_0) which is defined as $\omega_0 = \sigma_{sp} / (\sigma_{ext} + \sigma_{sp})$, and the extinction Ångström exponent ($å$). The single scattering albedo refers to the ratio between the scattering to the total extinction, while $å$ is a proxy for aerosol particle size (Eck et al., 1999). The AERONET data which have an uncertainty of ± 0.01 (Eck et al., 1999) were obtained through https://aeronet.gsfc.nasa.gov/

2.1.2.b Moderate Resolution Imaging Spectroradiometer

The **MOD**erate Resolution **I**maging **S**pectroradiometer (**MODIS**) launched to Sun-synchronous polar orbits on the Aqua platform (1:30 P.M. local solar Equatorial crossing time) has been providing data in 36 spectral bands between 0.41 and 14.4 μm since May 2002. MODIS has a spatial resolution of 1°×1° and a scan width of 2,330 km, providing near-daily global coverage at the equator. The MODIS **C**ollection **6** (**C6**) aerosol algorithm consists of three separate algorithms that are used to retrieve AOD from the spectral reflectance. These algorithms are the **D**ark **T**arget (**DT**) ocean and land

algorithms, and the **D**eep **B**lue (**DB**) algorithm, which is exclusively applied over bright surfaces such as deserts (Sayer, Hsu, Bettenhausen, & Jeong, 2013).

The fundamental equation for AOD satellite retrievals is given by

$$L\left(\tau_a, \mu_s, \mu_v, \phi\right) = L_0\left(\tau_a, \mu_s, \mu_v, \phi\right) + \frac{\rho_s}{1 - \rho_s \times S(\tau_a)} \mu_s T(\tau_a, \mu_s) T(\tau_a, \mu_v) \quad (2.2)$$

where $\boldsymbol{\tau_a}$ is the atmospheric optical depth resulting from gas molecules and aerosol particles; $\boldsymbol{L_0}$ is the path radiance that is produced by scattering of the particles and gas molecules in the atmosphere; $\boldsymbol{\rho_s}$ is the surface reflectance; $\boldsymbol{S(\tau_a)}$ is an atmospheric backscattering ratio to account the reflection between the surface and atmosphere; $\boldsymbol{T\,(\tau_a, \mu_s)}$ is the transmittance from the ground to the **T**op **O**f the **A**tmosphere (**TOA**); $\boldsymbol{T\,(\tau_a, \mu_v)}$ is the transmittance from the top to the ground; $\boldsymbol{\mu_s}$ and $\boldsymbol{\mu_v}$ are the cosine of the solar zenith angle and the cosine of the view zenith angle, respectively; and $\boldsymbol{\phi}$ is the relative azimuth angle between the solar and view angles. MODIS data were downloaded using https://modis.gsfc.nasa.gov/data/dataprod/

2.1.2.c Meteorological Soundings

The vertical distribution of the physical properties of the atmospheric column, such as pressure, relative humidity, temperature, wind speed, and wind direction are measured through meteorological soundings. Sensors that measure atmospheric parameters directly, such as thermometers, barometers, and humidity sensors, are all

combined in one single instrument called a radiosonde, which is sent aloft on weather balloons.

There are ten stations across the Caribbean basin, including one in the National **W**eather Service **F**orecast **O**ffice in **S**an **Ju**an, Puerto Rico (**WFO SJU**, 18.43°N, 65.61°W) (Figure 2.2), which releases meteorological soundings twice a day. Radiosondes launched at WFO SJU are developed by Vaisala ®. These radiosondes simplify daily observations by receiving, processing, and forwarding meteorological information. The sounding data were accessed via http://weather.uwyo.edu/upperair/sounding.html.

2.1.3 Sampling Strategy

Aerosol optical properties retrieved from CIMEL sun photometers in the AERONET network were analyzed in this study. The sites selected in the AERONET framework were **C**ape **S**an **J**uan (**CSJ**, 18.38°N, 65.62°W) and **L**a **P**arguera (**LP**,18.26°N, 65.59°W) (Figure 2.2). These sites are located on opposite sides of the island of Puerto Rico, at the northeast and southwest corners of the island, respectively. The wind flow over the island is dominated by easterly winds that carry a high concentration of African dust, particularly during the Northern Hemisphere summer (Gioda et al., 2011).

Figure 2.2 Google Earth Image of the sampling sites at Cape San Juan (CSJ), La Parguera (LP), and the National Weather Service Forecast Office in San Juan (WFO SJU).

The main database was the daily mean values of AOD at 440 nm and ***å*** derived in the range 440 – 870 nm between 2004 and 2018. AOD measurements at 440 nm were selected for analysis due to the frequent degradation at 500 nm (Guirado et al., 2014). Nevertheless, the AOD at 550 nm which is more suitable for satellite comparisons, was derived from the AOD at 440 nm and the ***å*** values at 440–870 nm applying the Ångström power law (Ångström, 1929) given by

$$AOD_{550} = AOD_{440} * \frac{550}{440}^{-å} \quad (2.3)$$

The AOD and $\boldsymbol{å}$ measurements were quality assured to ensure the reliability of results (Level 2.0).

Based on the strong correlation between AERONET sites as well as the synoptic nature (> 1000 km) of dust outbreaks, the CSJ and LP time series were combined to reduce temporal gaps in the AOD and $\boldsymbol{å}$ measurements. The correlation between the CSJ and LP was found through Pearson's correlation coefficient (r), which measures the statistical relationship between two variables based on the method of covariance.

*Pearson product-moment (*r*)*

The Pearson product-moment correlation coefficient (r) is a measure of the strength of a linear association between two variables. It has a value between +1 and −1, where 1 is a total positive linear correlation, 0 is no linear correlation, and −1 is a total negative linear correlation. The p-values were then calculated to determine the significance of the results. A p-value ≤ 0.05 means that the results are statistically significant.

$$r = \frac{\sum_{i=1}^{n}(x_i-\bar{x})(y_i-\bar{y})}{\sqrt{\sum_{i=1}^{n}(x_i-\bar{x})^2}\sqrt{\sum_{i=1}^{n}(y_i-\bar{y})^2}} \qquad (2.4)$$

In terms of the characterization of the local atmosphere during dust outbreaks, parameters including the relative humidity ($\boldsymbol{RH}$), potential temperature ($\boldsymbol{\theta}$), and the water mixing ratios ($\boldsymbol{w}$) values were retrieved from meteorological soundings launched at the WFO SJU. Due to the synoptic nature of dust outbreaks, sounding data was retrieved at one single point (WFO SJU) as well.

2.1.4 Statistical Analysis for the Aerosol Optical Properties across the Northeast Caribbean

Based on Dubovik et al. (2002) and Lin and Qing-Cun (2011), the **L**og-**N**ormal (**LN**) distribution is the most appropriate way to characterize the statistical properties such as mean, median, and mode of atmospheric variables including the AOD ($\boldsymbol{\tau}$).

The LN distribution assumes that the logarithms of AOD data are normally distributed. The LN distribution is given by

$$f_{LN}(\tau) = \frac{1}{\tau\sigma\sqrt{2\pi}}\, e^{-(\ln \tau - \mu)^2 / 2\sigma^2},\ \tau > 0 \qquad (2.5)$$

where μ and σ are the mean and standard deviation of the logarithmically transformed variables. The mean and the standard deviation are defined by

$$\mu = e^{\mu + \sigma^2/2} \qquad (2.6)$$

$$\sigma = \sqrt{(e^{\sigma^2} - 1)e^{2\mu+\sigma^2}} \qquad (2.7)$$

Since many atmospheric variables are distinctly asymmetrical and skewed to the right, the **W**eibull (**W**) distribution, which is positively skewed, was also used to characterize AOD and $\boldsymbol{å}$ retrievals.

The W distribution is defined by

$$f_w(\tau) = \frac{\beta}{\alpha}\left(\frac{\tau}{\alpha}\right)^{\beta-1} e^{-\frac{\tau^{\beta}}{\alpha}}, \tau \geq 0 \qquad (2.8)$$

where α and β are the scale and shape parameters, respectively

$$\Gamma\left(1+\frac{1}{\beta}\right)\alpha, \text{where } \Gamma \text{ is the gamma function} \qquad (2.9)$$

$$\beta = \alpha^2\left[\Gamma\left(1+\frac{2}{\beta}\right)\right] - \Gamma^2\left(1+\frac{1}{\beta}\right) \qquad (2.10)$$

The best fit between the LN and W distributions was determined through the **R**oot **M**ean **S**quared **E**rror (**RMSE**).

Root Mean Squared Error (RMSE)

The RMSE is a measure of the differences between the values predicted by a model (LN or W) and the AOD observed values. The lower the values of RMSE, the better is the fit of the data.

$$\text{RMSE} = \sqrt{\frac{\sum_{i=1}^{n}(\text{AOD predicted}_i - \text{AOD observed}_i)^2}{n}} \qquad (2.11)$$

2.2 African Dust Days

2.2.1 Software and Models

2.2.1.a Igor Pro®

Refer to section 2.1.1.a

2.2.1.b Hybrid Single-Particle Lagrangian Integrated Trajectory

The **HY**brid **S**ingle-**P**article **L**agrangian **I**ntegrated **T**rajectory **(HYSPLIT)** was used to determine the origin of the air masses. This tool, developed by the **N**ational **O**ceanic and **A**tmospheric **A**dministration (**NOAA**) and Australia's Bureau of Meteorology, is used for modeling dispersion and deposition of natural and anthropogenic atmospheric plumes. The HYSLIT model is a complete system for computing air parcel trajectories for complex dispersion and deposition simulations (Stein et al., 2015). The individual flow patterns are analyzed through merging trajectories that are near each other, creating clusters.

2.2.2 Frequency and Magnitude of African Dust Days

The thresholds used to identify **A**frican **D**ust **D**ays (**ADD**) were based on values given by Velasco-Merino et al. (2018), Guirado et al. (2014), and Dubovik et al. (2002). These thresholds were AOD (440 nm) values of 0.2 or greater combined with $\boldsymbol{å}$ values (440 -870 nm) of 0.6 or lower.

The **F**requency (**F**) of ADD was defined as the number of ADD divided by the total number of observations (Equation 2.12). Since AOD is proportional to the depth of SAL (Carlson, 2016), the magnitude (**M**) of ADD was defined as the mean AOD during ADD (Equation 2.13). The frequency and magnitude of ADD were calculated individually for June, July, and August and per the climatological season of June-July-August (JJA) between 2004 and 2018.

The number of days per the climatological seasons of March-April-May (MAM), September-October-November (SON), and December-January-February (DJF) was calculated as well.

$$\text{F of ADD} = \frac{\text{Number of ADD}}{\text{Number of Observations}} \tag{2.12}$$

$$\text{M of ADD} = \text{mean AOD during ADD} \tag{2.13}$$

The trends in frequency and magnitude of ADD were calculated using the **R**ate **O**f **C**hange (**R**OC) with time. The ROC values were calculated for June, July and August when the strong seasonal cycle of dust transport into the Caribbean is observed (Prospero et al., 2014). Essentially, the ROC F and ROC M are the ratios between the change in frequency of ADD to change in time (Equation 2.14), and the time rate of change in the magnitude of AOD during ADD (Equation 2.15), respectively.

$$\text{ROC F} = \frac{\Delta\text{frequency of ADD}}{\Delta\text{time}} \tag{2.14}$$

$$\text{ROC M} = \frac{\Delta \text{ magnitude of AOD during ADD}}{\Delta \text{time}} \quad (2.15)$$

2.3 Enhanced Dust Transport into the Northeast Caribbean Basin

2.3.1 Software and Models

2.3.1.a Igor Pro ®

Refer to section 2.1.1.a

2.3.1.b National Center for Environmental Prediction (NCEP) and National Center for Atmospheric Research (NCAR) Reanalysis Tool

The NCEP/NCAR reanalysis tool provides globally gridded data that represents the state of the Earth's atmosphere, incorporating observations and numerical weather prediction model output from 1948 to present (Kalnay et al., 1996). Fields such as temperature, winds and pressure can be downloaded for any given day, month, and year via https://www.esrl.noaa.gov/psd/. Details about parameters downloaded are presented in the next section.

2.3.2 The North African Dipole Intensity Index and the Caribbean Dustiness

To understand the variability in frequency and magnitude of ADD during the summer months, the NAFDI index, as established by Cuevas et al. (2017), was introduced to our analysis.

The NAFDI index is given by

$$NAFDI = \frac{1}{10}\left(\left(\Phi^{y}_{Mo} - < \Phi >_{Mo}\right) - \left(\Phi^{y}_{nNi} - < \Phi >_{nNi}\right)\right) \qquad (2.16)$$

where

- Φ^{y}_{Mo} is the mean geopotential height at 700 mb averaged in the Morocco region in the month "x" of year "y"
- $< \Phi >_{Mo}$ is the mean geopotential height at 700 mb averaged in the Morocco region averaged in the month "x" from 1981 to 2010
- Φ^{y}_{nNi} is the mean geopotential height at 700 mb averaged in the Nigeria region in the month "x" of year "y"
- $< \Phi >_{nNi}$ is the mean geopotential height at 700 mb averaged in the Nigeria region averaged in the month "x" from 1981 to 2010

The values of geopotential heights needed to calculate the NAFDI index were obtained through the NCEP/NCAR reanalysis. The NAFDI index and the AOD monthly anomaly across the Puerto Rico area were correlated through Pearson's correlation coefficient (r) to determine if the NAFDI index modulates dust transport. The AOD (440 nm) anomaly field for each summer month across the Puerto Rico area between 2004 and 2018 was calculated with respect to the AOD mean corresponding to all the occurrences of that summer month.

2.4 Dust as Cloud Condensation Nuclei

2.4.1 Software and Models

2.4.1.a Igor Pro ®

Refer to section 2.1.1.a

2.4.1.b Hybrid Single-Particle Lagrangian Integrated Trajectory (HYSPLIT)

Refer to section 2.2.1.b

2.4.2 Instrumentation Platform: Ice in Clouds - Tropical

The field campaign **Ice** in Clouds - **T**ropical (**ICE-T**) was held during the summer of 2011 with a sampling area (flying path) in the vicinity of the US Virgin Islands and Puerto Rico, although it was based in Saint Croix, US Virgin Islands. Instrumentation on board the **N**ational **S**cience **F**oundation/**N**ational **C**enter for **A**tmospheric **R**esearch (**NSF**/**NCAR**) C-130 included aerosol particle counters and sizers, cloud droplet counters and sizers, radars, and lidars.

This field campaign was intended to analyze chemical, physical, and cloud activating properties of aerosols during dust outbreaks. The ICE-T data can be retrieved through https://data.eol.ucar.edu/master_list/?project=ICE-T

2.4.2.a Aerosol Particle Counters and Sizers

A combination of techniques is required for aerosol measurements because no single instrument can measure particle sizes over the entire range (0.001 to 100 μm). Different measurements yield different information about particles; therefore, multiple instruments are commonly used for aerosols characterization.

Optical measurements classify the aerosol particles based on the scattered light while the electrical measurements classify aerosol particles based on their mobility in an electric field. Optical measurements are focused on size particles between 0.1 to 100 μm. The electrical mobility measurements, however, are focused on the submicron fraction, which is less than 1.0 μm.

Data retrieved during the ICE-T throughout the **A**erosol **P**article **S**pectrometer with **P**olarization **D**etection (**APSPD**), the **H**igh-flow **D**ual-channel **D**ifferential **M**obility **A**nalyzer (**HDDMA**), the **C**loud **C**ondensation **N**uclei **C**ounter (**CCNC**), the **C**ontinuous-**F**low thermal gradient **D**iffusion **C**hamber (**CFDC**) and **F**orward **S**cattering **S**pectrometer **P**robe (**FSSP**) facilitated the characterization of aerosol particle number and size distributions as well as CCN, IN and cloud droplet concentration over Puerto Rico and the vicinity during dust outbreaks. The description of each instrument can be found in the next section.

2.4.2.a.i Aerosol Particle Spectrometer with Polarization Detection

The **A**erosol **P**article **S**pectrometer with **P**olarization **D**etection (**APSPD**), developed by Droplet Measurement Technologies (DMT, Boulder, CO), is designed to measure the light scattered by individual particles that pass through a focused laser beam (Figure 2.3).

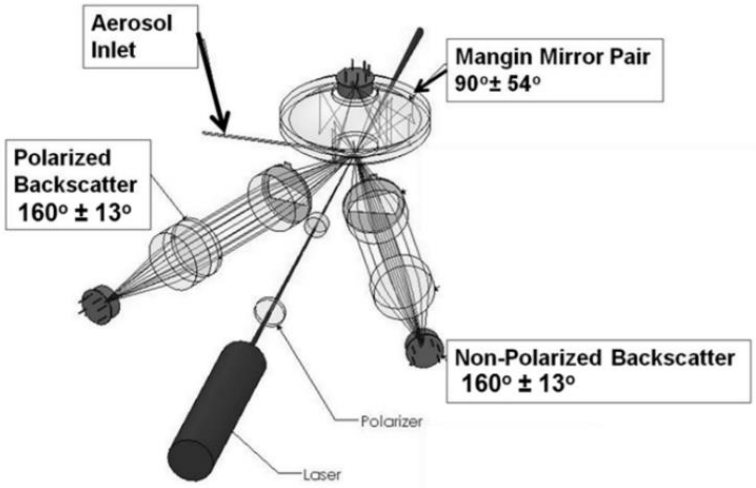

Figure 2.3 Principle of operation for the Aerosol Particle Spectrometer with Polarization Detection (APSPD)(Raga, Baumgardner, & Mayol-Bracero, 2016).

The aerosol particles are introduced into the laser beam with an aerodynamic jet. The light scattered is collected by optics positioned to gather side and backscattered photons. Because aerosol particles are likely to be aspherical and have an unknown refractive index, the diameter that is reported is for a sphere with an index of refraction of water (1.33) that would have produced the measured scattered light. The optical diameter range of the APSPD is 0.5 µm to 20 µm.

2.4.2.a.ii High-flow Dual-channel Differential Mobility Analyzer

The **H**igh-flow **D**ual-channel **D**ifferential **M**obility **A**nalyzer (**HDDMA**) developed by Clarkson University (Potsdam, NY) sizes the particles based on their electrical mobility. The electrical mobility of a particle is defined as the ratio of the constant velocity a charged particle will reach in a uniform electric field to the magnitude of this field (Figure 2.4). The smaller the particle and/or the higher the electrical charge, the higher is the electrical mobility. In contrast to a standard **D**ifferential **M**obility **A**nalyzer (**DMA**), the HDDMA can be operated at high aerosol flow rates to minimize the diffusional loss. The electrical mobility diameter range of the HDDMA is 0.01 to 0.40 μm.

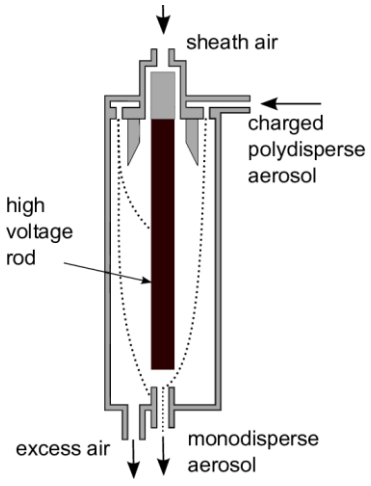

Figure 2.4 Principle of operation for the Differential Mobility Analyzer (DMA) adapted from Holmgre (2011).

2.4.2.b Nuclei Counters

2.4.2.b.i. Cloud Condensation Nuclei Counter

The **C**loud **C**ondensation **N**uclei (**CCN**) counter developed by Droplet Measurement Technologies (DMT, Boulder, CO) measures CCN concentration by drawing an air sample through a vertical column with wetted walls, which provides the water vapor necessary to produce supersaturations with respect to water. The actual partial pressure of water vapor at C equals the partial pressure of water vapor at B (Figure 2.5). However, the temperature at C is lower than at B, meaning there is more water vapor than thermodynamically allowed. Therefore, seeking equilibrium, the supersaturated water vapor condenses on the cloud condensation nuclei to form droplets. Particles that are activated, i.e., grown larger in the process, are detected optically. The optical diameter range of the CCN counter is 0.7 μm to 10 μm.

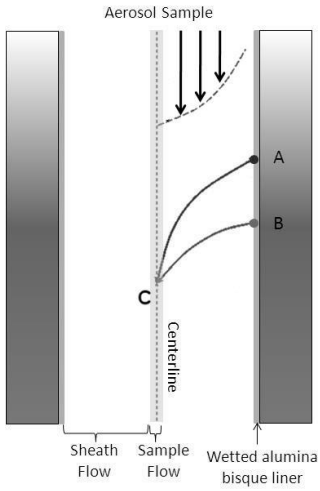

Figure 2.5 Principle of operations Cloud Condensation Nuclei Counter (CCN counter) [http://www.dropletmeasurement.com].

2.4.2.b.ii Continuous Flow Diffusion Chamber

The **C**ontinuous-**F**low thermal gradient **D**iffusion **C**hamber (**CFDC**) developed at Colorado State University (CSU, Fort Collins, CO) measures ice-nucleating aerosol particles through a region of controlled temperature and supersaturation. The chamber is coated with ice and held at different temperatures, which creates the supersaturated conditions. Aerosol particles in the sampled air larger than 2 µm are removed with inertial impactors. The sampled air then flows vertically downward through the chamber, where ice crystals nucleate and grow on active ice nuclei between 3 and 10 µm diameter. At the outlet of the chamber, an optical particle counter detects all particles larger than 0.8 µm. Those particles larger than 3 µm are assumed to be the newly formed ice crystals and comprise the ice nucleus count (Figure 2.6).

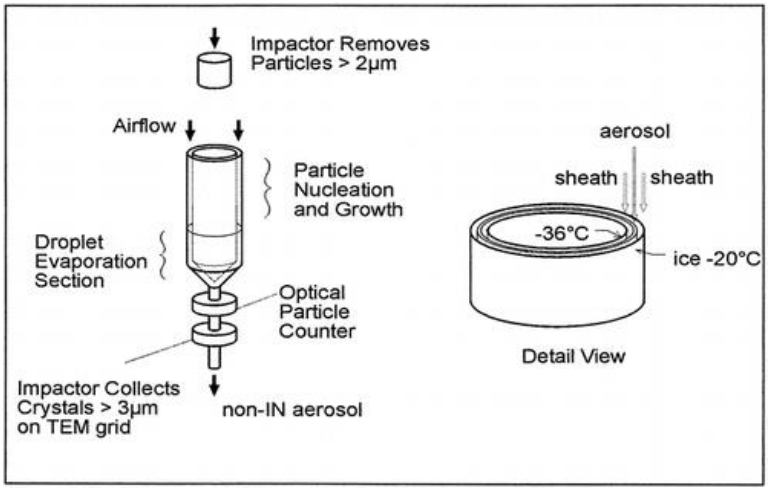

Figure 2.6 Principle of operations of Continuous-Flow thermal gradient Diffusion Chamber (CFDC) (Rogers, DeMott, Kreidenweis, & Chen, 2001).

2.4.2.c Cloud Droplet Counters

2.4.2.c.i. Forward Scattering Spectrometer Probe

The **F**orward **S**cattering **S**pectrometer **P**robe (**FSSP**) developed by Droplet Measurement Technologies (DMT, Boulder, CO) is a single particle counter for airborne droplet measurements in clouds. The cloud droplets pass through sample volume, where they scatter a laser beam (Figure 2.7). The scattered light picked up by detectors allowing the sizes to be determined.

The Model 300 used through this research was intended to size aerosol particles from 0.3 to 20 µm as they pass through the focused laser beam. Bulk quantities such as total droplet number concentrations, liquid water content, or effective droplet radius can also be derived.

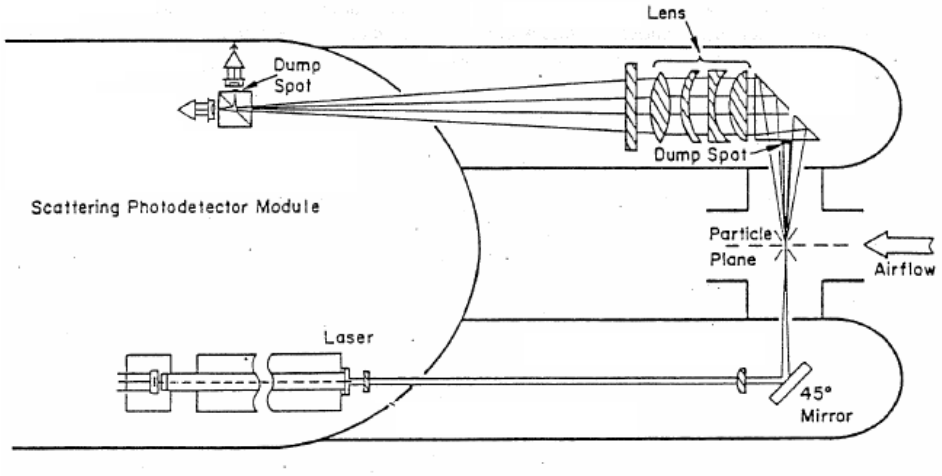

Figure 2.7 Principle of operations of Forward Scattering Spectrometer Probe (FSSP) (Baumgardner, Dye, Knollenberg, & Gandrud, 1992).

2.4.3 Sampling Strategy

There were 13 **R**esearch **F**lights (**RF**s) between July 1st, 2011, and July 30th, 2011 (Table 2.1). Unfortunately, RFs 01, 02, 04, 08, and 09 were rejected for analysis due to equipment malfunctions or missing values.

Table 2.1 Ice in Clouds - Tropical (ICE-T) Research Flights (RFs) analyzed throughout this research.

Research Flight	Start Date and Time	End Date and Time
RF03	July 6th, 1554 UTC	July 6th, 1952 UTC
RF05	July 12th, 1606 UTC	July 12th, 1948 UTC
RF06	July 15th, 1253 UTC	July 15th, 1719 UTC
RF07	July 17th, 1552 UTC	July 17th, 1914 UTC
RF10	July 24th, 1631 UTC	July 24th, 2305 UTC
RF11	July 27th, 1430 UTC	July 27th, 2030 UTC
RF12	July 28th, 1430 UTC	July 28th, 2030 UTC
RF13	July 30th, 1423 UTC	July 30th, 1935 UTC

The aerosol particle size distributions retrieved from APSPD and HDDMA, CCN concentrations retrieved from the CCN counter, IN concentrations retrieved from the CFDC, and cloud droplet concentrations retrieved from the FSSP were all plotted/analyzed to have a better understanding of microphysical properties, particularly during dust outbreaks.

2.5 Rainfall Patterns and Atmospheric Thermodynamics under African Dust

2.5.1 Software and Models

2.1.1.a Goddard Earth Sciences Data and Information Services Center

Analysis and visualization of remote sensing data used throughout this research were produced by the **G**oddard **E**arth **S**ciences **D**ata and **I**nformation **S**ervices **C**enter (**GES DISC**) via the **G**eospatial **I**nteractive **O**nline **V**isualization **AN**d a**N**alysis **I**nfrastructure (**Giovanni**). This powerful tool displays Earth science data retrieved from the **N**ational **A**eronautics and **S**pace **A**dministration (**NASA**) satellites directly through the Internet. Remote sensing data can be displayed in a variety of formats, including area plots, time series, meridional averages, zonal averages, and vertical profiles.

Satellite-based rainfall totals retrieved via Giovanni were used throughout this research. Additional details are found in section 2.5.2.b.

2.5.1.b Igor Pro ®

Refer to section 2.1.1.a

2.5.1.c Standardized Precipitation Index Software

The Standardized Precipitation Index (SPI) software used to calculate the 3-month SPI values was downloaded from

https://drought.unl.edu/droughtmonitoring/SPI.aspx. The SPI values were used to identify wet or dry patterns during June-July-August using land-based rainfall totals.

2.5.2 Sampling Strategy and Rainfall Analysis

2.5.2.a Land-based Rainfall Totals

The **N**ational **W**eather **S**ervice (**NWS**) **CO**operative **O**bserver **P**rogram (**COOP**) at WFO SJU is comprised of 49 weather stations, 8 of them located in the US Virgin Islands, and 41 in Puerto Rico.

Eleven of them were selected for the rainfall analysis based on their location and the lowest percent of missing days. The COOP weather stations selected for analysis are shown in Table 2.2 and Figure 2.8.

Table 2.2 Weather stations from the National Weather Service COoperative Observer Program (COOP) used throughout this research.

Station (Period of record 1980 -2018)	Latitude	Longitude	Percent of Missing Values
Adjuntas Substation	18.1747	-66.7977	1
Arecibo Observatory	18.3494	-66.7525	3
Coloso - Aguada	18.3808	-67.1569	1
Hacienda Constanza - Mayagüez	18.2159	-67.0883	3.5
Manati 2E	18.4308	-66.4661	4.3
Ponce 4E	18.0258	-66.5252	1.5
Lajas Substation	18.0330	-67.0722	1
Guayama 2E	17.9783	-66.0874	2.1
Luis Muñoz Marin Airport	18.4394	-66.0019	0
Juncos	18.2264	-65.9114	2.6
Paraiso, Fajardo	18.3102	-65.6630	1.3

Figure 2.8 Google Earth Image of the study area focused on the Weather Stations from the National Weather Service COperative Observer Program (COOP) used to retrieve rainfall data.

Even though the period of interest comprises 2004 through 2018, SPI calculation requires at least a 30- year record. Therefore, land-based rainfall totals between 1980 and 2018 were downloaded through https://www.ncei.noaa.gov/.

To identify how the seasonal rainfall behaved, the statistical relationship between frequency and magnitude of ADD during June-July-August and the 3-month SPI ending in August (using land-based rainfall totals) was performed through Pearson's correlation coefficient r (equation 2.4)

The 3-month SPI is a more accurate representation of seasonal rainfall because the distribution has been normalized. The 3-month SPI provides a comparison of the rainfall over a specific 3-month period with the rainfall totals from the same 3- month period for all the years included in the historical record (1980 – 2018).

2.5.2.b Satellite-based Rainfall Estimates

The **T**ropical **R**ainfall **M**easuring **M**ission (**TRMM**) is a research satellite designed to analyze the distribution and variability of the tropical rainfall. This sensor provides rainfall rates in inches per hour (in/hr) or inches per day (in/day) with a spatial resolution of 0.25 degrees in latitude and longitude.

The daily area-averaged rainfall totals measured between latitudes 17° and 19°N and longitudes 64° and 78°W were retrieved via https://giovanni.gsfc.nasa.gov/giovanni/. TRMM data were analyzed to obtain an area-averaged rainfall total for the Puerto Rico area.

Once the area-averaged rainfall total was obtained, African Dust Days were classified as -W (Wet) or -D (Dry). If the area-averaged rainfall was less than 0.01 in/day, the ADD was classified as ADD -**D** (**D**ry). If the rainfall, however, was 0.01 in/day or higher, the ADD was classified as ADD - **W** (**W**et).

2.5.2.c Vertical Profile of the Atmospheric Thermodynamics

To understand the daily variations between ADD -D and ADD -W; the vertical profile of the water vapor mixing ratio ***(w)*** and the static energy ($\boldsymbol{E_s}$) at the top of the **C**onvective **B**oundary **L**ayer (**CBL**) (850 mb) were analyzed using meteorological soundings launched at WFO SJU. The sounding data were retrieved at 12 UTC, assuming that the dusty air mass was already over the area, and before any locally induced afternoon showers that could result in a cleaner atmosphere. To increase data availability, the vertical profile of ADD -D and ADD -W were analyzed regardless of the meteorological season.

The ***w*** values in the CBL indicates the mixing occurring between the **M**ixing **B**oundary **L**ayer (**MBL**) (surface to 950 mb) and the dust layer through turbulence processes (Reid et al., 2003) while $\boldsymbol{E_s}$ indicates stability (Petit et al., 2005; Aspliden, 1972). Nevertheless, the vertical profile of other parameters such as relative humidity (***RH***) and potential temperature ($\boldsymbol{\theta}$) were compared with the SAL 1995 - 2002 climatology established by Dunion (2011) (Appendix A: Saharan Air Layer (SAL) 1995 - 2002 climatology and other air masses).

2.5.2.d Advanced Hydrologic Prediction Service

The **A**dvanced **H**ydrologic **P**rediction **S**ervice (**AHPS**) is an interface that displays the 24-h rainfall totals based on radar totals and surface observations, including the COOP stations. These graphical products can be accessed through https://water.weather.gov/ahps/ .

The AHPS tool was used throughout this research as a rainfall data visualization tool. AHPS images were used to confirm rainfall activity during the ICE-T flights.

Chapter 3 RESULTS AND DISCUSSION

3.1 Aerosol Optical Depth and Extinction Ångström Exponent

3.1.1 Correlation between Cape San Juan and La Parguera Sites

There is a strong correlation between CSJ and LP with r values of 0.83 and 0.75 for AOD and ***å***, respectively (Figure 3.1 and 3.2). These results are statistically highly significant with p- values lower than 0.001.

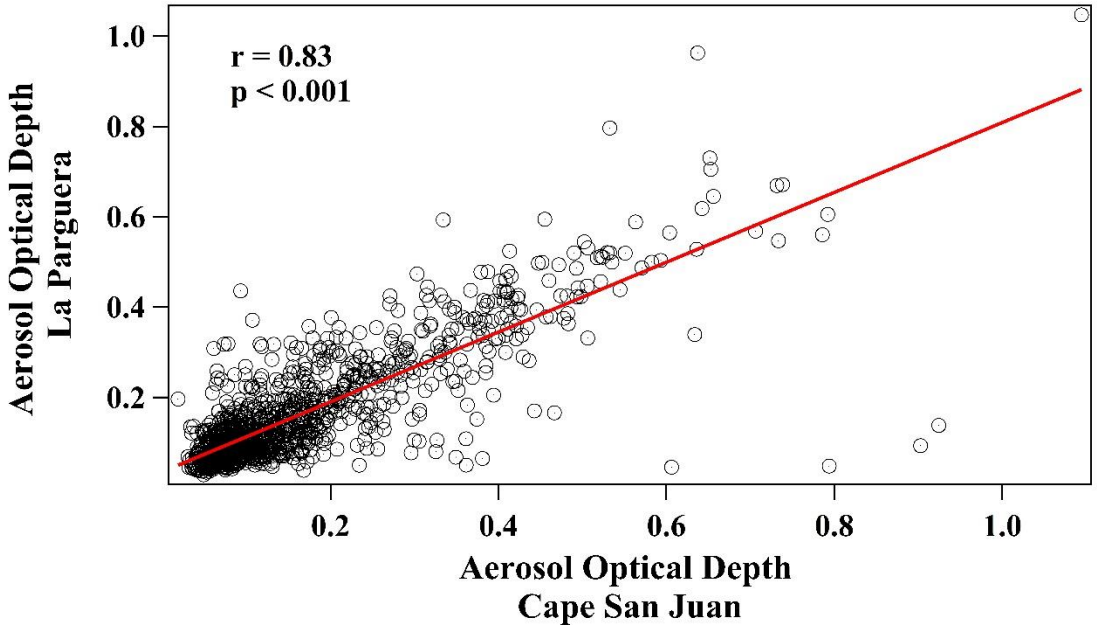

Figure 3.1 Correlation between Aerosol Optical Depth (AOD) AERONET-retrieved at Cape San Juan (CSJ) and La Parguera (LP). Period of Record: 2004 to 2018.

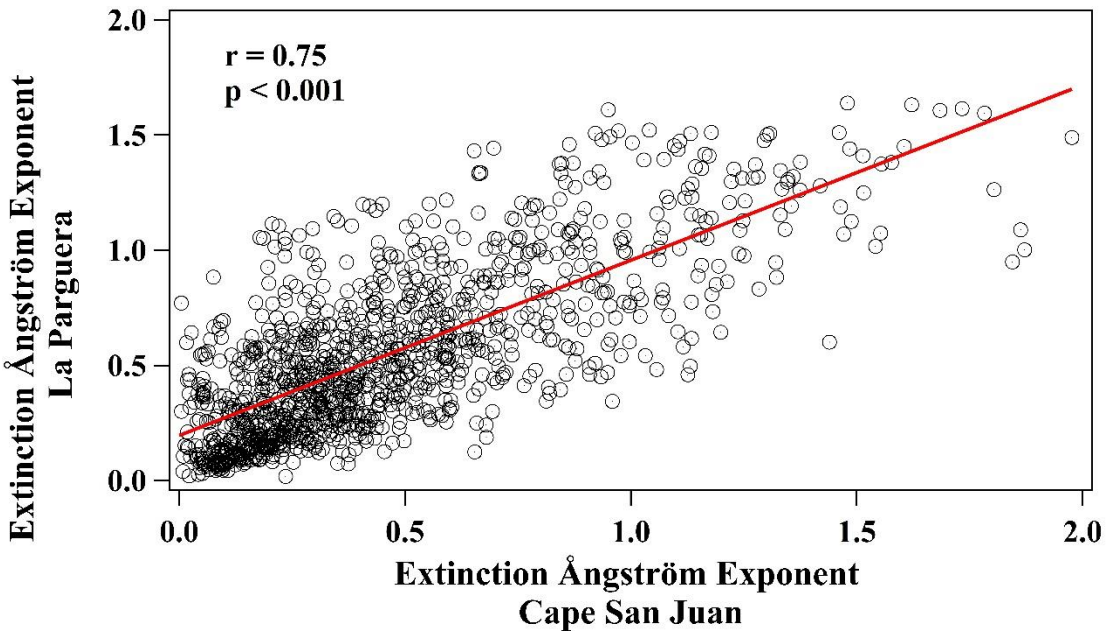

Figure 3.2 Correlation between extinction Ångström exponent (***å***) AERONET-retrieved at Cape San Juan (CSJ) and La Parguera (LP). Period of Record: 2004 to 2018.

Besides the strong correlation between sites, there is as well a strong correlation between the mid-visible AOD retrieved from MODIS and the AOD AERONET-derived over Puerto Rico (CSJ and LP combined time series, now refer as Puerto Rico). The r values between AOD MODIS-retrieved among latitudes 17.8° and 18.7°N and longitudes 65.2° and 67.3°W; and the AOD AERONET-derived over Puerto Rico are 0.84, 0.81 and 0.79 for June, July and August, respectively (Figure 3.3 to 3.5). These results are statistically significant, with p-values lower than 0.05.

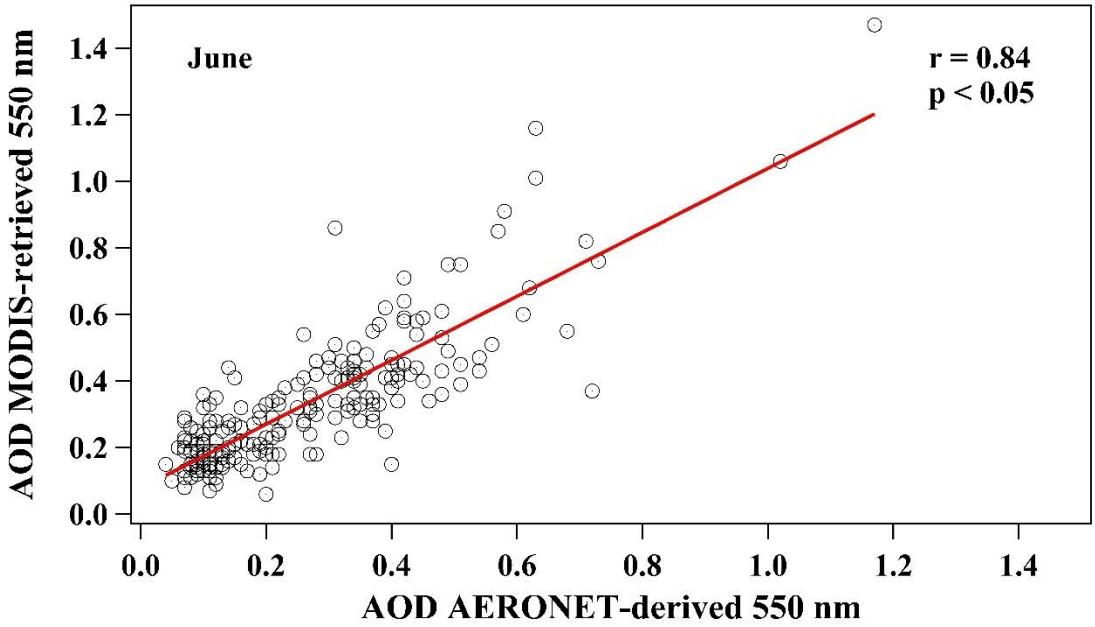

Figure 3.3 Correlation between the mid-visible Aerosol Optical Depth (AOD) MODIS-retrieved and AERONET-derived during June. Period of Record: 2004 to 2018.

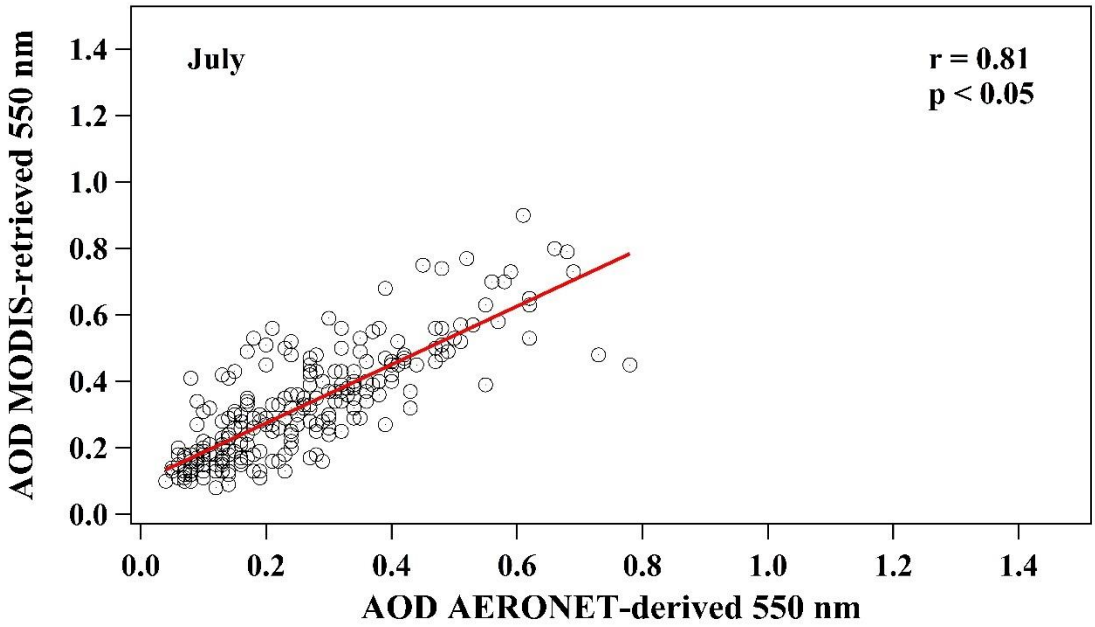

Figure 3.4 Correlation between the mid-visible Aerosol Optical Depth (AOD) MODIS-retrieved and AERONET-derived during July. Period of Record: 2004 to 2018.

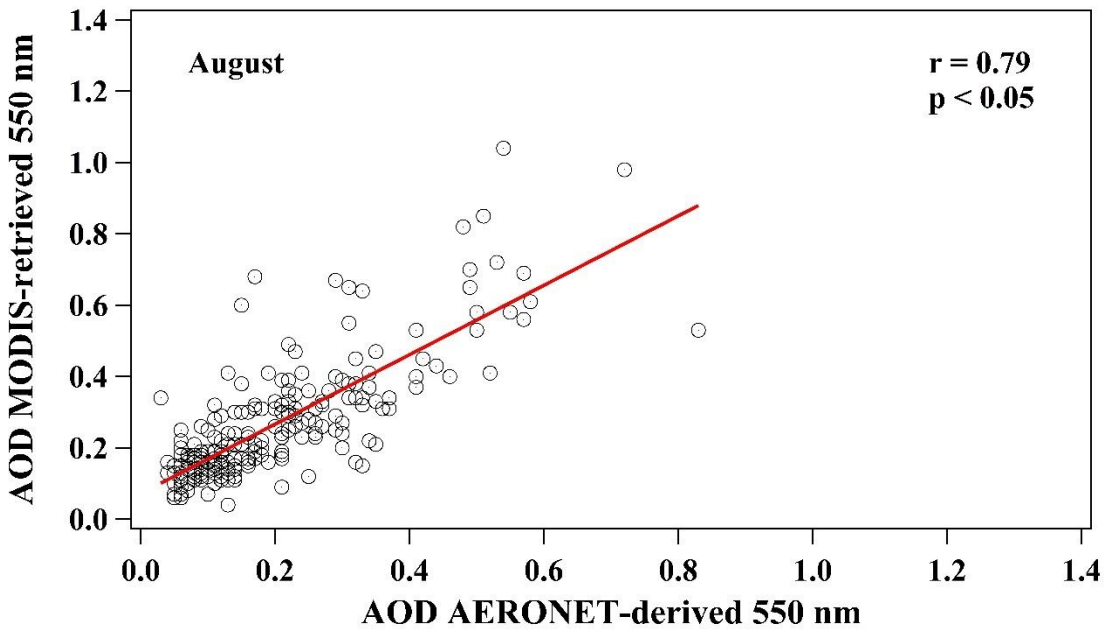

Figure 3.5 Correlation between the mid-visible Aerosol Optical Depth (AOD) MODIS-retrieved and AERONET-derived during August. Period of Record: 2004 to 2018.

3.1.2 Statistical Analysis: Probability Density Function

The frequency of AOD and $\mathring{a}$ values over Puerto Rico between 2004 and 2018 are shown in Figures 3.6 and 3.7. The distribution of both parameters is peaked toward the lower values and skewed to the right.

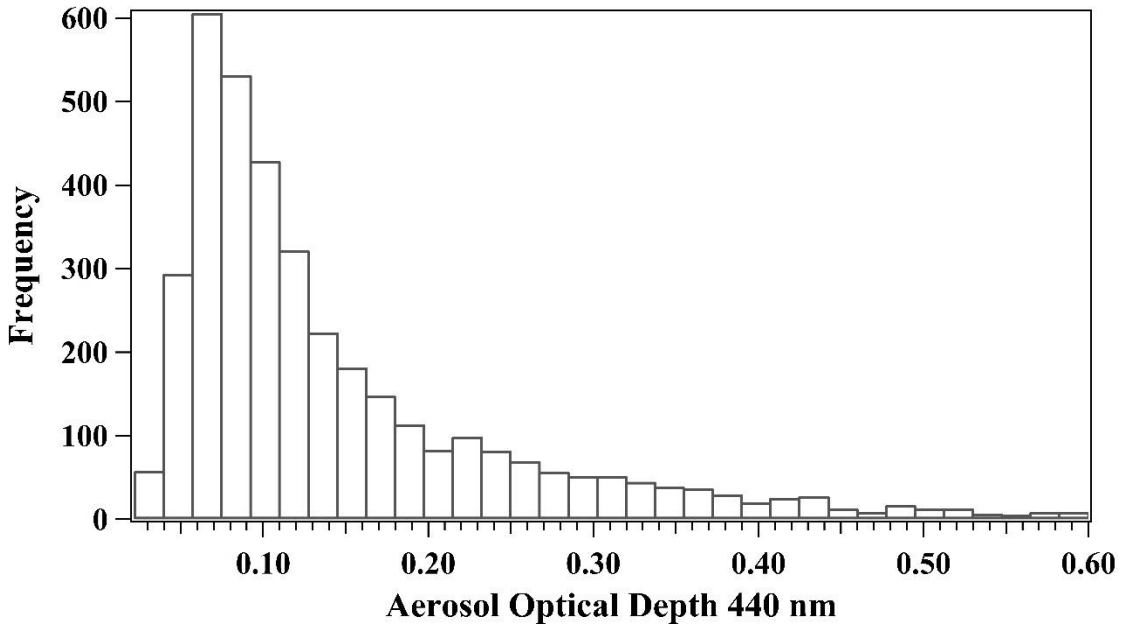

Figure 3.6 Frequency of Aerosol Optical Depth (AOD) retrieved from the Aerosol Robotic Network (AERONET) at La Parguera (LP) and Cape San Juan (CSJ) (combined time series). Period of Record: 2004 to 2018.

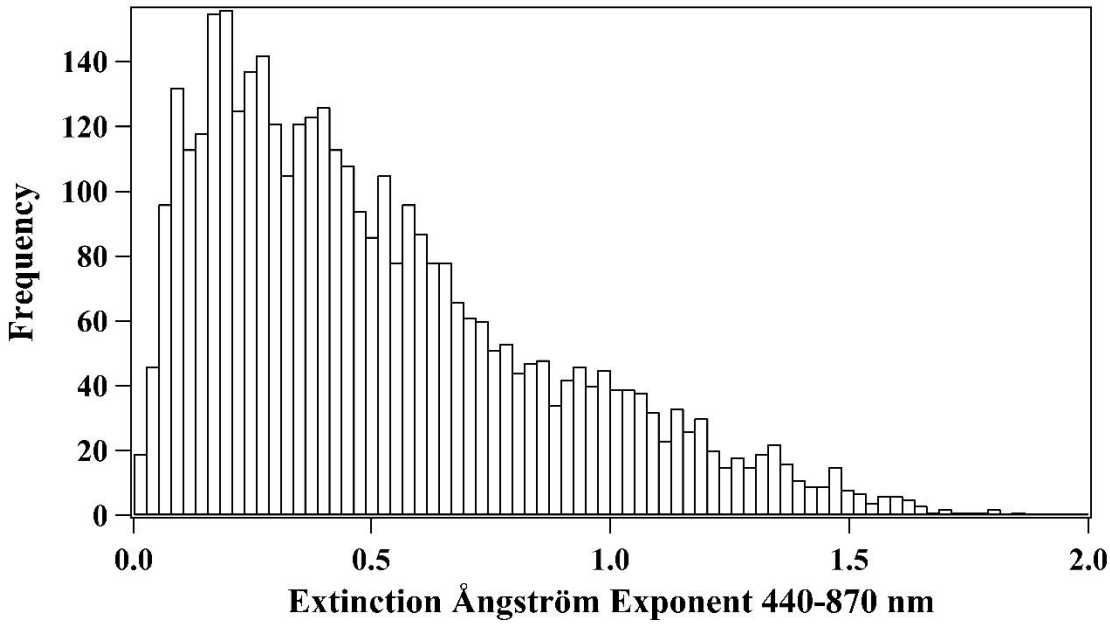

Figure 3.7 Frequency of extinction Ångström exponent (***å***) retrieved from the Aerosol Robotic Network (AERONET) at La Parguera (LP) and Cape San Juan (CSJ) (combined time series). Period of Record: 2004 to 2018.

Based on the RMSE values, the most appropriate distribution to characterize the statistical properties of the AOD and ***å*** population is the LN distribution. The RMSE values corresponding to the LN distribution are 0.19 and 0.46 for AOD and ***å***, respectively (Figure 3.8 and Figure 3.9). These values are much lower than the RMSE values corresponding to the W distribution, which are 0.53 for AOD and 0.64 for ***å*** (Figure 3.8 and Figure 3.9).

For a given AOD or ***å*** sample, the best-fit distribution depends on whether the sampled distribution is heavy- or light-tailed. Although LN and W are heavy-tailed distributions, the LN distribution is more suitable for a 10+ year dataset (Lin & Qing-Cun, 2011).

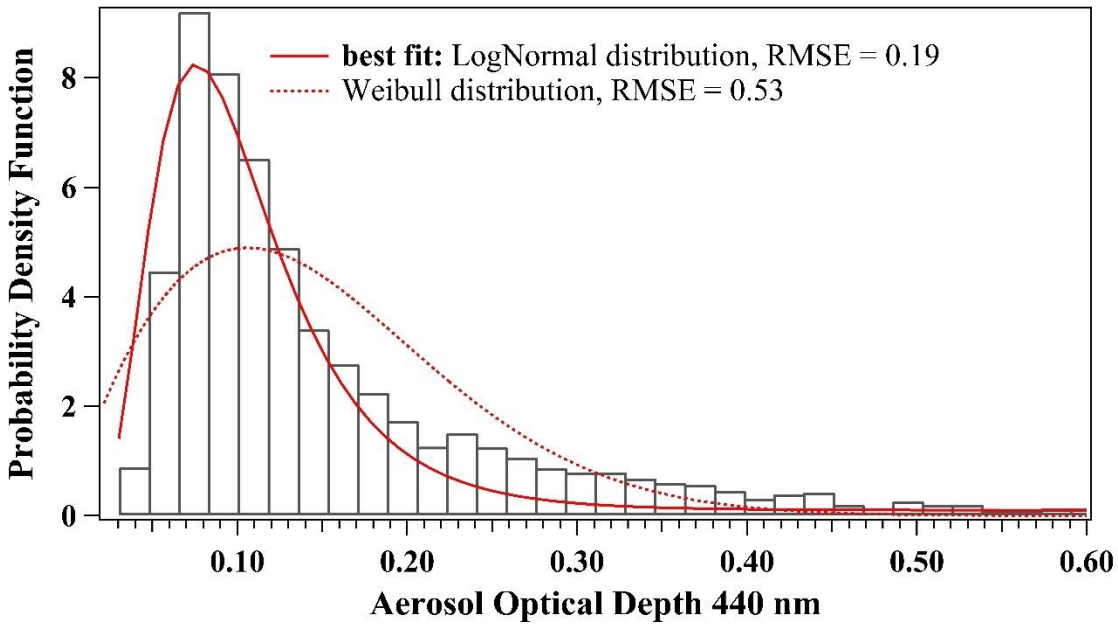

Figure 3.8 Probability Density Function (PDF) of Aerosol Optical Depth (AOD) retrieved from the Aerosol Robotic Network (AERONET) at La Parguera (LP) and Cape San Juan (CSJ) (combined time series). Period of Record: 2004 to 2018.

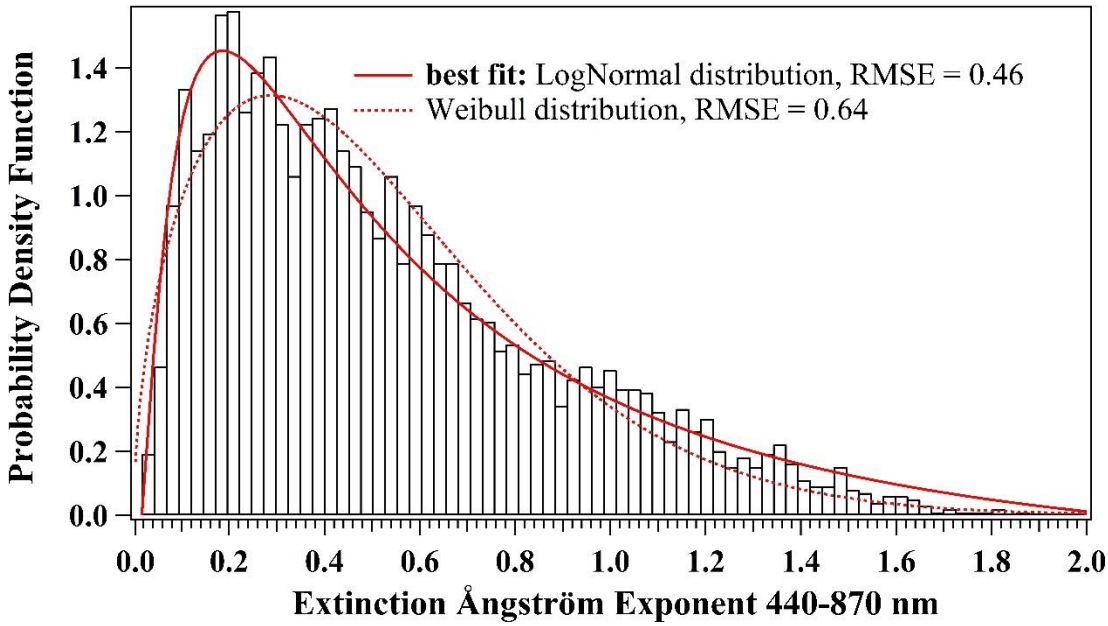

Figure 3.9 Probability Density Function (PDF) of extinction Ångström exponent (***å***) retrieved from the Aerosol Robotic Network (AERONET) at La Parguera (LP) and Cape San Juan (CSJ) (combined time series). Period of Record: 2004 to 2018.

Following the LN distribution, the mean, median, and mode of the AOD population are 0.15, 0.12, and 0.07, respectively. In terms of ***å*** retrievals, the mean, median, and mode are 0.52, 0.42, and 0.28. The mean represents the arithmetic average while the median and mode are the middle and the most common values in the sampled population, respectively.

3.1.3 Climatology

There is a strong seasonality in the AOD behavior with a maximum observed during the Northern Hemisphere summer, June-July-August (Figure 3.10).

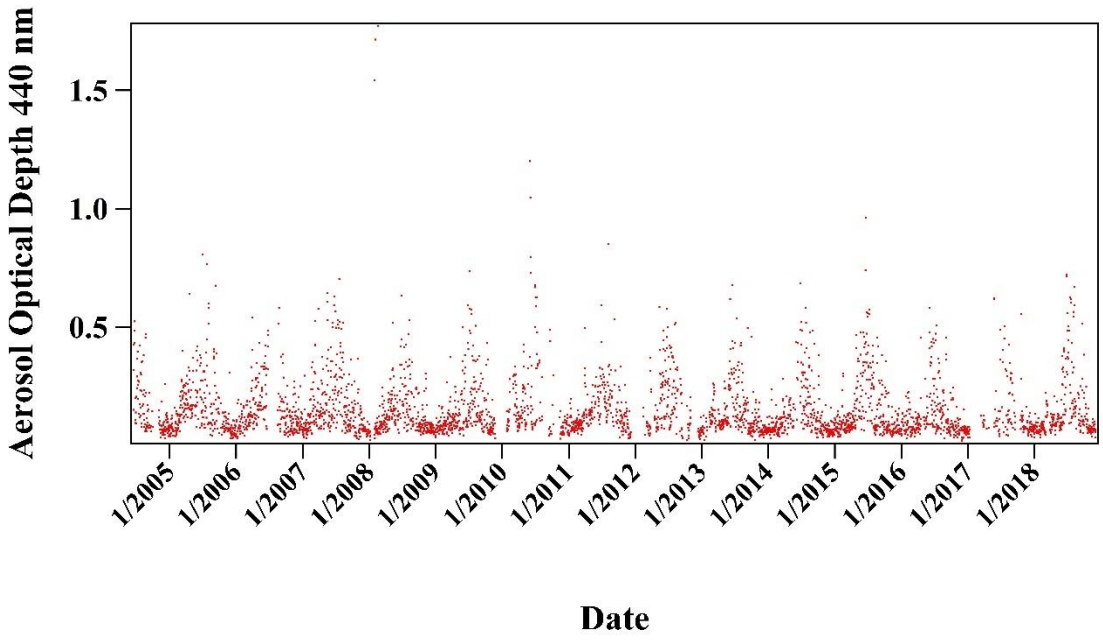

Figure 3.10 Time series of Aerosol Optical Depth (AOD) retrieved from the Aerosol Robotic Network (AERONET) at La Parguera (LP) and Cape San Juan (CSJ) (combined time series). Period of Record: 2004 to 2018.

The highest monthly mean (arithmetic mean) is observed during June, with a value of 0.27 (Figure 3.11). Conversely, the lowest monthly mean is observed during December with an AOD value of 0.07.

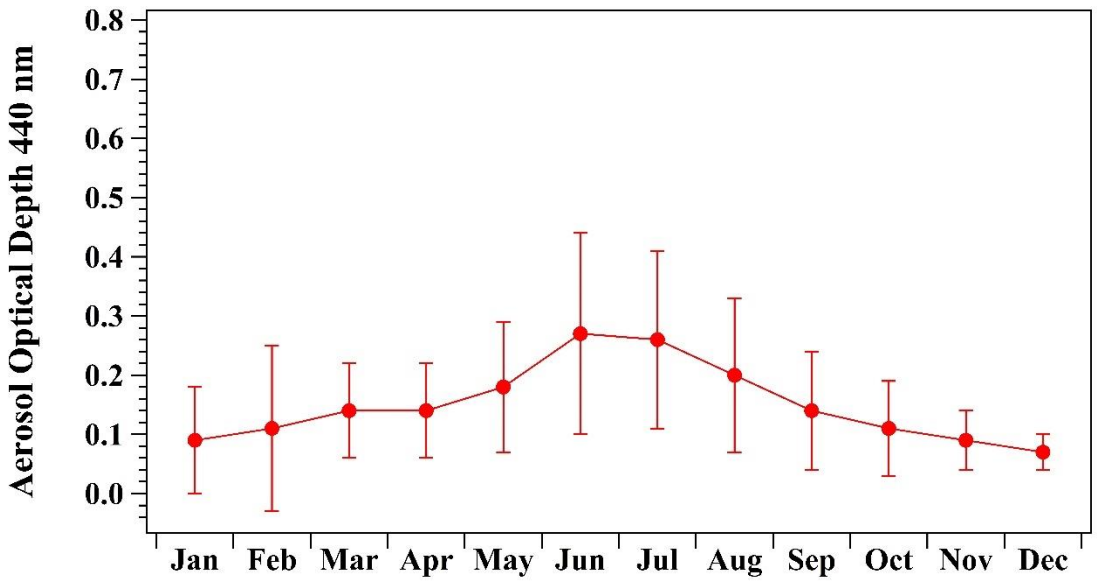

Figure 3.11 Monthly mean and associated standard deviation of Aerosol Optical Depth (AOD) retrieved from the Aerosol Robotic Network (AERONET) at La Parguera (LP) and Cape San Juan (CSJ) (combined series). Period of Record: 2004 to 2018.

In contrast, the ***å*** values retrieved between 2004 and 2018 show larger variability (Figure 3.12) with a maximum during the Spring and a minimum during the Summer (Figure 3.13). This variability is driven by the changes in the aerosol mixture that occur in the Caribbean region from the background values associated with maritime conditions to mineral dust outbreaks and the advection of pollutants (Velasco-Merino et al., 2018).

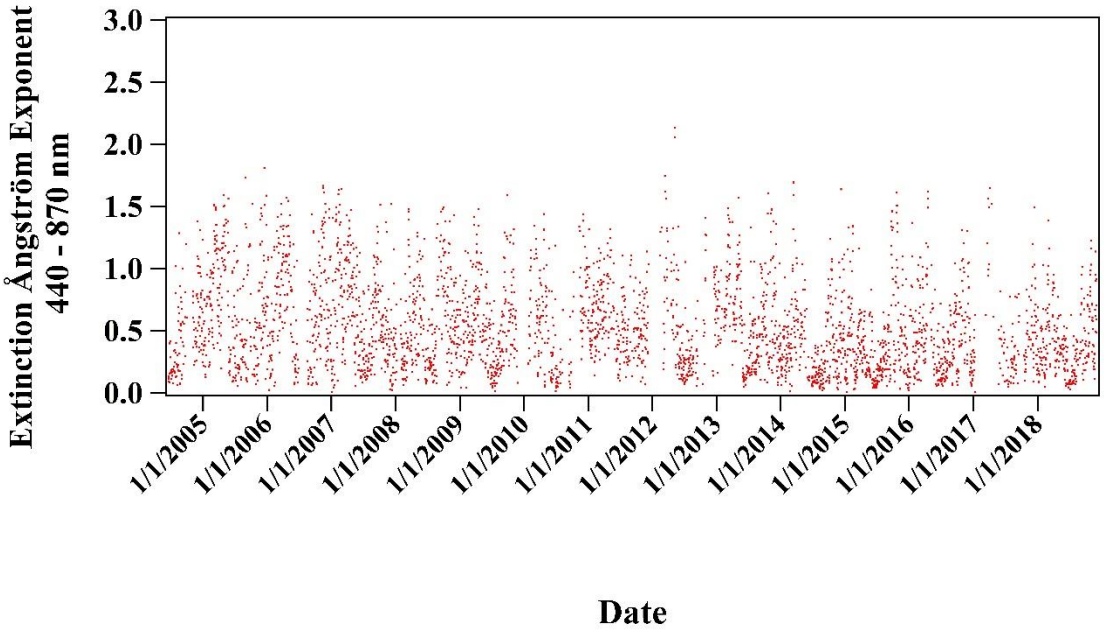

Figure 3.12 Time series of extinction Ångström exponent (***å***) retrieved from the Aerosol Robotic Network (AERONET) at La Parguera (LP) and Cape San Juan (CSJ) (combined series). Period of Record: 2004 to 2018.

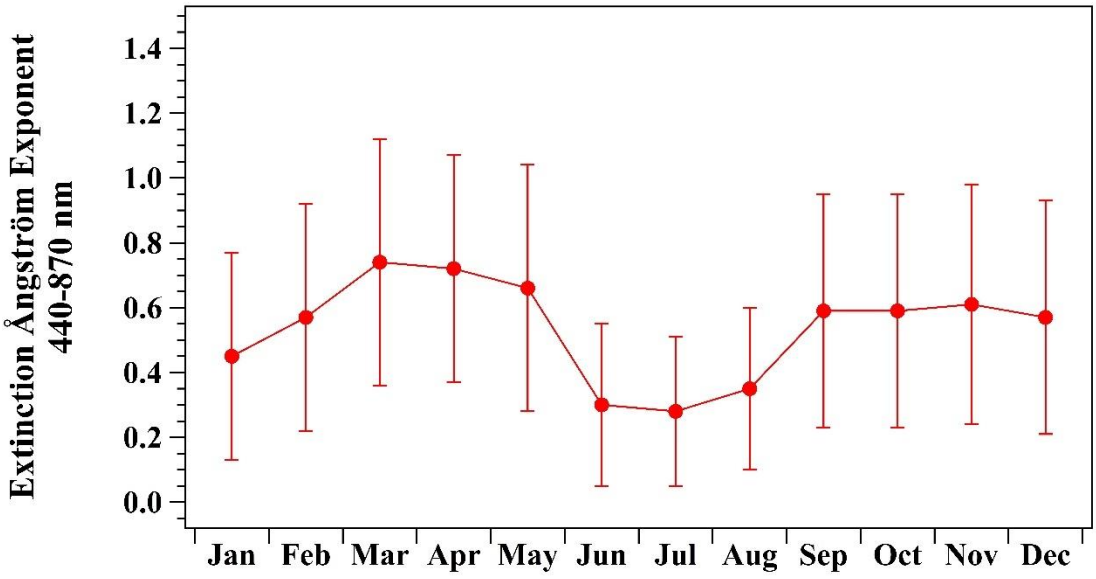

Figure 3.13 Monthly mean and associated standard deviation of extinction Ångström exponent (***å***) retrieved from the Aerosol Robotic Network (AERONET) at La Parguera (LP) and Cape San Juan (CSJ) (combined series). Period of Record: 2004 to 2018.

3.1.4 Aerosol Optical Depth and Extinction Ångström Exponent Thresholds

African **D**ust **D**ays (**ADD**) were identified using the values given by Velasco-Marino et al. (2018), Guirado et al. (2014), and Dubovik et al. (2002) which are AOD ≥ 0.2 and $\boldsymbol{å} \leq 0.6$.

These threshold values are close to the 75th percentile (D75) within the LN distribution (best fit) of the AERONET population retrieved over Puerto Rico. Based on the LN distribution, the D75 corresponds to 0.18 and 0.62 for AOD and ***å***, respectively. Other percentiles such as the 90th (D90), 95th (D95), and 99th (D99) could be used as well to identify **H**igh **D**ust **D**ay (**HDD**), **E**xtreme **D**ust **D**ay (**EDD**) and E**x**ceptional **D**ust **D**ays (**XDD**). These percentiles correspond to AOD values of 0.29, 0.37, and 0.62, respectively.

The threshold values concur with findings from SALTRACE 2013 and PRIDE 2002 field campaigns. AOD values between 0.2 and 0.4, with extreme AOD values exceeding 0.5, were reported during the aforementioned field campaigns (Groß et al., 2016; Reid et al., 2003).

3.1.4 How does AOD ≥ 0.20 look?

On June 11th, 2019, a dust outbreak with AOD value of 0.32, and ***å*** value of 0.12 was observed across the local area (Figure 3.14 and Figure 3.15). Although dustiness decreased the following days, on June 19th, 2019, a second pulse of dusty air arrived with AOD values of 0.25 and ***å*** of 0.22 (Figure 3.14 and Figure 3.16). A much cleaner

atmosphere was then observed on June 23rd with AOD values of 0.11 and ***å*** of 0.19 (Figure 3.14 and Figure 3.17).

Optical properties retrieved during June 2019 correspond to measurements retrieved at LP (Level 1.5). Unfortunately, there is no Level 1.5 data at CSJ, neither Level 2.0 at both sites.

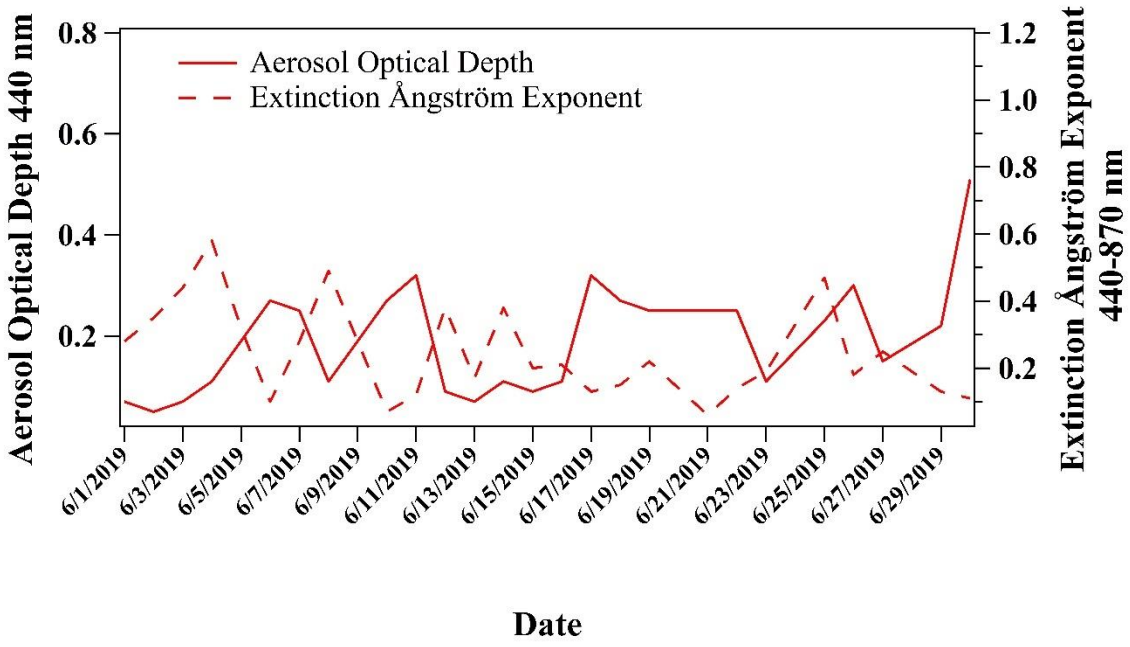

Figure 3.14 Time series of Aerosol Optical Depth (AOD) and extinction Ångström exponent (***å***) retrieved from the Aerosol Robotic Network (AERONET) at La Parguera (LP). Period of Record: June 2019.

Note: *The following photographs were taken at 3 PM each day to confirm the impacts on visibility. There is no filter or any other alteration.*

Figure 3.15 Photograph of the San Juan Metropolitan Area taken from Parque Escorial on June 11th, 2019, 3 PM. Aerosol Optical Depth (AOD) of 0.32 and ***å*** of 0.12.

Figure 3.16 Photograph of the San Juan Metropolitan Area taken from Parque Escorial on June 19th, 2019, 3 PM. Aerosol Optical Depth (AOD) of 0.25 and ***å*** of 0.22.

Figure 3.17 Photograph of the San Juan Metropolitan Area taken from Parque Escorial on June 23rd, 2019, 3 PM. Aerosol Optical Depth (AOD) of 0.11 and ***å*** of 0.19.

As shown in Figure 3.16, haziness begins to be observed if there is an AOD value around 0.25. Therefore, the threshold values in the 0.20s concur as well with impacts on visibility. Nevertheless, to confirm haziness associated with mineral dust, the values of $\boldsymbol{å}$ must be assessed.

3.2 African Dust Days Across the Northeast Caribbean

There are 674 days identified as ADD with AOD ≥ 0.2 and $\boldsymbol{å} \leq 0.6$ between 2004 and 2018. There is an average of 34 ± 9, 5 ± 3, 1 ± 1 and 6 ± 4 ADD per JJA, SON, DJF, and MAM, respectively (Figure 3.18 and Table 3.1).

505 out of the 674 ADD are observed during the summer season (75%). There is an average of 12 ± 6, 13 ± 4, and 8 ± 4 ADD during June, July, and August, respectively. Dates and their corresponding AOD and $\boldsymbol{å}$ values are listed in Appendix B: Repository of African Dust Days.

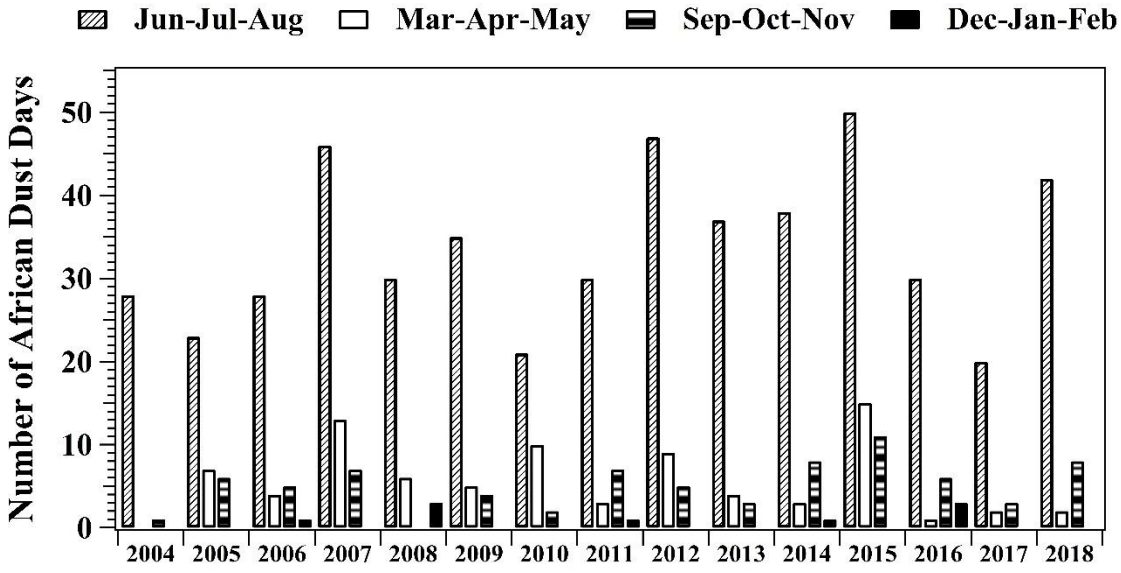

Figure 3.18 Number of African Dust Days (ADD) across Puerto Rico per climatological season between 2004 and 2018**.**

Table 3.1 Number of African Dust Days (ADD) across Puerto Rico between 2004 and 2018.

	Jan	Feb	Mar	Apr	May	Jun	Jul	Aug	Sep	Oct	Nov	Dec
2004	0	0	0	0	0	6	14	8	1	0	0	0
2005	0	0	0	4	3	8	11	4	6	0	0	0
2006	0	0	1	0	3	13	12	3	4	1	0	1
2007	0	0	5	1	7	14	21	11	4	2	1	0
2008	1	2	0	2	4	7	13	10	0	0	0	0
2009	0	0	0	0	5	9	16	10	2	1	1	0
2010	0	0	5	4	1	7	13	1	2	0	0	0
2011	1	0	0	0	3	11	8	11	3	3	1	0
2012	0	0	0	0	9	19	15	13	5	0	0	0
2013	0	0	0	0	4	17	11	9	1	2	0	0
2014	1	0	1	1	1	10	16	12	3	5	0	0
2015	0	0	0	4	11	22	21	7	7	4	0	0
2016	1	2	0	0	1	16	10	4	4	2	0	0
2017	0	0	0	0	2	3	5	12	1	2	0	0
2018	0	0	0	1	1	18	16	8	6	2	0	0

As shown in Figure 3.19, most of the air masses that correspond to ADD during JJA originated over or west of the African continent. Although there are some air masses that originated over the central and eastern Atlantic, mixing and dust intrusion are possible. Therefore, it is not surprising to have a mineral dust signal with high AOD and low $\boldsymbol{\mathring{a}}$ even though the air mass did not originate necessarily near or over Africa.

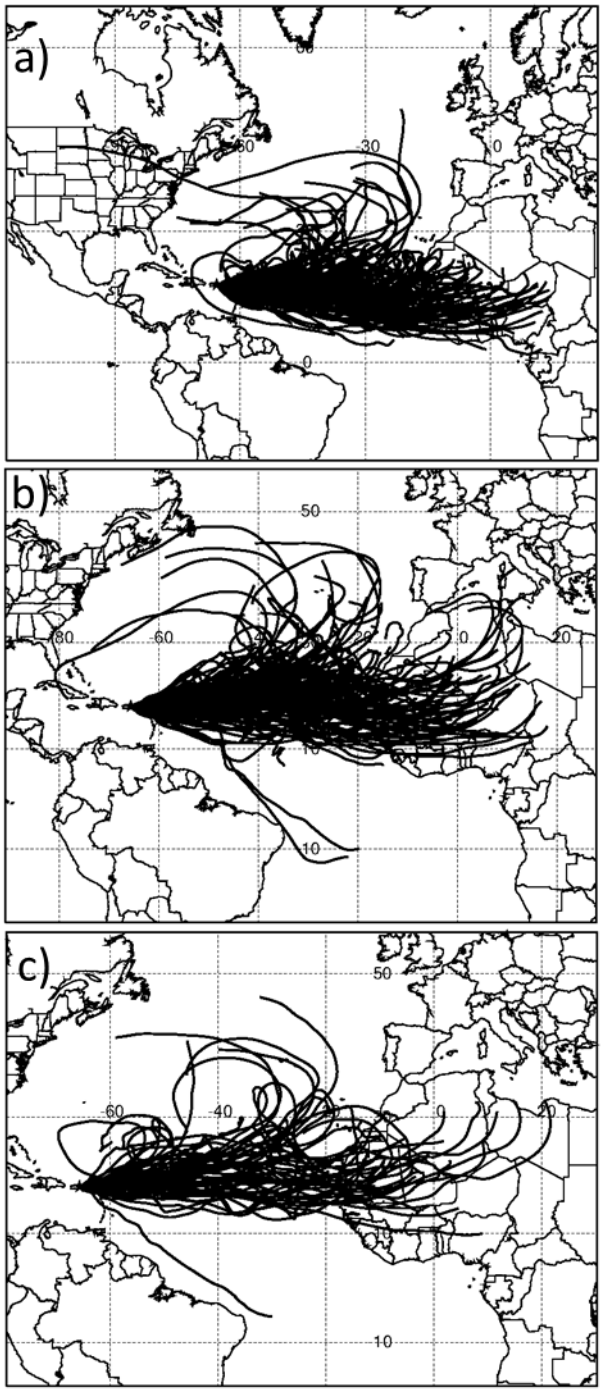

Figure 3.19 10-day HYSPLIT backward trajectories of days classified as African Dust Days (ADD) during the summer months between 2004 and 2018, a) June, b) July, and c) August, respectively.

3.3 Trends in Frequency and Magnitude of African Dust Days

The years with the highest frequency of ADD during June are 2014 and 2015, while the years with the lowest frequency are 2010 and 2017 (Figure 3.20). The highest frequency during July and August are 2007, 2015, and 2011, 2012, respectively.

In terms of magnitude, the highest AOD mean during June is observed during 2010, while the lowest mean is observed in 2011 (Figure 3.20). The highest AOD mean during July and August are observed in 2010 and 2005, respectively.

These results suggest that an increase in the frequency of ADD does not necessarily represent an increase in the magnitude of ADD, or vice versa. During June 2011, there is a peak in frequency, but not in magnitude. An opposite scenario is observed during August 2005 when a peak in magnitude is observed, but not in frequency. The sharp increase in ADD between June 2012 through June 2015 will be discussed in section 3.4.

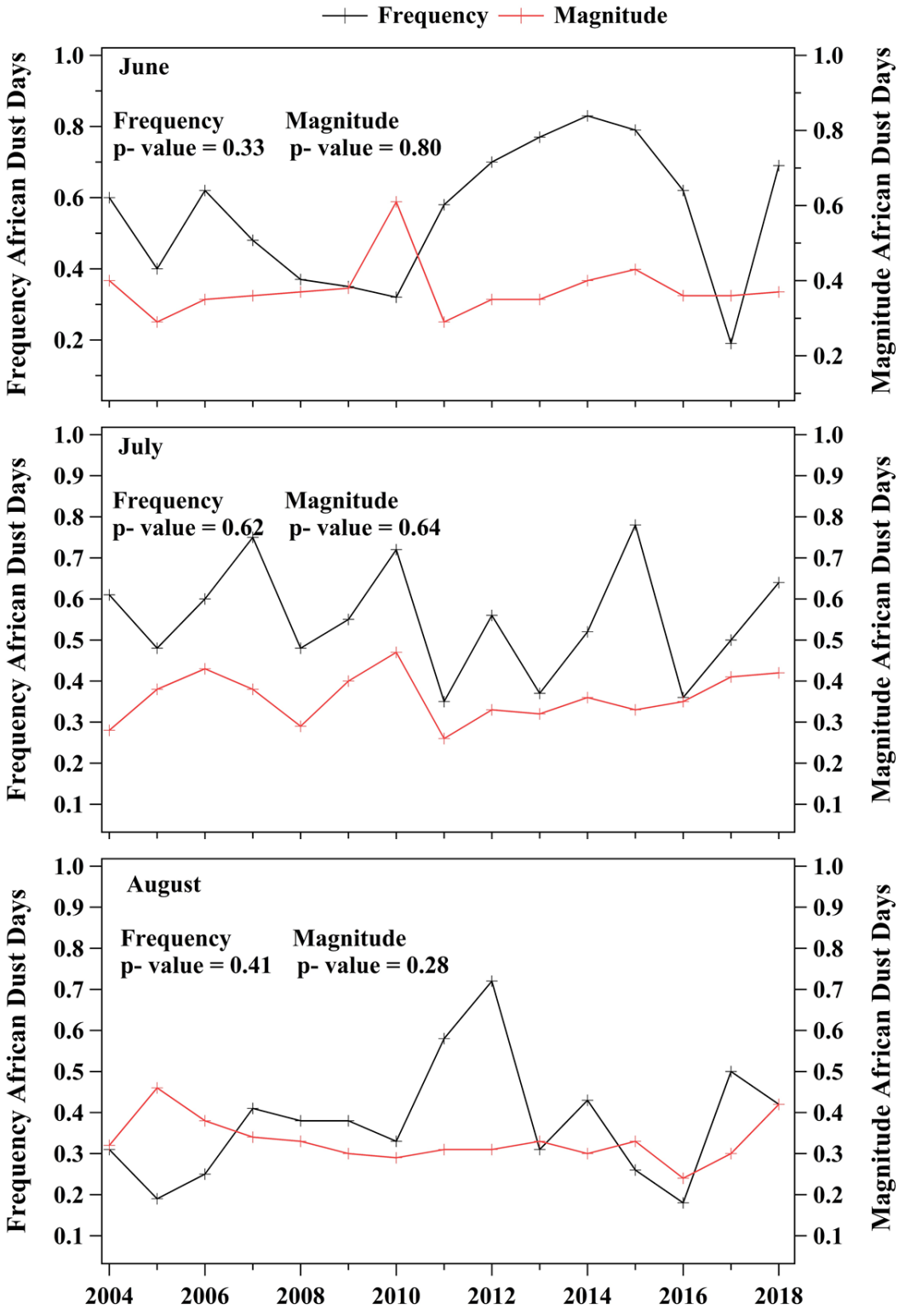

Figure 3.20 Frequency and magnitude of African Dust Days (ADD) during June (top), July (center), and August (bottom) between 2004 and 2018.

Based on the ROC values equal to zero, there are no quantifiable trends in frequency or magnitude of ADD during June, July, or August between 2004 and 2018 (Figure 3.20). These values were confirmed through p- values in the linear regression analysis. The p-values were greater than 0.05, which indicates weak evidence against the null hypothesis. In the formalism of the statistical test, the properties "no trend" or "no change" are known as the null hypothesis.

Results from Ridley et al. (2014) suggest that there is a decreasing trend in the dust concentration during the summer months between 1980 and 2008 at Barbados. Also, Evan et al. (2016) suggest that there have been three periods of anomalous low dust concentration over Africa, which are the 1860s, 1950s, and the 2000s. Therefore, hypothesis #1 has been rejected, and scientific question #1 has been answered.

3.4 North African Dipole Intensity Index and its Correlation with the Northeast Caribbean Dustiness

To understand the variability of ADD across the northeast Caribbean, the NAFDI index, which is an intra-seasonal measure of dust source activation over the Sahara, was introduced into our analysis. There is a moderate negative correlation between the AOD monthly anomaly and the NAFDI index during June with an r of -0.49 (Figure 3.21). The correlation between the AOD monthly anomaly and the NAFDI index became positive during July with an r of *0.52*. The correlation during July is statistically significant, with a p-value lower than 0.05. That is not the case for June with a p-value greater than 0.05.

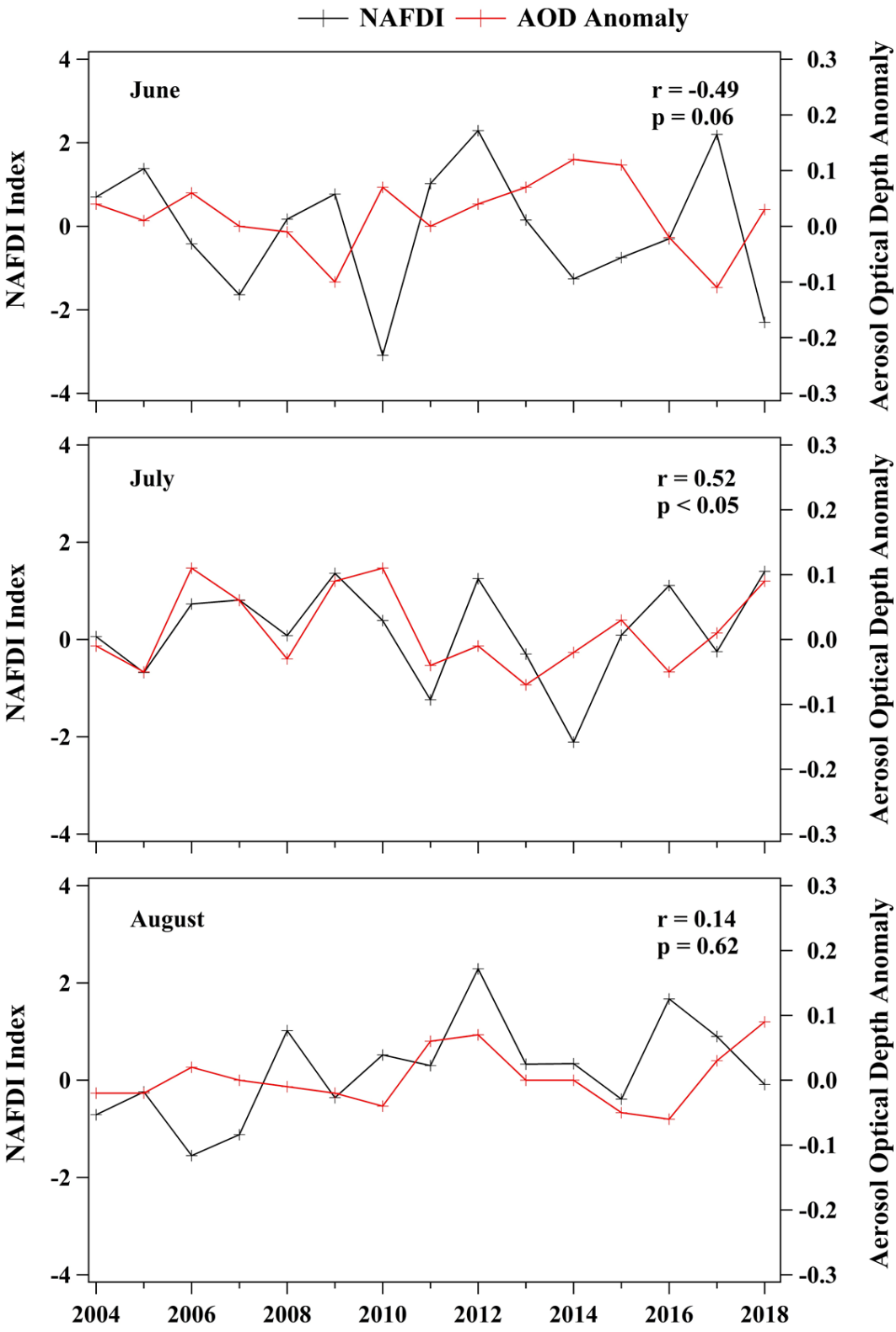

Figure 3.21 Correlation between Aerosol Optical Depth (AOD) monthly anomalies over Puerto Rico and the North African Dipole Intensity (NAFDI) index.

Regardless of the moderate correlation during June (statistically non-significant) and July (statistically significant), qualitatively, the synoptic pattern observed during the years with the highest and lowest frequency of ADD concur with the synoptic pattern described in Cuevas et al. (2017). In addition, a positive correlation during July and a negative correlation during June are reasonable because the NAFDI index is a measure of dust source activation over the Sahara.

Based on the HYSPLIT 10-day backward trajectories and the cluster analysis of the 10-day backward trajectories (Figure 3.19 and Figure 3.22), the air masses that reached the northeast Caribbean during June (64% of the trajectories) on average originated at lower latitudes near or below the 15°N (Sahel/Sub Sahara region). With the northward progression of the ITCZ during the Northern Hemisphere summer (Prospero, 2002), the air masses that reached the northeast Caribbean during July (77% of the trajectories) originated at higher latitudes (Sahara region). The AOD monthly mean retrieved from MODIS at 550 nm shows the northward progression of the dust plume as well (Figure 3.23).

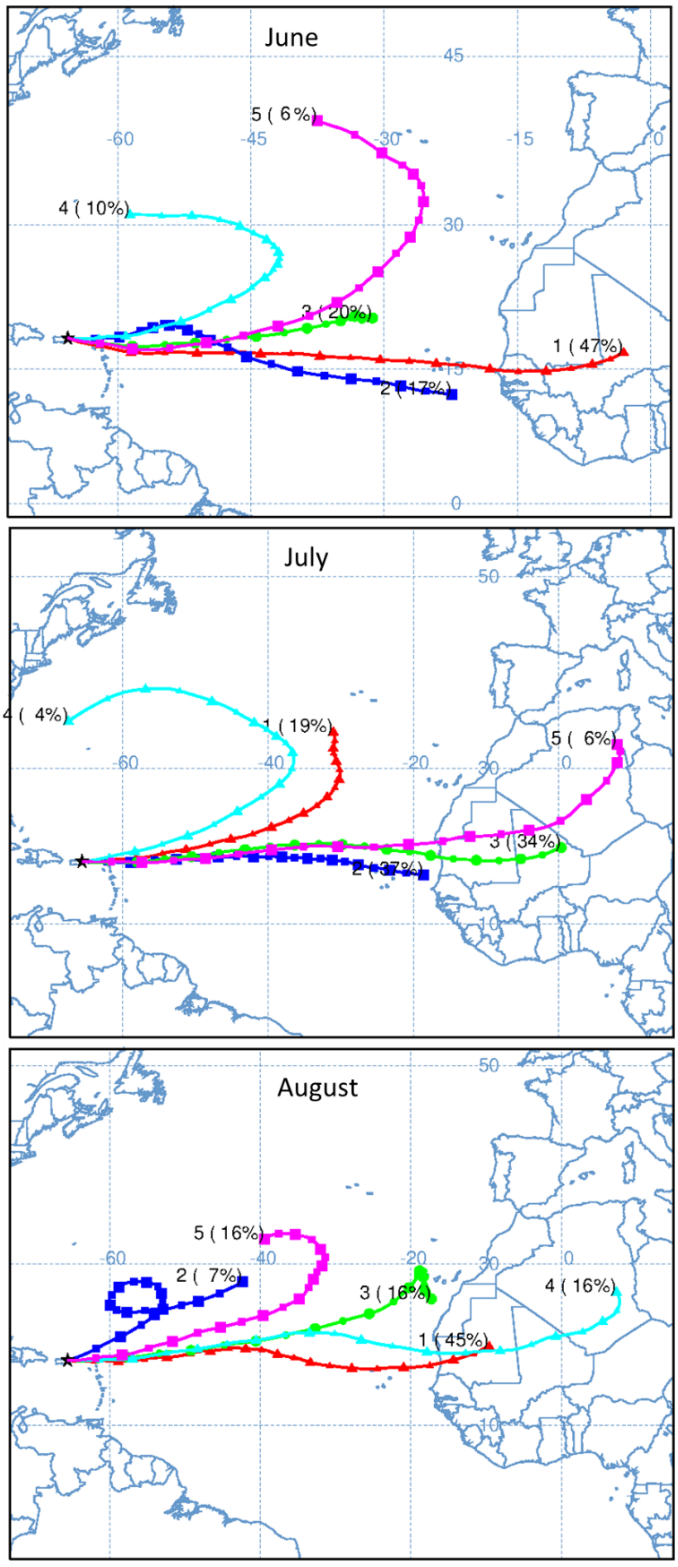

Figure 3.22 HYSPLIT cluster analysis of 10-day backward trajectories of days classified as African Dust Days (ADD) between 2004 and 2018, June (top), July (center), and August (bottom), respectively.

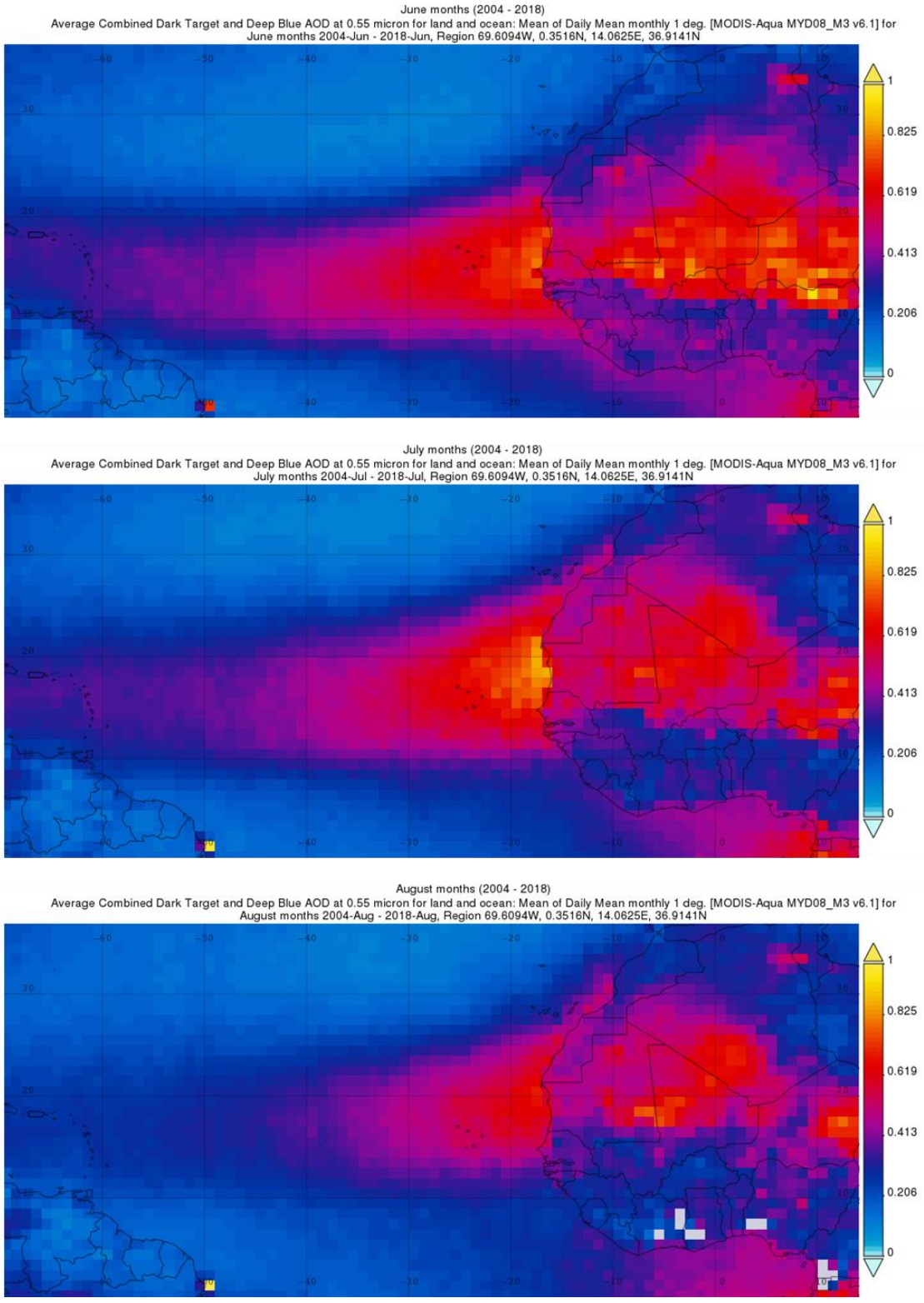

Figure 3.23 MODIS-aqua Aerosol Optical Depth (AOD) monthly average 2004-2018 over the tropical Atlantic, June (top), July (center), and August (bottom), respectively.

In terms of the synoptic patterns, the location of the Azores High and North African anticyclone - which is associated with the NAFDI phase - were plotted based on the highest and lowest frequency of ADD. If the frequency of ADD exceeded the 90th/10th percentile, it was considered a year with the highest/lowest frequency, respectively.

The synoptic pattern during the months of June with the highest and lowest frequency of ADD was similar to the pattern observed during the negative NAFDI phase with a trough displacing the Azores High from the North African anticyclone (Figure 3.24). During the years with the highest frequency of ADD, however, a stronger pressure gradient was observed over Western Africa, which flattens the western side of the North African anticyclone (Figure 3.24a). This resulted in stronger easterly winds at 700 mb below the 15°N (Figure 3.25a).

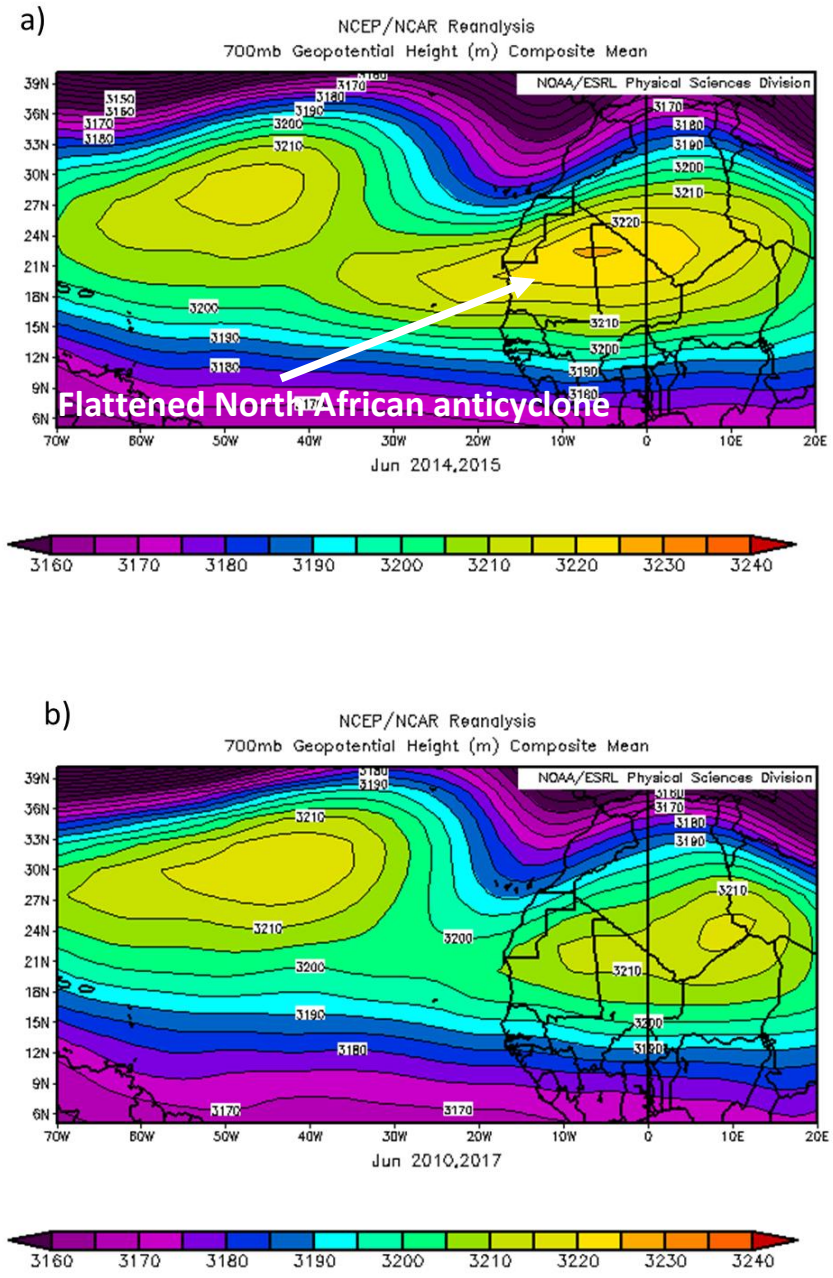

Figure 3.24 Geopotential heights at 700 mb from NCEP/NCAR reanalysis during June: (a) years with the highest frequency of African Dust Days (ADD) and (b) years with the lowest frequency of ADD, respectively.

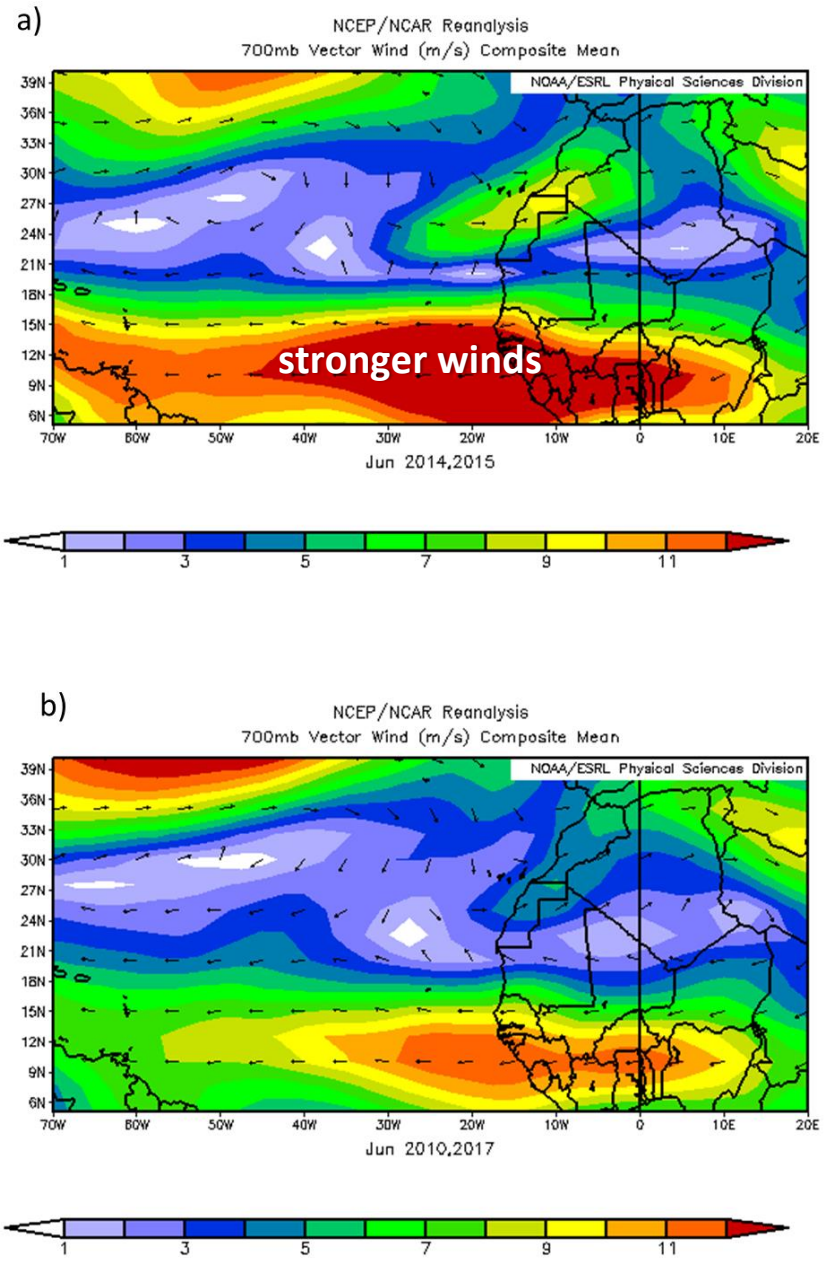

Figure 3.25 Winds at 700 mb from NCEP/NCAR reanalysis during June: (a) years with the highest frequency of African Dust Days (ADD) and (b) years with the lowest frequency of ADD, respectively.

The aforementioned synoptic pattern explains the sharp increase as well in ADD observed between June 2011 and June 2015 (Figure 3.20). Figure 3.26(a) shows a deeper trough with a stronger pressure gradient west of Western Africa, combined with a much more elongated Azores High. This resulted in a flattened North African anticyclone strengthening easterly wind at 700 mb below the 15°N (Figure 3.26 (c)).

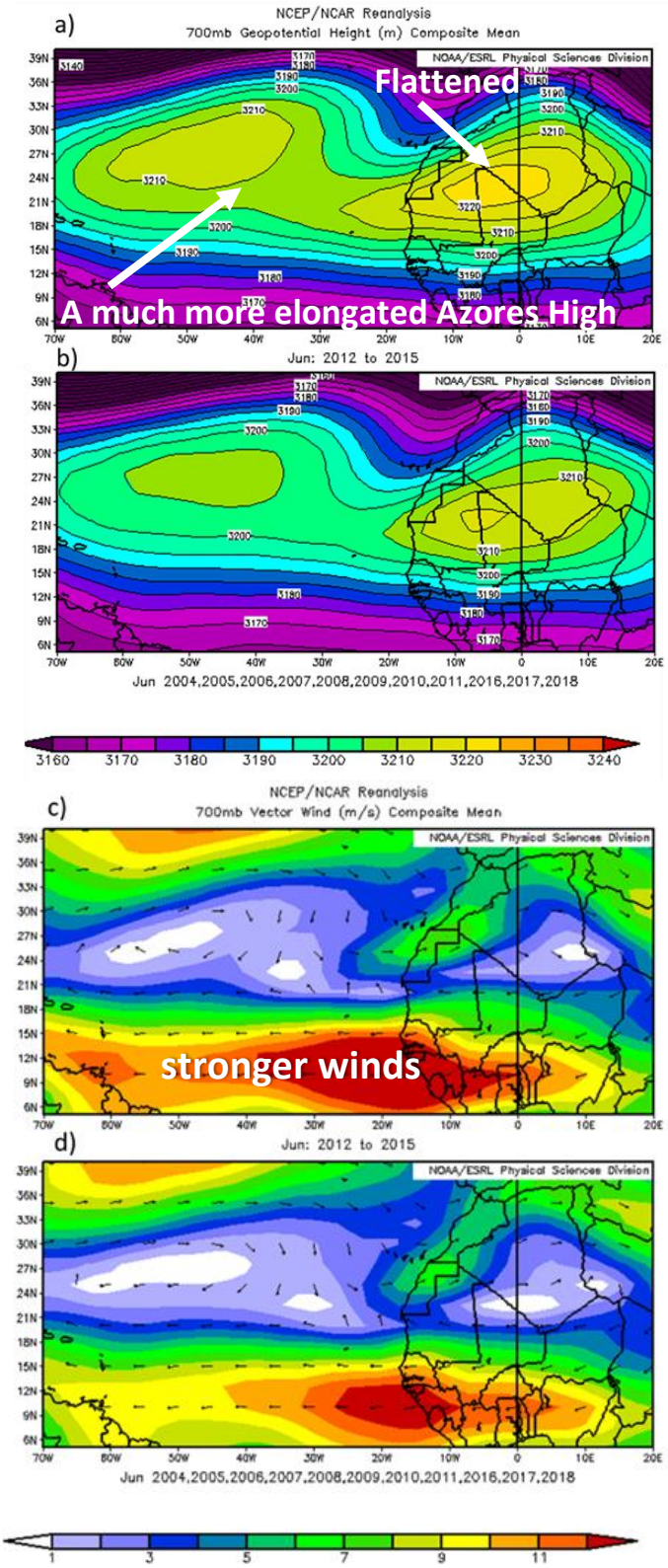

Figure 3.26 (a) and (c) Geopotential heights and winds at 700 mb June 2012 to 2015. (b) and (d) Geopotential heights and winds at 700 mb during the months of June except 2012 to 2015.

As the ITCZ shifts northwards and reaches its most northern position, the synoptic pattern which enhances dust transport into the northeast Caribbean changes. The Azores High and the North African anticyclone merged at 700 mb during the month of July with the highest frequency of ADD (Figure 3.27a). This follows the synoptic pattern corresponding to the positive NAFDI phase with strengthening easterly winds at 700 mb between 15˚ and 20˚N (Figure 3.28a).

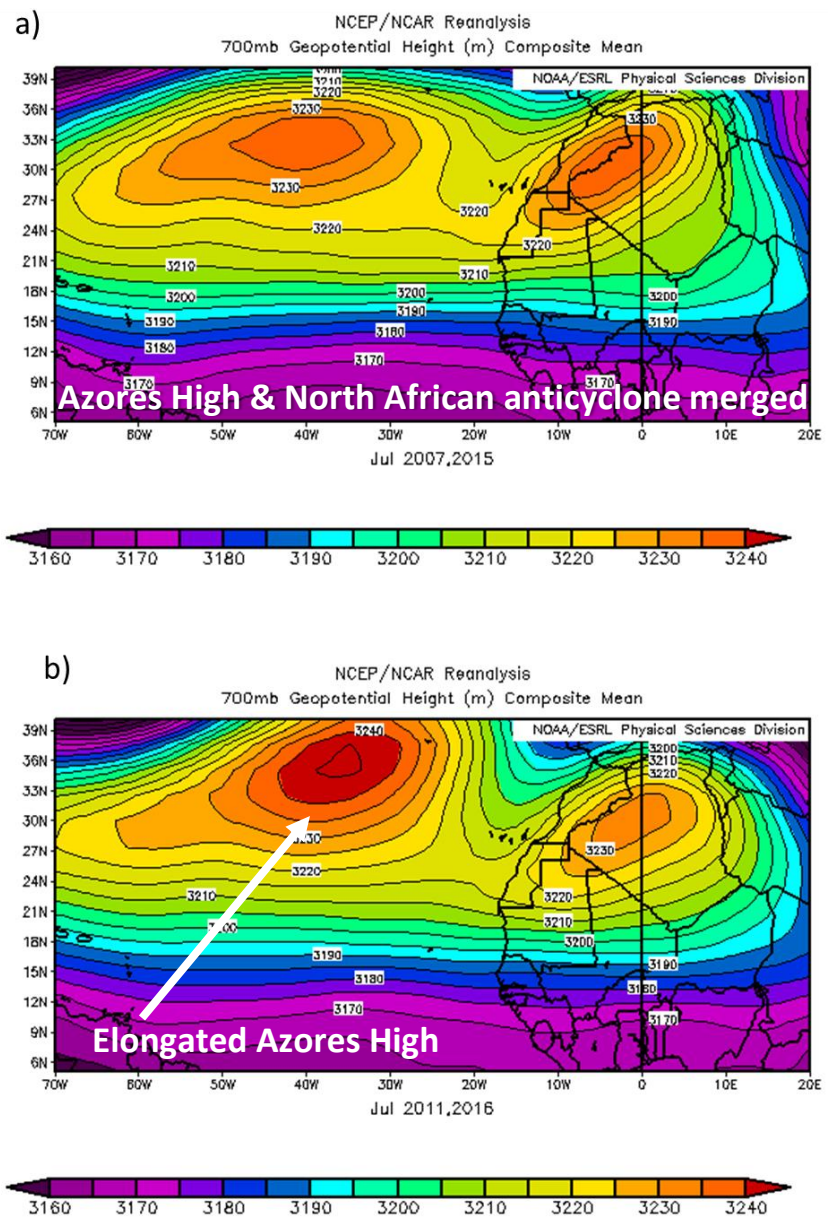

Figure 3.27 Geopotential heights at 700 mb from NCEP/NCAR reanalysis during July: (a) years with the highest frequency of African Dust Days (ADD) and (b) years with the lowest frequency of ADD, respectively.

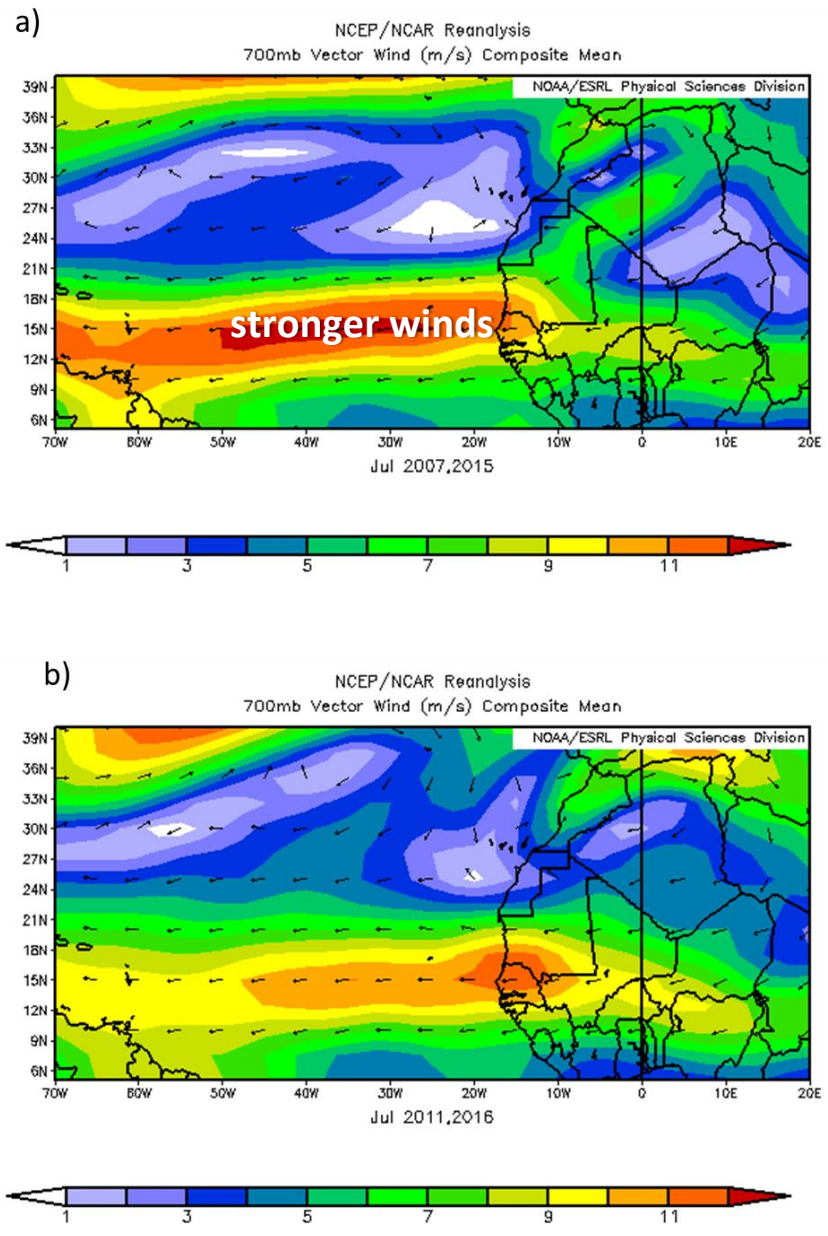

Figure 3.28 Winds at 700 mb from NCEP/NCAR reanalysis during July: (a) years with the highest frequency of African Dust Days (ADD) and (b) years with the lowest frequency of ADD, respectively.

Therefore, the synoptic pattern that enhances dust transport towards the Atlantic and into the northeast Caribbean from the Sahel/Sub Sahara region, which is the primary dust source early in the summer, corresponds to a stronger pressure gradient west off Western Africa combined with a much more elongated Azores High. This flattens the western side of the North African anticyclone, which strengths easterly wind at 700 mb over the Sahel/Sub Sahara region.

As the ITCZ moves northward, the Sahara Desert becomes active and the positive NAFDI phase could be applied to describe the enhanced dust transport. The synoptic pattern which corresponds to enhanced dust transport from the Sahara toward the Atlantic and into the northeast Caribbean is the merging of the Azores High and the North African anticyclone with strengthening easterly winds at 700 mb between 15˚ and 20˚N.

There was no surprise to observe a positive correlation ($r = 0.14$) between the AOD monthly anomaly and the NAFDI index during August (Figure 3.21). This is because July and August are similar in terms of synoptic pattern over Africa. However, the weaker correlation (statistically non-significant) between the NAFDI index and the AOD anomaly is likely to be associated with the local rainfall patterns, which include an increase in the tropical cyclone activity. Climatologically speaking, June and July are drier months compared with August (Martinez, Goddard, Kushnir, & Ting, 2019).

Nevertheless, the months of August with the highest and lowest frequency of ADD concur with the synoptic pattern described in Cuevas et al. (2017). Figure 3.29(a) shows the Azores High and the North African Anticyclone merged and stronger easterly

winds between 15˚ and 20˚N (Figure 3.30(a)), while Figure 3.29(b) shows an elongated Azores High.

This answers scientific question #2. It is possible to identify patterns that enhance dust transport into the northeast Caribbean, the Azores High and the North African anticyclone play a major role based on their location and proximity.

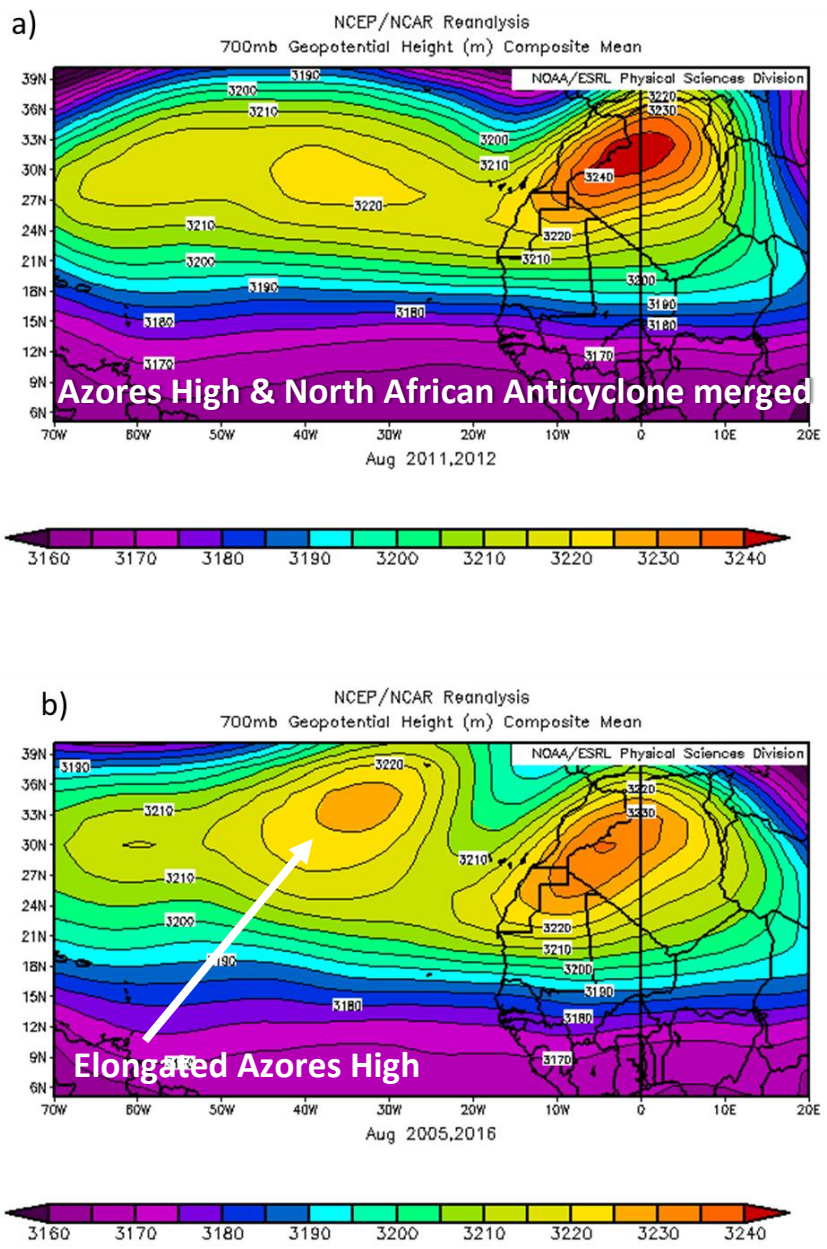

Figure 3.29 Geopotential heights at 700 mb from NCEP/NCAR reanalysis during August: (a) years with the highest frequency of African Dust Days (ADD) and (b) years with the lowest frequency of ADD, respectively.

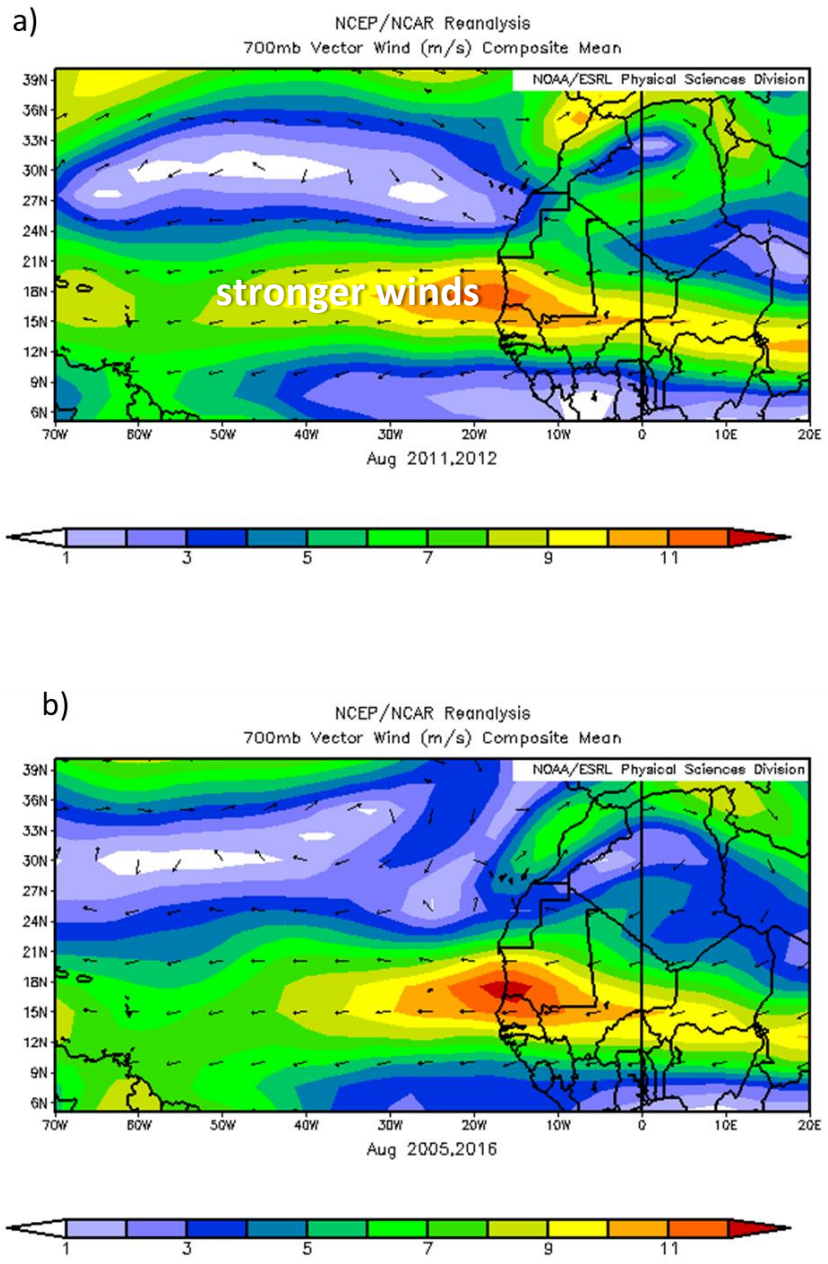

Figure 3.30 Winds at 700 mb from NCEP/NCAR reanalysis during August: (a) years with the highest frequency of African Dust Days (ADD) and (b) years with the lowest frequency of ADD, respectively.

3.5 Aerosol Particle Size and Number Distributions

Based on the threshold values to identify ADD (AOD ≥ 0.20 and **å** ≤ 0.6), only three research flights during the ICE-T field campaign were performed during dust outbreaks. Those were RF03, RF06 and RF13 with AOD and **å** values of 0.26, 0.29, 0.23 and 0.33, 0.57, 0.24, respectively. The flight paths during RF03 and RF06 were east of Puerto Rico while the flight path for RF13 was southeast of Saint Croix/south of Puerto Rico (See Appendix C: Ice in Clouds - Tropical (ICE-T), Supplemental Information).

The air masses analyzed during RF03, RF06, and RF13 originated on the west coast of the African continent, as it is shown in Figures 3.31 to Figure 3.33.

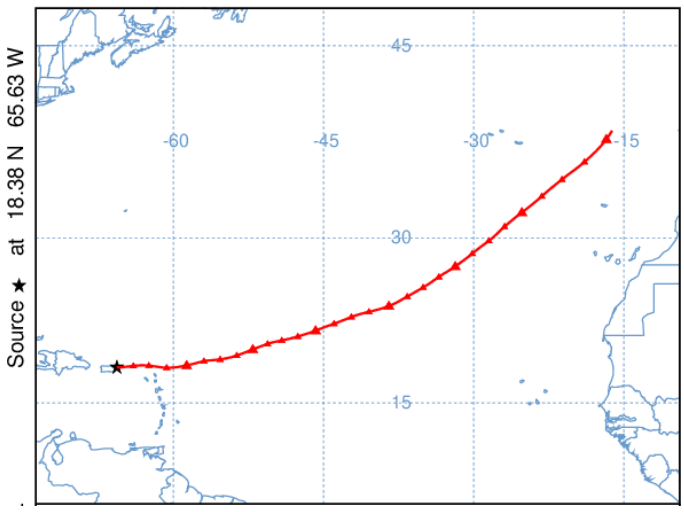

Figure 3.31 HYSPLIT 7-day backward trajectory of air mass arriving on July 6th, 2011, corresponding to Research Flight 03 (RF03).

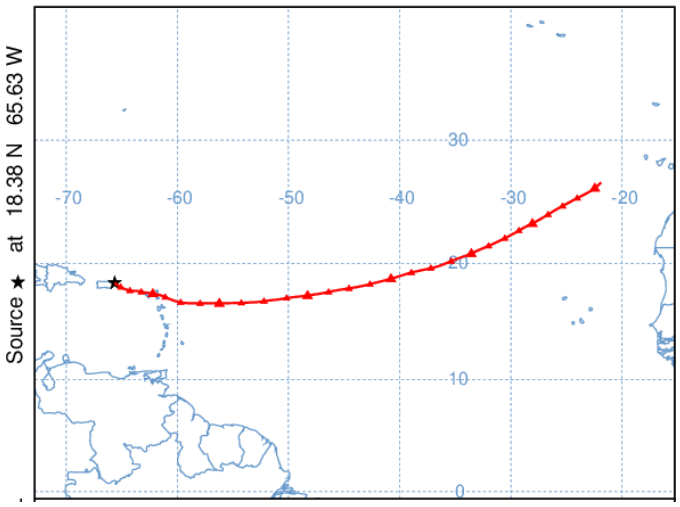

Figure 3.32 HYSPLIT 7-day backward trajectory of air mass arriving on July 15th, 2011, corresponding to Research Flight 06 (RF06).

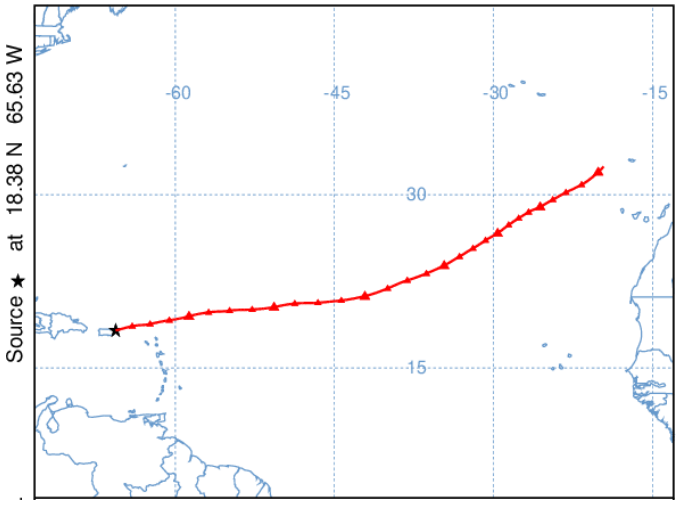

Figure 3.33 HYSPLIT 7-day backward trajectory of air mass arriving on July 30th, 2011, corresponding to Research Flight 13 (RF13).

The size distributions retrieved from the APSPD and HDDMA (Figure 3.34) show an increased number of accumulation and coarse mode particles during RF03, RF06, and RF12. That was not the case during RFs without dust.

An increased number of accumulation and coarse mode particles (> 0.1 µm) during ADD concurs with findings from Weinzierl et al. (2017) during SALTRACE 2013. Weinzierl et al. (2017) reported a shift to a smaller size spectrum across the eastern Caribbean compared to the west coast of Africa. This is associated with the loss of larger particles during the first 1-3 days and the aforementioned increase in particles under the accumulation mode due to coagulation processes.

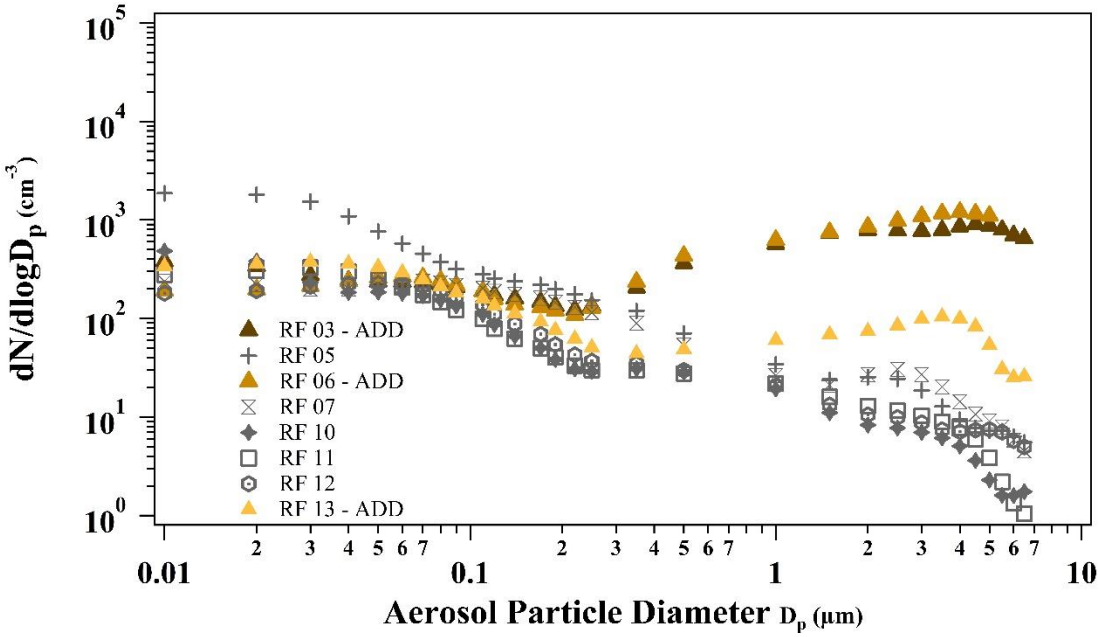

Figure 3.34 Aerosol particle size distribution retrieved from the Aerosol Particle Spectrometer with Polarization Detection (APSPD) and High-flow Dual-channel Differential Mobility Analyzer (HDDMA) during Ice in Clouds - Tropical (ICE-T) experiment.

In terms of the vertical profile, there is a higher concentration of aerosol particles above 3 km during ADD (RF03, RF06, and RF13) (Figure 3.35), with the highest concentration observed during RF03.

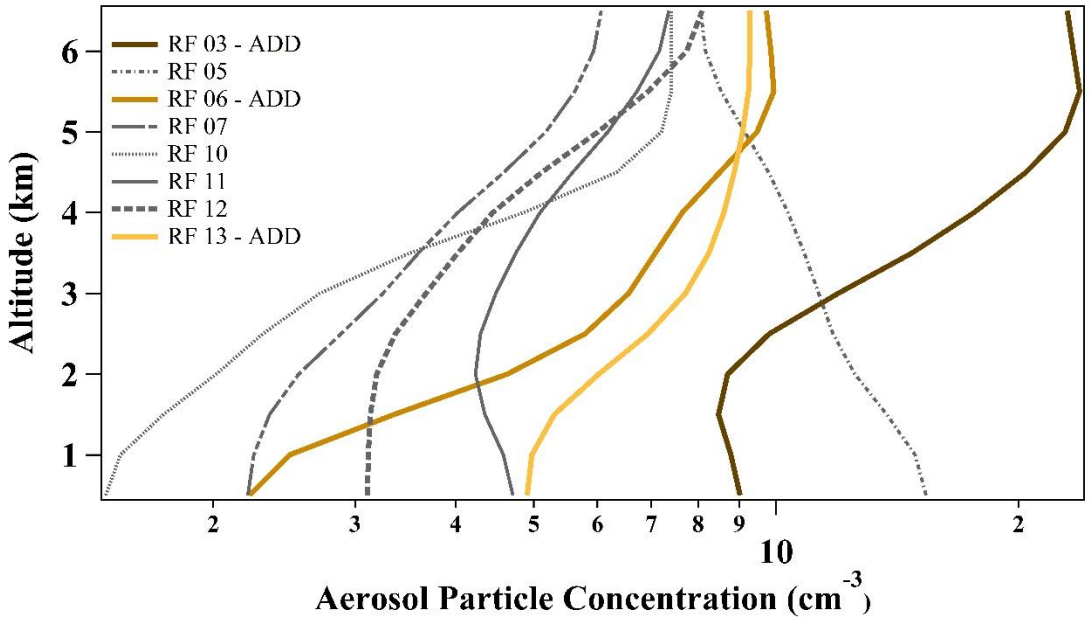

Figure 3.35 Vertical profile of aerosol particle number concentration retrieved from the Aerosol Particle Spectrometer with Polarization Detection (APSPD) during Ice in Clouds - Tropical (ICE-T).

Surprisingly, there is an increase in aerosol particle concentrations at lower levels during RF05 (Figure 3.35). Most likely due to anthropogenic aerosols as it is shown in Figure 3.34, where a higher number of particles is observed in the nucleation mode.

3.6 Nuclei Activation

An increased CCN concentration is observed during RF06 (Figure 3.36). Since the ability to serve as cloud condensation nuclei will depend on size, chemical composition, and local saturation (Choobari et al., 2014), the higher CCN concentration observed during RF06 is likely to be associated with the enhancement of dust hygroscopicity or a stronger updraft. As it is shown in Figure 3.34, there are no differences in terms of the sizes (RF03 vs. RF06), and the CCN counter configuration in terms of saturation remained unchanged throughout research flights.

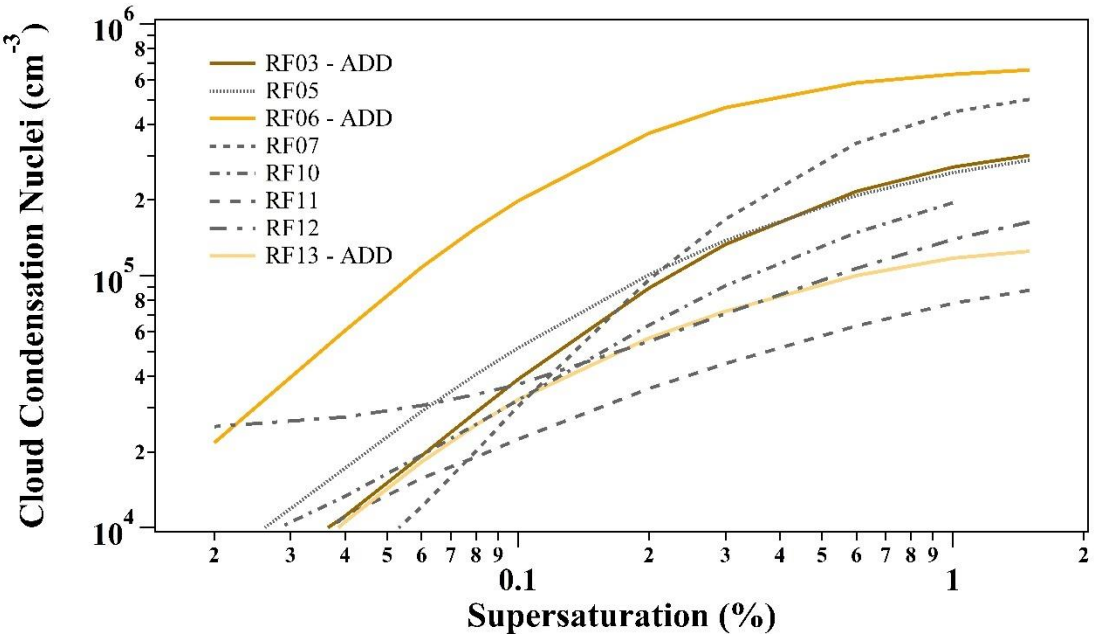

Figure 3.36 Cloud Condensation Nuclei (CCN) activation retrieved from the Cloud Condensation Nuclei Counter (CCN counter) during Ice in Clouds - Tropical (ICE-T).

In terms of IN activation and concentration, aerosol particles across the local area are efficient ice nuclei (activate) at temperatures near or below - 18˚C regardless of the presence of mineral dust or saturation (Figure 3.37).

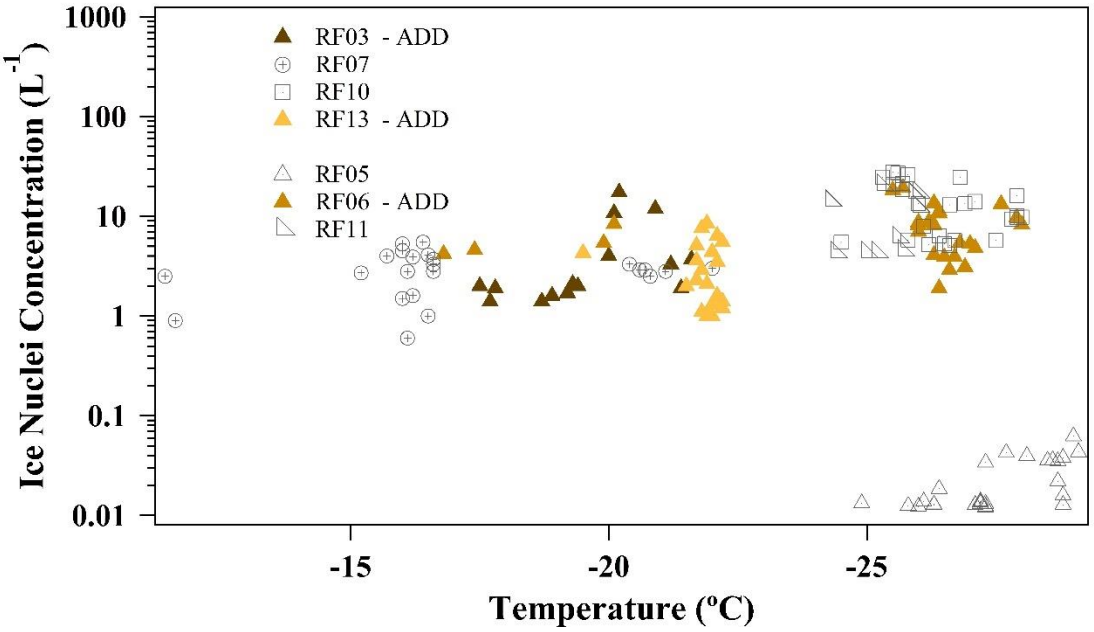

Figure 3.37 Ice nuclei concentration retrieved from the Continuous-Flow thermal gradient Diffusion Chamber (CFDC) during Ice in Clouds - Tropical (ICE-T).

3.7 Cloud Droplet Concentration

Data retrieved from the FSSP on board the C-130 do not show an increased number of smaller cloud droplet sizes on any of the flights (Figure 3.38). Therefore, based on the current information, dust across the area does not necessarily mean an increased number of smaller cloud droplet sizes.

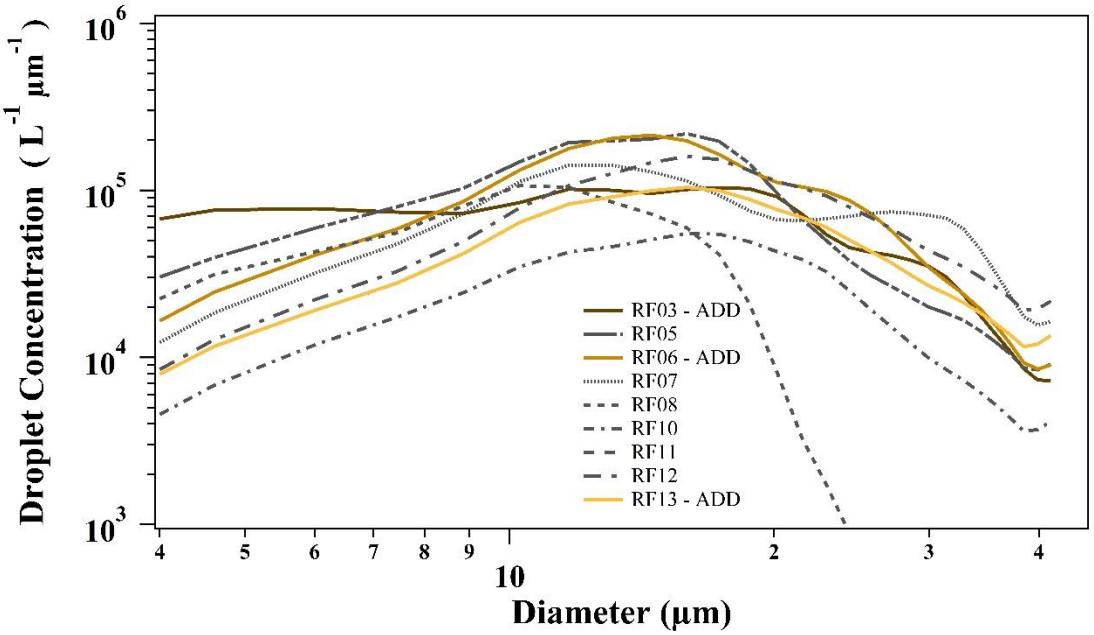

Figure 3.38 Droplet concentration retrieved from the Forward Scattering Spectrometer Probe (FSSP) during Ice in Clouds - Tropical (ICE-T).

3.8 Observed Rainfall Patterns

Based on the frequency of ADD during JJA and the 3-month SPI ending in August, there is a weak negative correlation (r = -0.20) between ADD and the rainfall observed at the San Juan International Airport (Figure 3.39). A weak correlation is observed as well at all weather stations with r values ranging between - 0.05 and - 0.44 (See Appendix D: Rainfall and the Standardized Precipitation Index). These results are statistically non-significant with p-values greater than 0.05.

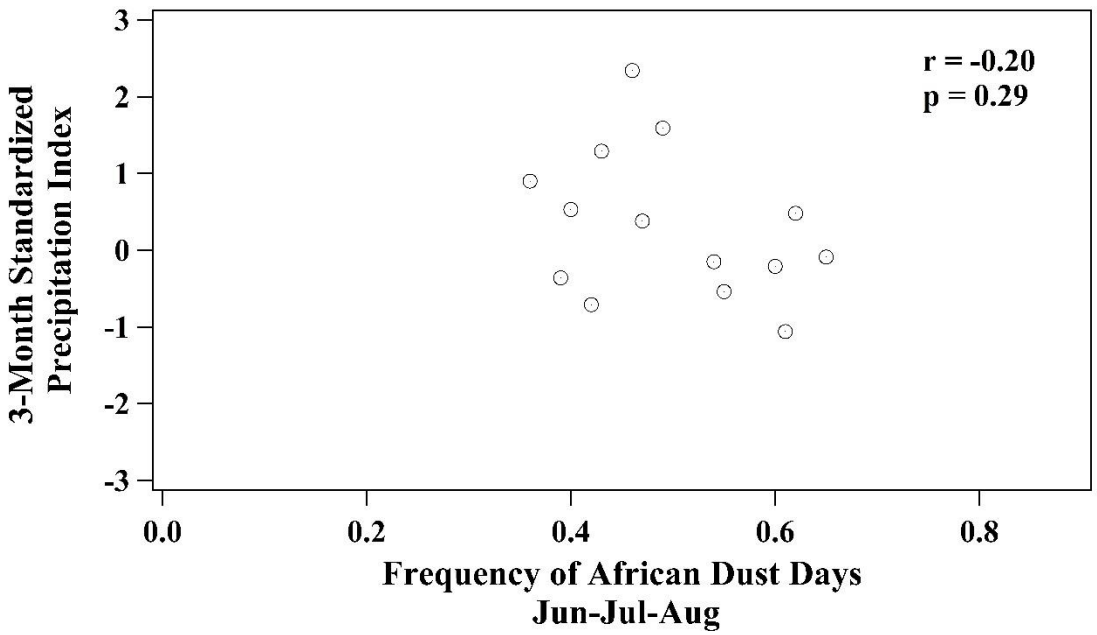

Figure 3.39 Correlation between frequency of African Dust Days (ADD) during Jun-Jul-Aug (JJA) and its corresponding 3-month standardized precipitation index (SPI) ending in August at Luis Muñoz Marin Airport.

The correlation between the magnitude of ADD during JJA and the 3-month SPI ending in August is highly variable within weather stations, meaning positive and negative r values (See Appendix D: Rainfall and the Standardized Precipitation Index). All of them are statistically non-significant as well.

Figure 3.40 shows the correlation between magnitude and rainfall at the San Juan International Airport.

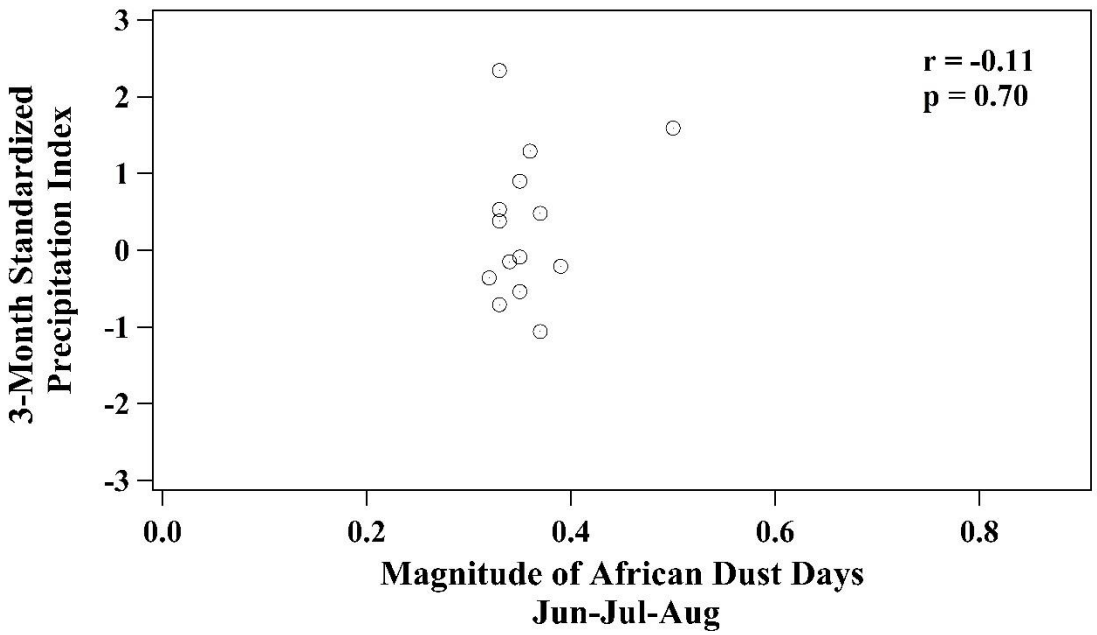

Figure 3.40 Correlation between magnitude of African Dust Days (ADD) during June-July and August (JJA) and its corresponding 3-month standardized precipitation index (SPI) ending in August at Luis Muñoz Marin Airport.

The weak correlation between frequency and magnitude of ADD and the seasonal rainfall can be attributed to the changes in the structure and vertical distribution of the dust layer during transit (Weinzierl et al., 2017).

Although dust can activate as CCN after aging, rainfall activity will depend on microphysical properties – which are highly variable between events as it is shown in section 3.5 to 3.7 – as well as the structure and vertical distribution of the dust layer and its thermodynamic characteristics.

3.9 Vertical Profile of Atmospheric Thermodynamics

There are 172 ADD -D and 502 ADD -W. The dust layer generally extends from 800 mb to 650 mb during ADD -D while it is observed between 700 mb and 600 mb during ADD-W.

Based on the meteorological soundings, there are no variations in $\boldsymbol{\theta}$ between ADD -D, ADD -W, or the 1995 – 2002 SAL climatology established by Dunion (2011) (Figure 3.41) (See Appendix A: Saharan Dust Layer (SAL) 1995 - 2002 climatology and other air masses).

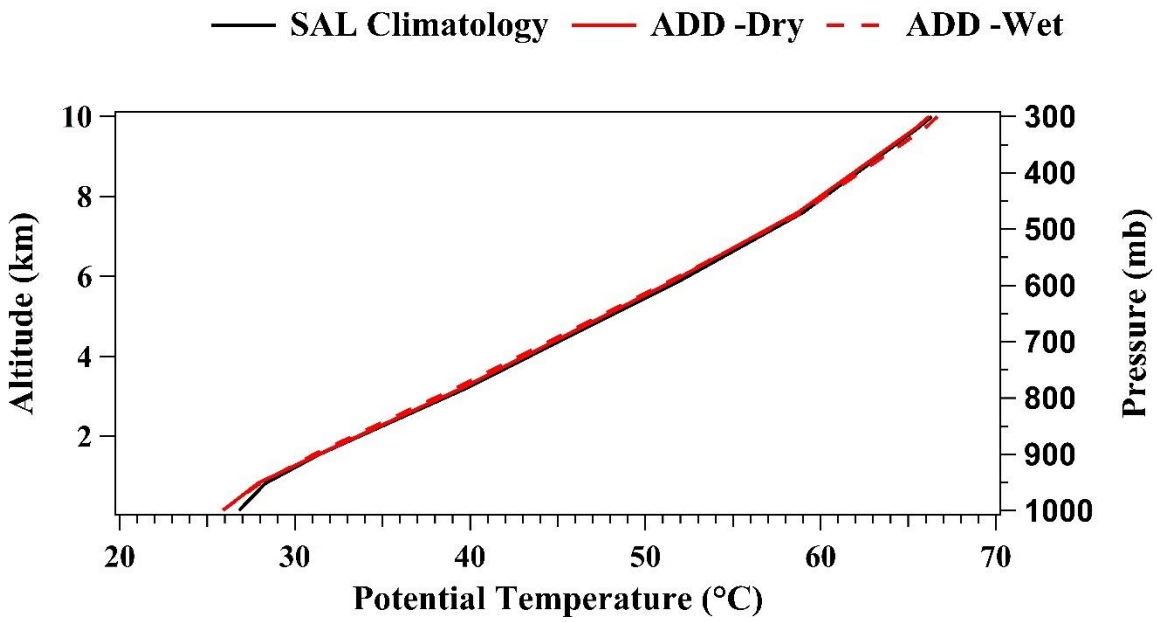

Figure 3.41 Vertical profile of potential temperature ($\boldsymbol{\theta}$) during African Dust Days (ADD). Comparison between the Saharan Air Layer (SAL) 1995 – 2002 climatology and days classified as ADD -D (Dry) and ADD -W (Wet).

There are, however, variations in the vertical profile of the mixing ratio ***(w)***, particularly in the convective boundary layer (CBL,~850 mb) with mean values of 9.0

and 11.6 g kg^{-1} during ADD -D and ADD -W, respectively (Figure 3.42). The 1995 - 2002 SAL climatology indicates a mean value of 10.28 g kg^{-1}.

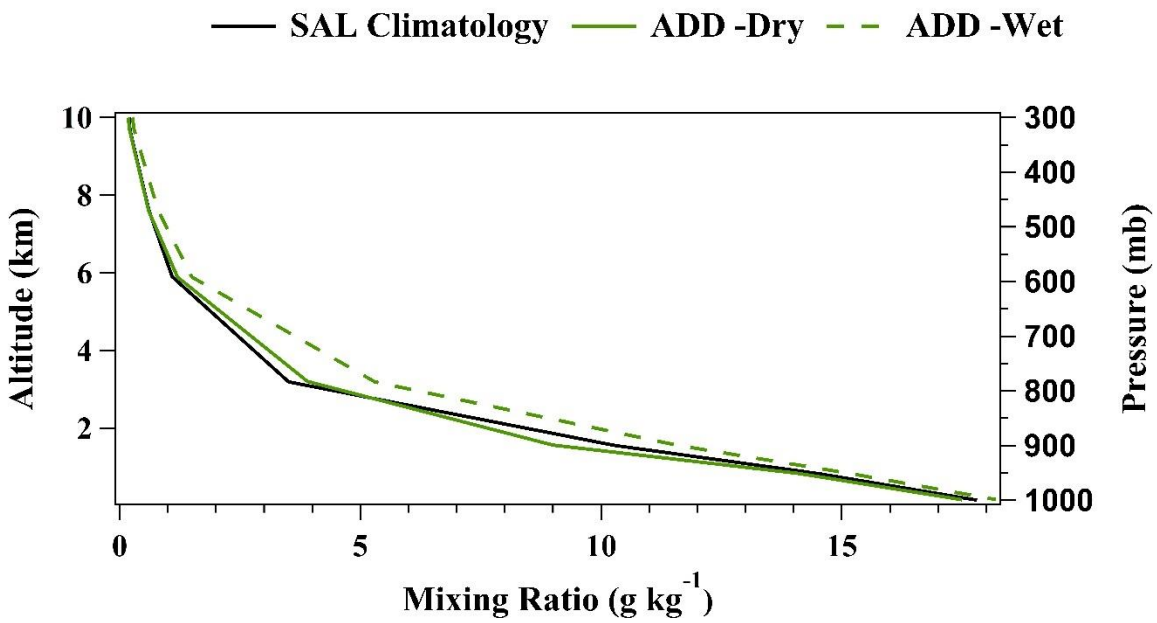

Figure 3.42 Vertical profile of mixing ratio (***w***) during African Dust Days (ADD). Comparison between the Saharan Air Layer (SAL) 1995 - 2002 climatology and days classified as ADD -D (Dry) and ADD -W (Wet).

The values of ***w*** in the CBL indicates that the mixing occurring between the surface to 950 mb and the dust layer through turbulence processes (Reid et al., 2003). Based on the analyzed data, additional mixing is observed between the surface and the dust layer during the ADD -W. This resulted in a greater variation in the relative humidity (RH) at 850 mb, which has a climatological value of 69.5%. The mean RH values are 59.6, and 78.5% during ADD -D and ADD -W, respectively (Figure 3.43).

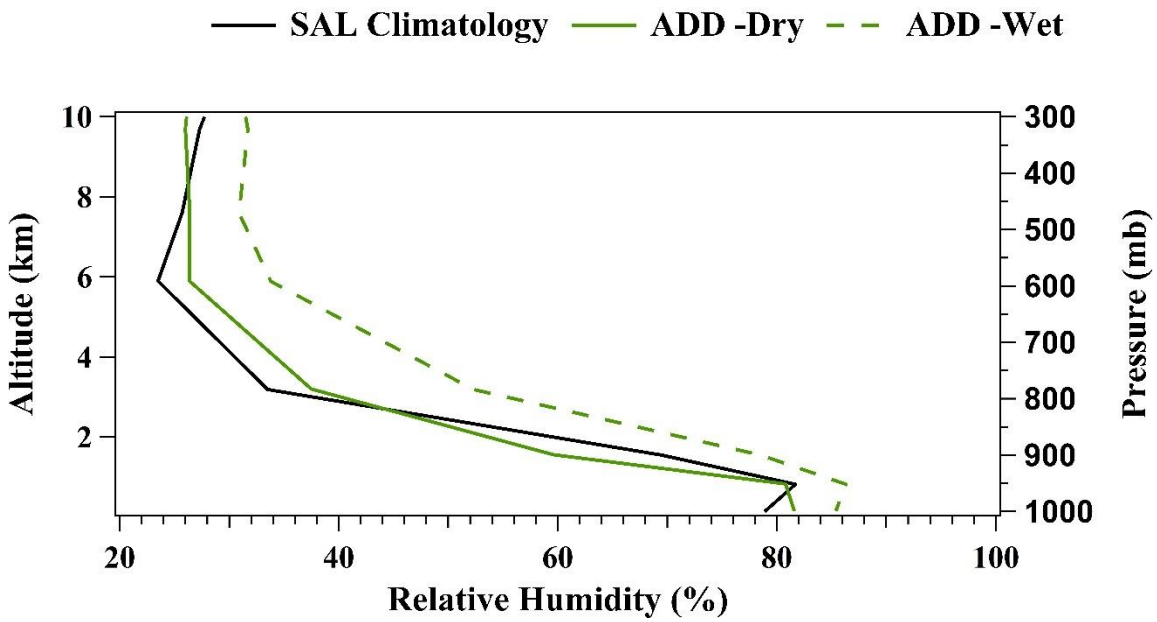

Figure 3.43 Vertical profile of relative humidity (RH) during African Dust Days (ADD). Comparison between the Saharan Air Layer (SAL) 1995 - 2002 climatology and days classified as ADD -D (Dry) and ADD -W (Wet).

There are also variations in the E_s profile. Based on the analyzed data, the mean E_s values are 328.7 and 334.1 kJ kg^{-1} during ADD -D and ADD -W, respectively (Figure 3.44). This concurs and improves the E_s values provided by Aspliden (1972) and Petit et al. (2005), which suggested that a very dry, stable, and dusty air mass has E_s below 330 kJ kg^{-1}. Based on these results, a slight adjustment in the threshold values could be introduced. A very dry, stable, and dusty air mass has E_s lower than 334 kJ kg^{-1}.

As a result, the thermodynamic characteristics at 850 mb, which are conductive for rainfall activity during dust outbreaks, correspond to mixing ratio near or above 12 g kg^{-1} combined with E_s values near or above than 334 kJ kg^{-1}.

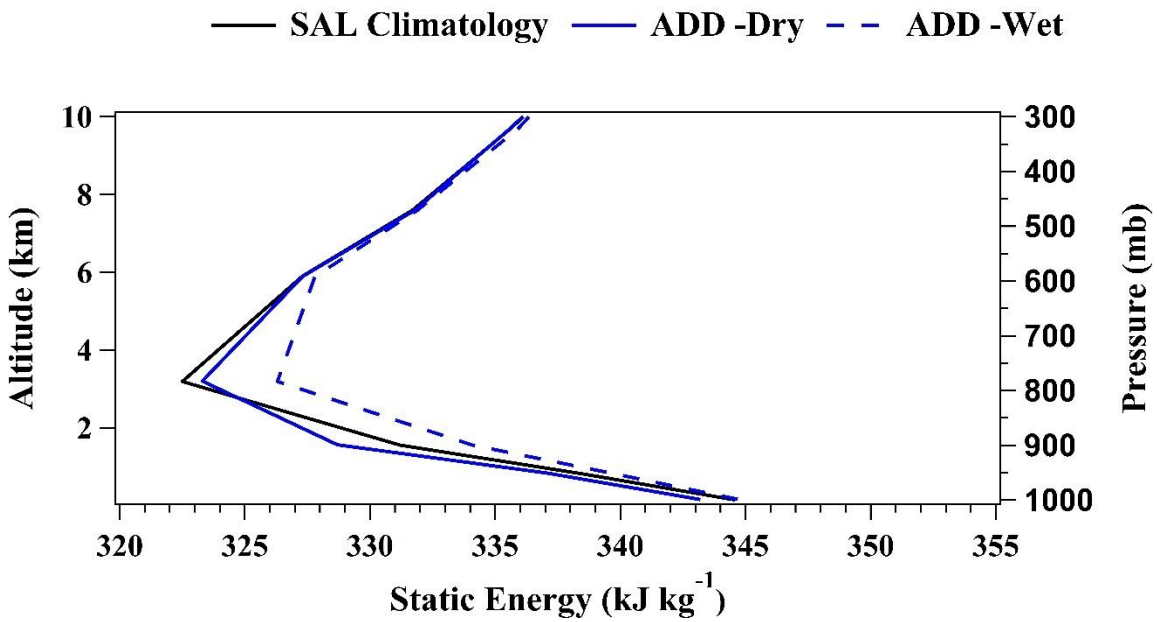

Figure 3.44 Vertical profile of the static energy (E_s) during African Dust Days (ADD). Comparison between the Saharan Air Layer (SAL) 1995 - 2002 climatology and days classified as ADD -D (Dry) and ADD -W (Wet).

There is no surprise to observe E_s values of 333.3, 333.4, and 339.0 kJ kg^{-1} and mixing ratios of 12, 12, and 14 g kg^{-1} at 850 mb during the RF03, RF06 and RF13, respectively. This is because rainfall activity was observed over Puerto Rico during those days (Figure 3.45 to 3.47).

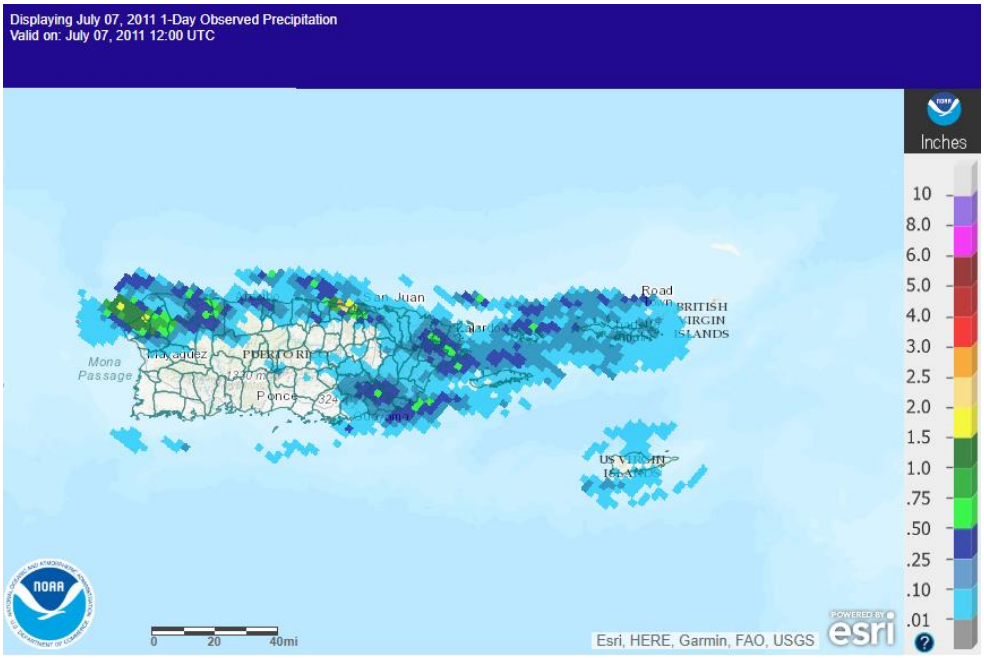

Figure 3.45 Rainfall totals retrieved from Advanced Hydrologic Prediction Service (AHPS) between July 6th, 2011, 8 AM AST, and July 7th, 2011, 8 AM AST, which corresponds to Research Flight 03 (RF03).

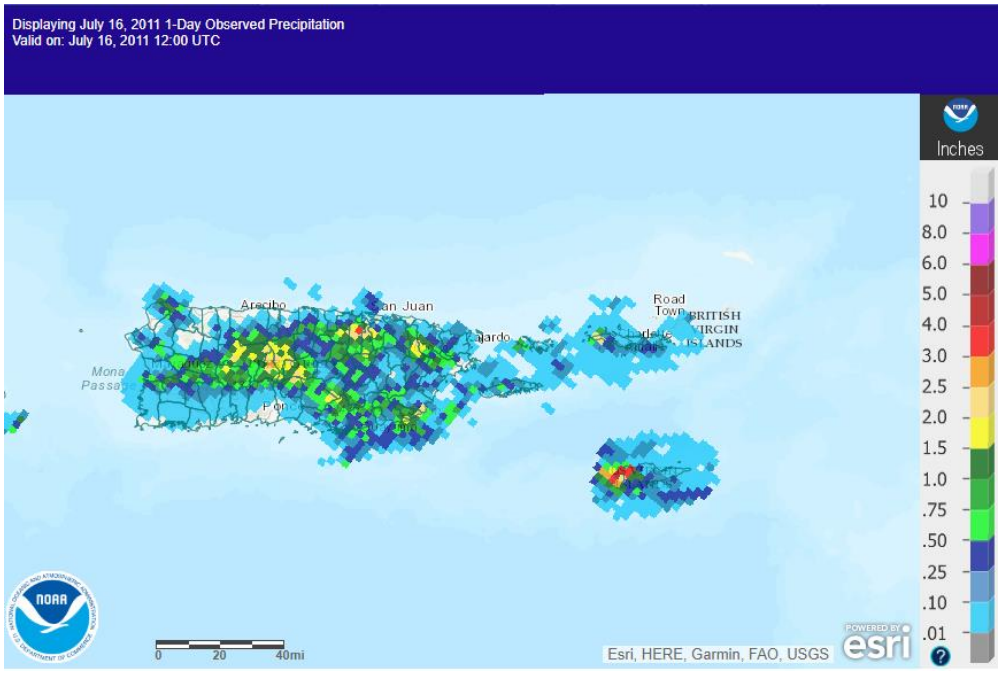

Figure 3.46 Rainfall total retrieved from Advanced Hydrologic Prediction Service (AHPS) between July 15th, 2011, 8 AM AST, and July 16th, 2011, 8 AM AST, which corresponds to Research Flight 06 (RF06).

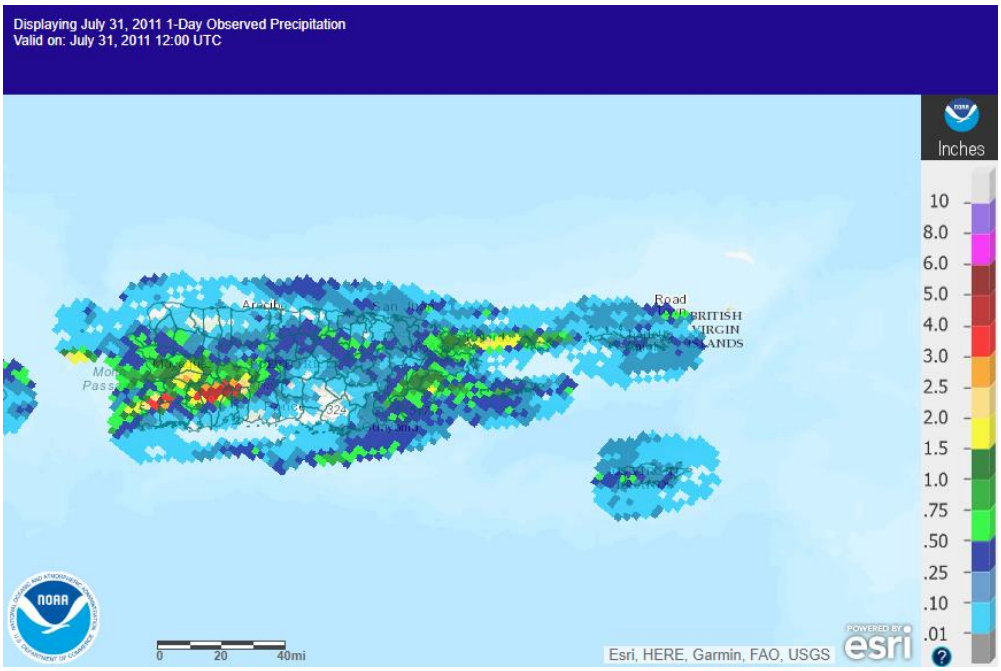

Figure 3.47 Rainfall accumulation retrieved from Advanced Hydrologic Prediction Service (AHPS) between July 30th, 2011, 8 AM AST, and July 31st, 2011, 8 AM AST, which correspond to Research Flight 13 (RF13).

Although similar values of $\boldsymbol{w}$ and $\boldsymbol{E_s}$ prevailed during RF03 and RF06, the difference (rainfall totals and coverage) (Figure 3.45 to 3.46) could be attributed to the stronger winds observed during RF03. The higher rainfall amount, as well as the areal coverage observed during RF13 (Figure 3.47), were associated with the higher values of $\boldsymbol{E_s}$ and $\boldsymbol{w}$.

Rainfall activity during dust outbreaks is observed if there are mixing ratios near or above 12 g kg^{-1} combined with $\boldsymbol{E_s}$ values are near or above 334 kJ kg^{-1} (850 mb). Additional data or computer modeling in terms of cloud droplet sizes are needed to answer scientific question #3. Therefore, further studies are needed to reject or accept hypothesis #2.

Chapter 4 CONCLUSIONS AND FUTURE WORK

The threshold values given by Velasco-Marino et al. (2018), Guirado et al. (2014) and Dubovik et al. (2002) to identify ADD (AOD ≥ 0.20 and $\boldsymbol{å} \leq 0.6$) are close to the 75th percentile (D75) within the LN distribution (best-fit) of the AOD and $\boldsymbol{å}$ population retrieved from the AERONET network in Puerto Rico. An AOD value equal or greater than 0.20 to identify dust days concurs with findings from SALTRACE 2013 and PRIDE 2002 as well. Therefore, there is high confidence to use AOD ≥ 0.20 as a threshold value. Nevertheless, it is highly recommended to combine it with $\boldsymbol{å}$ values close to zero because it confirms the presence of coarse mode particles (Eck et al., 1999).

There are no quantifiable trends in the frequency or magnitude of ADD during June, July, or August across the Puerto Rico area between 2004 and 2018. There are 674 days identified as ADD, with 505 of them observed during JJA (75%). There is a monthly average of 12 ± 6, 13 ± 4, and 8 ± 4 per June, July, and August, respectively. Data suggest that an increase in the frequency of ADD during any given month does not necessarily mean an increase in magnitude or vice versa.

Although the highest frequency of ADD is observed during the summer months, from time to time ADD could also be observed during winter, spring, or fall depending on the synoptic patterns. This is because African dust is transported across the tropical North Atlantic in great quantities almost all year; however, dust sources and transport path change (Prospero et al., 2014).

The most striking finding is that the intra-seasonal variations of dust transport into the northeast Caribbean are modulated by the NAFDI phases. The enhanced dust transport into the northeast Caribbean is determined by the synoptic pattern associated with the NAFDI phase. The synoptic pattern that enhances dust transport towards the tropical Atlantic and into the northeast Caribbean from the Sahel/Sub Sahara region - which is the primary dust source early in the summer- corresponds to a stronger pressure gradient west of Western Africa combined with a much more elongated Azores High (NAFDI negative phase). This flattens the western side of the North African anticyclone, which strengths easterly wind at 700 mb near the Sahel/Sub Sahara region.

As the ITCZ moves northward, the synoptic pattern that enhances dust transport from the Sahara toward the Subtropical Atlantic and into the northeast Caribbean is the merging of the Azores High with the North African anticyclone (NAFDI positive phase). This results in stronger easterly winds at 700 mb between 15˚ and 20˚N, where the primary dust sources are then observed (Sahara region).

After long-range transport, the vertical extent of the dust layer over Puerto Rico is located from 800 mb to 650 mb during ADD-D and between 700 mb and 600 mb during ADD-W. There is no surprise to observe an increased number of accumulation (diameter > 0.1 μm) and coarse mode particles (diameter > 1 μm) during dust outbreaks across the local area. Findings from Weinzierl et al. (2017) suggest a shift to a smaller size spectrum across the eastern Caribbean compared to the west coast of Africa. This shift is associated with the loss of larger particles during the first 1-3 days and the increase in aerosol particles under the accumulation mode.

It was found a weak correlation between the frequency and magnitude of ADD during JJA and the seasonal rainfall. This is attributed to the changes in the structure and vertical distribution of the dust layer during transit (Weinzierl et al., 2017). Data suggest, however, that rainfall activity will be determined by specific thermodynamics characteristics. ***Measurable rainfall (> 0.01 inches) is observed during ADD with mixing ratios near or above 12 g kg^{-1} combined with E_s values near or above 334 kJ kg^{-1} at 850 mb.***

Additional measurements of cloud droplet sizes across the Caribbean are still needed with future research work focusing on dust and rainfall, and possibly lightning activity. An extensive cloud droplet size database will help to confirm if smaller cloud droplet sizes tend to reduce precipitation efficiency. The greatest uncertainty in assessments of climate change arises from aerosol-cloud-climate interactions (Forster et al., 2007). Therefore, a better understanding of cloud droplet sizes is imperative.

Chapter 5 BIBLIOGRAPHY

Ångström, A. (1929). On the Atmospheric Transmission of Sun Radiation and on Dust in the Air. *Geografiska Annaler, 11*, 156-166.

Andreae, M. O., Rosenfeld, D., Artaxo, P., Costa, A. A., Frank, G. P., Longo, K. M., & Silva-Dias, M. A. F. (2004). Smoking rain clouds over the Amazon. *Science, 303*, 1337–1342.

Aspliden, C. (1972). Analyses de structures énergétiques lors de BOMEX. *Barbados Oceanographic and Meteorological Experiment*, Tallahassee, FL: NOAA.

Baumgardner, D., Dye, J. E., Knollenberg, R. G., & Gandrud, B. W. (1992). Interpretation of measurements made by the FSSP-300X during the Airborne Arctic Stratospheric Expedition. *Journal of Geophysical Research, 97*, 8035 – 8046.

Bellouin, N., Rae, J., Jones, A., Johnson, C., Haywood, J., & Boucher, O. (2011). Aerosol forcing in the Climate Model Intercomparison Project (CMIP5) simulations by HadGEM2-ES and the role of ammonium nitrate. *Journal of Geophysical Research Atmospheres, 116*(20), 1–25.

Carlson, T. N. (2016). The Saharan elevated mixed layer and its aerosol optical depth. *The Open Atmospheric Science Journal, 10*, 26–38.

Carlson, T. N., & Prospero, J. M. (1972). The large-scale movement of Saharan Air outbreaks over the northern Atlantic. *Journal of Applied Meteorology, 11*, 283–297.

Cheng, W. Y. Y., Carrió, G. G., Cotton, W. R., & Saleeby, S. M. (2009). Influence of cloud condensation and giant cloud condensation nuclei on the development of precipitating trade wind cumuli in a large eddy simulation. *Journal of Geophysical Research*, *114*(D8), D08201.

Choobari, O. A., Zawar-Reza, P., & Sturman, A. (2014). The global distribution of mineral dust and its impacts on the climate system: A review. *Atmospheric Research*, *138*, 152–165.

Cuevas, E., Gómez-Peláez, A. J., Rodríguez, S., Terradellas, E., Basart, S., García, R. D., … Alonso-Pérez, S. (2017). The pulsating nature of large-scale Saharan dust transport as a result of interplays between mid-latitude Rossby waves and the North African Dipole Intensity. *Atmospheric Environment*, *167*, 586–602.

d'Almeida, G. A. (1986). A model for Saharan dust transport. *Journal of Climate and Applied Meteorology*, *25*(7), 903–916.

Denjean, C., Formenti, P., Desboeufs, K., Chevaillier, S., Triquet, S., Maille, M., … Ogren, J. (2016). Size distribution and optical properties of African mineral dust after intercontinental transport. *Journal of Geophysical Research Atmospheres*, 121, 7117–7138.

Denjean, C., Caquineau, S., Desboeufs, K., Laurent, B., Maille, M., Quiñones Rosado, M., … Formenti, P. (2015). Long-range transport across the Atlantic in summertime does not enhance the hygroscopicity of African mineral dust. *Geophysical Research Letters*, 42, 7835-7843.

Dubovik, O., Holben, B., Eck, T. F., Smirnov, A., Kaufman, Y. J., King, M. D., … Slutsker, I. (2002). Variability of absorption and optical properties of key aerosol types observed in worldwide locations. *Journal of the Atmospheric Sciences*, *59*(3), 590–608.

Dunion, J. P. (2011). Rewriting the climatology of the tropical North atlantic and Caribbean Sea atmosphere. *Journal of Climate*, *24*(3), 893–908.

Eck, T. F., Holben, B. N., Reid, J.S., Dubovik, O., Smirnov, A., O'Neill, N.T., … Kinne, S. (1999). Wavelength dependence of the optical depth of biomass burning, urban, and desert dust aerosols. *Journal of Geophysical Research, 104*(D24), 31333–31349.

Edwards, D.C., & McKee, T.B. (1997). Characteristics of 20th century drought in the United States at multiple times scales. *Atmospheric Science Paper, 634*, 1-30.

Evan, A. T., Flamant, C., Gaetani, M., & Guichard, F. (2016). The past, present and future of African dust. *Nature*, *531*(7595), 493–495. https://doi.org/10.1038/nature17149

Evan, A. T., Dunion, J., Foley, J. A., Heidinger, A. K., & Velden, C. S. (2006). New evidence for a relationship between Atlantic tropical cyclone activity and African dust outbreaks. *Geophysical Research Letters*, *33*(19), 1–5.

Engelstaedter, S., & Washington, R. (2007). Temporal controls on global dust emissions: The role of surface gustiness. *Geophysical Research Letters*, *34*(15), 1–5.

Fiedler, S., Schepanski, K., Heinold, B., Knippertz, P., & Tegen, I. (2013). Climatology of nocturnal low-level jets over North Africa and implications for modeling mineral dust emission. *Journal of Geophysical Research Atmospheres*, *118*(12), 6100–6121.

Formenti, P., Caquineau, S., Desboeufs, K., Klaver, A., Chevaillier, S., Journet, E., & Rajot, J. L. (2014). Mapping the physico-chemical properties of mineral dust in western Africa: Mineralogical composition. *Atmospheric Chemistry and Physics*, *14*(19), 10663–10686.

Forster, P., Ramaswamy, V., Artaxo, P., Berntsen, T., Betts, R., Fahey, D. W., … Dorland, R. V. (2007). Changes in atmospheric constituents and in radiative forcing. *In Climate Change 2007: The Physical Science Basis*. Contribution of Working Group I to the Fourth Assessment Report of the Intergovernmental Panel on Climate Change. Cambridge University Press: USA.

Gillette, D.A. (1979). On the production of soil wind erosion having the potential for long range transport. *Journal of Geophysical Research, 8*, 734–744.

Ginoux, P., Prospero, J., Torres, O., & Chin, M. (2004). Long-term simulation of global dust distribution with the GOCART model: correlation with North Atlantic Oscillation. *Environmental Modelling & Software*, *19*(2), 113–128.

Gioda, A., Reyes-Rodríguez, G. J., Santos-Figueroa, G., Collett, J. L., Decesari, S., Ramos, M. da C. K. V., … Mayol-Bracero, O. L. (2011). Speciation of water-soluble inorganic, organic, and total nitrogen in a background marine environment: Cloud water, rainwater, and aerosol particles. *Journal of Geophysical Research*, *116*(D5), D05203.

Groß, S., Gasteiger, J., Freudenthaler, V., Müller, T., Sauer, D., Toledano, C., & Ansmann, A. (2016). Saharan dust contribution to the Caribbean summertime boundary layer – a lidar study during SALTRACE. *Atmospheric Chemistry and Physics*, *16*(18), 11535–11546.

Guirado, C., Cuevas, E., Cachorro, V. E., Toledano, C., Alonso-Pérez, S., Bustos, J. J., … De Frutos, A. M. (2014). Aerosol characterization at the Saharan AERONET site Tamanrasset. *Atmospheric Chemistry and Physics*, *14*(21), 11753–11773.

Heymsfield, A. J., Bansemer, A., Heymsfield, G., & Fierro, A. O. (2009). Microphysics of Maritime Tropical Convective Updrafts at Temperatures from −20° to −60°. *Journal of the Atmospheric Sciences*, *66*(12), 3530–3562.

Hinds, W.C. (1999). *Aerosol Technology: Properties, Behavior, and Measurements of Airborne Particles*. USA: John Wiley and Sons.

Holben, B. N., Eck, T. E., Slutsker, I., Tanre, D., Buis, J. P., Setzer, A., & Smirnov, A. (1998). AERONET—a federated instrument network and data archive for aerosol characterization. *Remote Sensing Environment*, *66*, 1–16.

Holmgren, H. (2011). *On the formation and physical behavior of exhaled particles*. Retrieved from Semantic Scholar.

Huang, J., Zhang, C., & Prospero, J. M. (2010). African dust outbreaks : A satellite perspective of temporal and spatial variability over the tropical Atlantic Ocean. *Journal of Geophysical Research*, *115*, 1–20.

Huneeus, N., Schulz, M., Balkanski, Y., Griesfeller, J., Prospero, J., Kinne, S., … Zender, C. S. (2011). Global dust model intercomparison in AeroCom phase I. *Atmospheric Chemistry and Physics*, *11*(15), 7781–7816.

Huneeus, N., Boucher, O., & Chevallier, F. (2013). Atmospheric inversion of SO2 and primary aerosol emissions for the year 2010. *Atmospheric Chemistry and Physics*, *13*(13), 6555–6573.

Jenkins, G. S., & Pratt, A. (2008). Saharan dust , lightning and tropical cyclones in the eastern tropical Atlantic during NAMMA-06. *Geophysical Research Letters*, *35*, L12804.

Kalu, A. E. (1979). The African dust plume: Its characteristics and propagation across west Africa in Winter. *Scope*, *14*, 95–118.

Kalnay, E., Kanamitsu, M., Kistler, R., Collins, W., Deaven, D. Gandin, L., …Joseph, D. (1996). The NCEP/NCAR 40-year reanalysis project. *Bulletin of the American Meteorological Society*, 77, 437–471.

Keyantash, J., & National Center for Atmospheric Research Staff (Eds). Last modified 07 Aug 2018. "*The Climate Data Guide: Standardized Precipitation Index (SPI).*" Retrieved from https://climatedataguide.ucar.edu/climate-data/standardized-precipitation-index-spi.

Khain, A. P., BenMoshe, N., & Pokrovsky, A. (2008). Factors determining the impact of aerosols on surface precipitation from clouds: An attempt at classification. *Journal of the Atmospheric Sciences*, *65*(6), 1721–1748.

Kirkby, J. (2001). Beam measurements of a CLOUD (Cosmics Leaving OUtdoor Droplets) chamber, CERN-OPEN-2001-028, 27 pp., European Organization for Nuclear Research (CERN), Geneva, Switzerland.

Knippertz, P., & Stuut, JB. W. (2014). *Mineral Dust: A Key Player in Earth System*. USA: Springer.

Koehler, K. A., Kreidenweis, S. M., DeMott, P. J., Prenni, A. J., & Petters, M. D. (2007). Potential impact of Owens (dry) Lake dust on warm and cold cloud formation. *Journal of Geophysical Research*, *112*(D12), D12210.

Lagzi, I., Meszaros, R., Gelybo, G., & Leelossy, A. (2013). *Atmospheric Chemistry*. Hungary: Eotvos Lorand University.

Lavaysse, C., Flamant, C., & Janicot, S. (2010). Regional-scale convection patterns during strong and weak phases of the Saharan heat low. *Atmospheric Science Letters*, *11*(4), 255–264.

Lavaysse, C., Flamant, C., Janicot, S., Parker, D. J., Lafore, J. P., Sultan, B., & Pelon, J. (2009). Seasonal evolution of the West African heat low: A climatological perspective. *Climate Dynamics*, *33*(2–3), 313–330.

Lin, W., & Qing-Cun, Z. (2011). Study on probability distributions of multi-timescale aerosol optical depth using AERONET Data. *Atmospheric and Oceanic Science Letters*, *4*(4), 216–222.

Marticorena, B., & Formenti, P. (2013). Fundamentals of Aeolian Sediment Transport: Long-Range Transport of Dust. In *Treatise on Geomorphology*, *11*, 64-84.

Martinez, C., Goddard, L., Kushnir, Y., & Ting, M. (2019). Seasonal climatology and dynamical mechanisms of rainfall in the Caribbean. *Climate Dynamics*, *53*(1–2), 825–846.

Moreno, T., Querol, X., Castillo, S., Alastuey, A., Cuevas, E., Herrmann, L., … Gibbons, W. (2006). Geochemical variations in aeolian mineral particles from the Sahara-Sahel Dust Corridor. *Chemosphere*, *65*(2), 261–270.

Myhre, G., Shindell, D., Bréon, F.M., Collins, W., Fuglestvedt, J., Huang, J., … Zhang, H. (2013). Anthropogenic and Natural Radiative Forcing. In: *Climate Change 2013: The Physical Science Basis.* Contribution of Working Group I to the Fifth

Assessment Report of the Intergovernmental Panel on Climate Change. Cambridge University Press: USA.

Petit, R. H., Legrand, M., Jankowiak, I., Molinié, J., Asselin de Beauville, C., Marion, G., & Mansot, J. L. (2005). Transport of Saharan dust over the Caribbean Islands: Study of an event. *Journal of Geophysical Research : Atmospheres*, *110*(18), 1–19.

Prospero, J. M. (2002). Environmental characterization of global sources of atmospheric soil dust identified with the NIMBUS 7 Total Ozone Mapping Spectrometer (TOMS) absorbing aerosol product. *Reviews of Geophysics*, *40*(1), 1002.

Prospero, J. M., & Lamb, P. (2003). African droughts and dust transport to the Caribbean: climate change implications. *Science*, *302*(5647), 1024–1027.

Prospero, J. M., Collard, F. X., Molinié, J., & Jeannot, A. (2014). Characterizing the annual cycle of African dust transport to the Caribbean Basin and South America and its impact on the environment and air quality. *Global Biogeochemical Cycles*, *29*, 757-773.

Raga, G. B., Baumgardner, D., & Mayol-Bracero, O. L. (2016). History of aerosol-cloud interactions derived from observations in mountaintop clouds in Puerto Rico. *Aerosol and Air Quality Research*, *16*(3), 674–688.

Ridley, D. A., C. L. Heald, C.L., & Prospero, J.M. (2014). What controls the recent changes in African mineral dust aerosol across the Atlantic? *Atmospheric Chemistry and Physics*, 14, 5735–5747.

Reid, J. S. (2003). Analysis of measurements of Saharan dust by airborne and ground-

based remote sensing methods during the Puerto Rico Dust Experiment (PRIDE). *Journal of Geophysical Research*, *108*(D19), 8586.

Rodríguez, S., Cuevas, E., Prospero, J. M., Alastuey, A., Querol, X., López-Solano, J., … Alonso-Pérez, S. (2015). Modulation of Saharan dust export by the North African dipole. *Atmospheric Chemistry and Physics*, *15*(13), 7471–7486.

Rogers, D. C., DeMott, P. J., Kreidenweis, S. M., & Chen, Y. (2001). A continuous-flow diffusion chamber for airborne measurements of ice nuclei. *Journal of Atmospheric and Oceanic Technology*, *18*(5), 725–741.

Sayer, A. M., Hsu, N. C., Bettenhausen, C., & Jeong, M. J. (2013). Validation and uncertainty estimates for MODIS Collection 6 "deep Blue" aerosol data. *Journal of Geophysical Research Atmospheres*, *118*(14), 7864–7872.

Scheuvens, D., Schütz, L., Kandler, K., Ebert, M., & Weinbruch, S. (2013). Bulk composition of northern African dust and its source sediments - A compilation. *Earth-Science Reviews*, *116*(1), 170–194.

Shao, Y., Wyrwoll, K. H., Chappell, A., Huang, J., Lin, Z., McTainsh, G. H., … Yoon, S. (2011). Dust cycle: An emerging core theme in Earth system science. *Aeolian Research*, *2*, 181-204.

Stein, A. F., Draxler, R. R., Rolph, G. D., Stunder, B. J. B., Cohen, M. D., & Ngan, F. (2015). Noaa's hysplit atmospheric transport and dispersion modeling system. *Bulletin of the American Meteorological Society*, *96*(12), 2059–2077. https://doi.org/10.1175/BAMS-D-14-00110.1

Twohy, C. H., Kreidenweis, S. M., Eidhammer, T., Browell, E.D., Heymsfield, A. J., Bansermer, A. R., … Van Den Heever, S. C. (2009). Saharan dust particles nucleate droplets in eastern Atlantic clouds. *Geophysical Research Letters*, *36*, L01807.

Twomey, S. (1977). The influence of pollution on the shortwave albedo of clouds. *Journal of the Atmospheric Sciences*, *34* (7), 1149–1154.

Valle-Díaz, C. J., Torres-Delgado, E., Colón-Santos, S. M., Lee, T., Collett, J. L. J., McDowell, W. H., & Mayol-Bracero, O. L. (2016). Impact of Long-Range Transported African Dust on Cloud Water Chemistry at a Tropical Montane Cloud Forest in Northeastern Puerto Rico. *Aerosol and Air Quality Research*, *16*(3), 653–664.

Velasco-Merino, C., Mateos, D., Toledano, C., Prospero, J. M., Molinie, J., Euphrasie-Clotilde, L., … De Frutos, A. M. (2018). Impact of long-range transport over the Atlantic Ocean on Saharan dust optical and microphysical properties based on AERONET data. *Atmospheric Chemistry and Physics*, *18*(13), 9411–9424.

Weinzierl, B., Ansmann, A., Prospero, J. M., Althausen, D., Benker, N., Chouza, F., … Walser, A. (2017). The Saharan aerosol long-range transport and aerosol-cloud-interaction experiment: Overview and selected highlights. *Bulletin of the American Meteorological Society*, *98*(7), 1427–1451.

Appendix A: Table A.1 Saharan Air Layer (SAL) 1995 - 2002 climatology and other air masses.

MT-moist tropical airmass, **MLDAI**-midlatitude dry air intrusion, **SAL**-Saharan Air Layer
Theta -Potential Temperature, **Theta-e -**Equivalent Potential Temperature

TABLE 2. MT (roman), SAL (boldface), and MLDAI (italics) July–October (1995–2002) mean atmospheric soundings.

Pressure (hPa)	GPH (m)	Temperature (°C)	Dewpoint (°C)	RH (%)	Mixing ratio (g kg^{-1})	Theta (K)	Theta-*e* (K)	Wind speed (m s^{-1})	Wind direction (°)
50	20 726	−63.0	−73.8	25.5	0.04	494.5	495.4	12.7	88
	20 733	**−63.0**	**−72.2**	**28.6**	**0.05**	**494.6**	**496.4**	**15.6**	**89**
	20 696	*−63.2*	*−75.4*	*21.5*	*0.04*	*494.1*	*495.1*	*9.5*	*88*
100	16 590	−74.5	−81.3	33.8	0.01	383.5	384.4	4.1	67
	16 593	**−73.7**	**−80.4**	**32.5**	**0.01**	**385.0**	**386.7**	**6.0**	**86**
	16 572	*−75.2*	*−83.1*	*29.2*	*0.004*	*382.2*	*382.8*	*1.8*	*356*
150	14 203	−67.2	−74.7	35.3	0.01	354.2	354.5	3.6	330
	14 196	**−66.8**	**−74.5**	**32.6**	**0.01**	**354.8**	**355.5**	**1.1**	**329**
	14 182	*−66.6*	*−75.6*	*29.0*	*0.01*	*355.2*	*355.6*	*6.6*	*292*
200	12 418	−54.3	−63.2	35.9	0.04	346.6	346.8	3.6	309
	12 413	**−54.7**	**−64.2**	**31.6**	**0.04**	**346.0**	**346.2**	**2.1**	**300**
	12 395	*−54.5*	*−65.3*	*28.2*	*0.03*	*346.3*	*346.5*	*7.5*	*293*
250	10 949	−42.3	−52.4	37.0	0.14	343.0	343.6	2.1	305
	10 947	**−43.1**	**−54.2**	**31.4**	**0.11**	**341.9**	**342.2**	**0.9**	**323**
	10 930	*−43.1*	*−55.9*	*27.6*	*0.09*	*341.9*	*342.3*	*6.2*	*292*
300	9690	−32.3	−43.5	38.7	0.34	339.8	341.1	0.9	309
	9693	**−33.1**	**−47.4**	**27.3**	**0.21**	**338.6**	**339.5**	**1.1**	**57**
	9676	*−33.3*	*−48.5*	*25.4*	*0.20*	*338.3*	*339.2*	*4.3*	*297*
400	7596	−17.1	−28.7	44.4	1.12	332.7	336.8	0.8	100
	7604	**−17.5**	**−35.1**	**25.7**	**0.61**	**332.1**	**334.4**	**3.5**	**83**
	7590	*−17.8*	*−37.2*	*22.2*	*0.52*	*331.8*	*333.8*	*1.6*	*342*
500	5887	−6.6	−16.9	51.8	2.41	325.0	333.3	1.8	111
	5897	**−6.4**	**−26.4**	**23.5**	**1.09**	**325.1**	**329.1**	**5.0**	**84**
	5883	*−6.3*	*−28.5*	*20.1*	*0.95*	*325.3*	*328.7*	*1.7*	*38*
600	4437	1.6	−7.1	57.7	4.11	317.9	331.4	2.7	113
	4451	**1.5**	**−16.5**	**30.7**	**2.13**	**317.8**	**325.0**	**6.7**	**88**
	4430	*2.2*	*−18.9*	*25.9*	*1.92*	*318.6*	*325.2*	*1.8*	*54*
700	3178	8.9	2.5	65.7	6.74	312.3	333.6	3.6	112
	3190	**9.4**	**−6.6**	**33.5**	**3.51**	**312.8**	**324.3**	**7.8**	**91**
	3173	*9.2*	*−9.5*	*30.7*	*3.17*	*312.7*	*323.0*	*3.1*	*69*
850	1541	17.6	13.8	79.5	11.96	304.6	340.5	4.7	109
	1553	**17.5**	**11.3**	**69.5**	**10.28**	**304.5**	**335.5**	**7.6**	**92**
	1542	*16.4*	*10.6*	*71.4*	*9.92*	303.3	333.1	*5.0*	*79*
925	810	21.9	19.0	84.2	15.27	301.7	346.9	4.9	108
	823	**21.6**	**18.2**	**81.7**	**14.53**	**301.4**	**344.3**	**7.1**	**92**
	815	*20.6*	*17.1*	*80.8*	*13.60*	*300.4*	*340.5*	*5.6*	*81*
1000	124	26.5	23.3	83.3	18.50	299.6	354.0	3.0	98
	138	**26.7**	**22.7**	**78.9**	**17.81**	**299.9**	**352.3**	**4.4**	**86**
	133	*25.8*	*21.1*	*76.2*	*16.28*	*298.9*	*346.6*	*3.5*	*74*
P_{MSL} = 1014.8	—	26.8	23.7	83.3	18.65	298.8	353.5	1.8	97
P_{MSL} = 1016.5	—	**27.6**	**23.2**	**77.2**	**18.04**	**299.5**	**352.5**	**2.7**	**84**
P_{MSL} = 1015.7	—	*26.2*	*21.8*	*77.6*	*16.65*	*298.1*	*346.7*	*2.0*	*74*
Layer mean (850–500)	—	6.7	−0.2	65.7	7.04	314.0	335.8	3.4	111
	—	**6.8**	**−7.2**	**42.2**	**4.97**	**314.1**	**329.6**	**6.8**	**89**
	—	*6.4*	*−9.0*	*40.9*	*4.70*	*313.7*	*328.3*	*3.2*	*69*

Appendix B: Repository of African Dust Days.

Table B.1 Repository of African Dust Days (ADD) with its corresponding Aerosol Optical Depth (AOD) and extinction Ångström exponent (***å***).

Date	AOD_440nm	440-870_Angstrom_Exponent
6/18/2004	0.32	0.12
6/19/2004	0.43	0.11
6/20/2004	0.44	0.13
6/23/2004	0.49	0.08
6/24/2004	0.52	0.15
6/27/2004	0.20	0.16
7/2/2004	0.21	0.17
7/3/2004	0.21	0.18
7/4/2004	0.24	0.16
7/5/2004	0.29	0.11
7/8/2004	0.37	0.14
7/9/2004	0.40	0.14
7/10/2004	0.28	0.19
7/11/2004	0.20	0.17
7/13/2004	0.26	0.19
7/15/2004	0.27	0.08
7/22/2004	0.42	0.17
7/23/2004	0.23	0.34
7/26/2004	0.31	0.25
7/28/2004	0.30	0.32
8/1/2004	0.35	0.13
8/6/2004	0.36	0.06
8/7/2004	0.22	0.22
8/11/2004	0.38	0.18
8/15/2004	0.23	0.18
8/21/2004	0.46	0.07
8/22/2004	0.47	0.08
8/23/2004	0.22	0.17
9/10/2004	0.22	0.23
4/2/2005	0.22	0.58
4/3/2005	0.23	0.59
4/15/2005	0.22	0.22
5/29/2005	0.40	0.16
5/30/2005	0.32	0.24
5/31/2005	0.42	0.14
6/1/2005	0.36	0.18
6/2/2005	0.22	0.07

6/3/2005	0.23	0.27
6/19/2005	0.21	0.53
6/20/2005	0.37	0.06
6/21/2005	0.35	0.09
6/23/2005	0.28	0.37
7/1/2005	0.81	0.12
7/2/2005	0.28	0.24
7/5/2005	0.31	0.10
7/8/2005	0.32	0.14
7/15/2005	0.28	0.06
7/16/2005	0.20	0.22
7/21/2005	0.39	0.16
7/23/2005	0.34	0.22
7/24/2005	0.77	0.19
7/25/2005	0.45	0.21
7/26/2005	0.26	0.20
8/3/2005	0.52	0.42
8/4/2005	0.58	0.11
8/5/2005	0.60	0.13
8/6/2005	0.22	0.28
9/1/2005	0.41	0.23
9/2/2005	0.40	0.10
9/3/2005	0.38	0.12
9/4/2005	0.31	0.20
9/9/2005	0.68	0.09
9/27/2005	0.20	0.45
5/22/2006	0.23	
5/23/2006	0.23	
5/24/2006	0.24	
6/5/2006	0.35	
6/6/2006	0.33	
6/7/2006	0.33	
6/9/2006	0.37	
6/10/2006	0.42	
6/11/2006	0.25	
6/13/2006	0.33	
6/14/2006	0.21	
6/15/2006	0.30	
6/23/2006	0.41	
6/25/2006	0.49	
6/26/2006	0.45	
6/27/2006	0.32	
7/4/2006	0.40	

7/6/2006	0.57	
7/9/2006	0.31	
7/11/2006	0.30	
7/13/2006	0.26	
7/16/2006	0.54	
7/20/2006	0.39	
7/23/2006	0.35	
7/26/2006	0.24	
7/30/2006	0.36	
7/31/2006	0.32	
8/21/2006	0.22	0.11
8/23/2006	0.52	0.08
8/24/2006	0.58	0.07
9/5/2006	0.38	0.17
9/9/2006	0.20	0.06
9/16/2006	0.35	0.08
9/17/2006	0.29	0.13
10/10/2006	0.25	0.27
3/8/2007	0.39	0.38
3/9/2007	0.64	0.36
3/10/2007	0.31	0.36
3/11/2007	0.27	0.23
4/20/2007	0.38	0.58
5/13/2007	0.22	0.24
5/14/2007	0.34	0.40
5/16/2007	0.61	0.06
5/18/2007	0.66	0.19
5/19/2007	0.53	0.33
5/20/2007	0.27	0.16
6/2/2007	0.20	0.45
6/3/2007	0.41	0.18
6/4/2007	0.32	0.22
6/5/2007	0.36	0.29
6/6/2007	0.29	0.18
6/15/2007	0.58	0.10
6/16/2007	0.49	0.10
6/17/2007	0.25	0.13
6/22/2007	0.46	0.09
6/23/2007	0.20	0.15
6/26/2007	0.63	0.08
6/29/2007	0.21	0.23
6/30/2007	0.23	0.23
7/1/2007	0.71	0.19

7/2/2007	0.45	0.08
7/3/2007	0.23	0.08
7/6/2007	0.21	0.10
7/9/2007	0.28	0.08
7/10/2007	0.31	0.12
7/12/2007	0.52	0.10
7/13/2007	0.51	0.11
7/15/2007	0.20	0.16
7/17/2007	0.23	0.25
7/18/2007	0.45	0.13
7/21/2007	0.65	0.04
7/22/2007	0.33	0.14
7/23/2007	0.36	0.11
7/24/2007	0.43	0.16
7/25/2007	0.41	0.17
7/26/2007	0.38	0.11
7/27/2007	0.41	0.09
7/28/2007	0.42	0.11
7/29/2007	0.24	0.16
8/2/2007	0.32	0.28
8/3/2007	0.47	0.32
8/4/2007	0.36	0.27
8/5/2007	0.29	0.31
8/9/2007	0.28	0.18
8/12/2007	0.53	0.16
8/13/2007	0.25	0.25
8/16/2007	0.31	0.11
8/17/2007	0.34	0.08
8/20/2007	0.21	0.22
8/21/2007	0.25	0.49
8/31/2007	0.25	0.55
9/11/2007	0.31	0.30
9/12/2007	0.29	0.31
10/12/2007	0.27	0.19
10/31/2007	0.37	0.26
11/1/2007	0.21	0.22
11/2/2007	0.22	0.47
12/13/2007	0.38	0.37
4/23/2008	0.20	0.35
4/28/2008	0.28	0.22
5/7/2008	0.20	0.29
5/8/2008	0.32	0.39
5/9/2008	0.52	0.10

5/10/2008	0.33	0.32
6/16/2008	0.23	0.18
6/20/2008	0.34	0.11
6/21/2008	0.42	0.10
6/23/2008	0.29	0.07
6/25/2008	0.63	0.09
6/27/2008	0.34	0.26
6/28/2008	0.45	0.10
7/3/2008	0.26	0.20
7/11/2008	0.32	0.25
7/12/2008	0.42	0.18
7/13/2008	0.25	0.26
7/16/2008	0.20	0.22
7/17/2008	0.29	0.19
7/19/2008	0.25	0.24
7/20/2008	0.22	0.24
7/21/2008	0.35	0.21
7/22/2008	0.43	0.22
7/23/2008	0.20	0.25
7/30/2008	0.34	0.16
7/31/2008	0.22	0.34
8/3/2008	0.23	0.09
8/6/2008	0.47	0.10
8/7/2008	0.53	0.10
8/8/2008	0.34	0.18
8/11/2008	0.36	0.14
8/12/2008	0.28	0.30
8/16/2008	0.30	0.18
8/17/2008	0.23	0.39
8/22/2008	0.35	0.08
8/23/2008	0.22	0.14
5/24/2009	0.22	0.54
5/27/2009	0.36	0.20
5/28/2009	0.50	0.23
6/8/2009	0.24	0.35
6/9/2009	0.30	0.13
6/10/2009	0.38	0.16
6/11/2009	0.33	0.18
6/13/2009	0.27	0.56
6/26/2009	0.44	0.11
6/27/2009	0.59	0.07
6/28/2009	0.43	0.12
6/29/2009	0.41	0.16

7/4/2009	0.74	0.04
7/6/2009	0.58	0.05
7/7/2009	0.49	0.09
7/11/2009	0.48	0.20
7/12/2009	0.23	0.25
7/14/2009	0.22	0.10
7/15/2009	0.56	0.08
7/16/2009	0.58	0.13
7/17/2009	0.24	0.25
7/20/2009	0.46	-0.01
7/24/2009	0.42	0.19
7/25/2009	0.36	0.14
7/27/2009	0.24	0.07
7/28/2009	0.36	0.08
7/29/2009	0.27	0.16
7/31/2009	0.29	0.22
8/4/2009	0.20	0.19
8/5/2009	0.24	0.22
8/6/2009	0.27	0.27
8/7/2009	0.51	0.14
8/8/2009	0.36	0.24
8/14/2009	0.23	0.20
8/18/2009	0.36	0.15
8/22/2009	0.24	0.18
8/25/2009	0.27	0.23
8/27/2009	0.38	0.22
9/1/2009	0.25	0.33
9/7/2009	0.30	0.22
10/6/2009	0.34	0.22
11/6/2009	0.20	0.43
3/3/2010	0.26	0.29
3/4/2010	0.29	0.40
3/5/2010	0.30	0.48
3/19/2010	0.27	0.23
3/20/2010	0.21	0.29
4/27/2010	0.23	0.20
4/28/2010	0.42	0.07
4/29/2010	0.41	0.08
4/30/2010	0.38	0.08
5/1/2010	0.25	0.40
5/20/2010	0.21	0.44
6/1/2010	0.38	0.32
6/3/2010	1.20	0.11

6/4/2010	1.09	0.09
6/5/2010	0.65	0.12
6/6/2010	0.53	0.22
6/10/2010	0.34	0.06
7/1/2010	0.68	0.04
7/2/2010	0.73	0.08
7/3/2010	0.63	0.06
7/4/2010	0.33	0.11
7/7/2010	0.56	0.04
7/8/2010	0.35	0.06
7/10/2010	0.33	0.13
7/11/2010	0.63	0.05
7/12/2010	0.39	0.05
7/13/2010	0.31	-0.03
7/15/2010	0.41	0.09
7/24/2010	0.35	0.17
7/25/2010	0.36	0.08
8/7/2010	0.29	0.16
9/21/2010	0.49	0.04
9/22/2010	0.44	0.07
4/30/2011	0.25	0.54
5/14/2011	0.26	0.51
5/15/2011	0.21	0.52
5/28/2011	0.30	0.57
5/31/2011	0.24	0.36
6/9/2011	0.25	0.27
6/11/2011	0.22	0.37
6/12/2011	0.20	0.34
6/14/2011	0.21	0.57
6/17/2011	0.20	0.36
6/21/2011	0.38	0.16
6/22/2011	0.40	0.13
6/23/2011	0.33	0.20
6/24/2011	0.22	0.50
6/25/2011	0.23	0.39
6/29/2011	0.54	0.23
6/30/2011	0.59	0.10
7/1/2011	0.28	0.23
7/5/2011	0.34	0.39
7/6/2011	0.26	0.33
7/14/2011	0.37	0.59
7/16/2011	0.20	0.51
7/17/2011	0.24	0.50

7/18/2011	0.25	0.39
7/21/2011	0.24	0.38
7/25/2011	0.26	0.27
8/1/2011	0.27	0.34
8/5/2011	0.85	0.13
8/8/2011	0.25	0.34
8/9/2011	0.33	0.24
8/10/2011	0.20	0.44
8/11/2011	0.30	0.41
8/12/2011	0.34	0.28
8/15/2011	0.23	0.38
8/16/2011	0.44	0.13
8/18/2011	0.22	0.32
8/20/2011	0.33	0.22
8/26/2011	0.21	0.26
9/9/2011	0.53	0.14
9/10/2011	0.26	0.34
9/16/2011	0.32	0.28
10/5/2011	0.25	0.37
10/6/2011	0.23	0.51
10/14/2011	0.21	0.14
11/5/2011	0.26	0.12
5/13/2012	0.58	0.23
5/14/2012	0.40	0.21
5/20/2012	0.20	0.47
5/22/2012	0.25	0.40
5/23/2012	0.24	0.24
5/24/2012	0.20	0.20
5/29/2012	0.31	0.53
5/30/2012	0.27	0.23
5/31/2012	0.31	0.34
6/1/2012	0.30	0.30
6/2/2012	0.57	0.21
6/3/2012	0.51	0.18
6/4/2012	0.41	0.24
6/5/2012	0.29	0.34
6/8/2012	0.20	0.28
6/12/2012	0.32	0.15
6/13/2012	0.35	0.13
6/14/2012	0.28	0.19
6/15/2012	0.24	0.20
6/16/2012	0.32	0.20
6/20/2012	0.39	0.18

6/21/2012	0.58	0.10
6/22/2012	0.46	0.21
6/23/2012	0.34	0.16
6/26/2012	0.34	0.14
6/27/2012	0.54	0.12
6/28/2012	0.23	0.28
7/2/2012	0.28	0.08
7/3/2012	0.40	0.10
7/4/2012	0.35	0.10
7/6/2012	0.48	0.11
7/10/2012	0.41	0.01
7/11/2012	0.32	0.10
7/16/2012	0.43	0.11
7/17/2012	0.41	0.18
7/21/2012	0.21	0.21
7/22/2012	0.48	0.15
7/24/2012	0.46	0.17
7/25/2012	0.38	0.25
7/26/2012	0.25	0.25
7/30/2012	0.27	0.22
8/1/2012	0.35	0.14
8/2/2012	0.28	0.18
8/5/2012	0.52	0.10
8/6/2012	0.22	0.30
8/9/2012	0.29	0.45
8/10/2012	0.26	0.29
8/11/2012	0.55	0.16
8/12/2012	0.21	0.23
8/18/2012	0.32	0.17
8/19/2012	0.34	0.30
8/20/2012	0.42	0.29
8/21/2012	0.26	0.26
8/22/2012	0.24	0.27
9/5/2012	0.28	0.59
9/7/2012	0.26	0.34
9/8/2012	0.22	0.50
9/9/2012	0.22	0.35
9/11/2012	0.23	0.06
5/28/2013	0.26	0.16
5/29/2013	0.25	0.20
5/30/2013	0.24	0.16
5/31/2013	0.30	0.13
6/1/2013	0.28	0.13

6/2/2013	0.25	0.09
6/3/2013	0.23	0.14
6/4/2013	0.36	0.11
6/5/2013	0.62	0.05
6/6/2013	0.41	0.10
6/9/2013	0.24	0.13
6/12/2013	0.31	0.10
6/13/2013	0.32	0.10
6/15/2013	0.30	0.07
6/16/2013	0.68	0.06
6/18/2013	0.49	0.08
6/19/2013	0.21	0.22
6/21/2013	0.41	0.15
6/27/2013	0.33	0.18
6/28/2013	0.23	0.18
6/29/2013	0.28	0.17
7/1/2013	0.44	0.16
7/3/2013	0.30	0.19
7/4/2013	0.37	0.21
7/6/2013	0.20	0.28
7/9/2013	0.26	0.16
7/10/2013	0.54	0.14
7/16/2013	0.24	0.20
7/17/2013	0.22	0.19
7/18/2013	0.34	0.14
7/19/2013	0.32	0.18
7/22/2013	0.35	0.17
7/23/2013	0.35	0.28
8/1/2013	0.47	0.18
8/2/2013	0.49	0.15
8/3/2013	0.47	0.17
8/9/2013	0.36	0.17
8/10/2013	0.28	0.18
8/11/2013	0.27	0.19
8/13/2013	0.29	0.18
8/14/2013	0.30	0.15
8/15/2013	0.31	0.17
8/18/2013	0.21	0.27
8/30/2013	0.26	0.07
9/9/2013	0.50	0.11
10/1/2013	0.46	0.10
11/11/2013	0.26	0.27
1/20/2014	0.24	0.45

3/22/2014	0.28	0.45
4/9/2014	0.21	0.59
5/2/2014	0.20	0.44
6/3/2014	0.44	0.12
6/9/2014	0.29	0.11
6/10/2014	0.35	0.13
6/11/2014	0.43	0.10
6/12/2014	0.28	0.13
6/25/2014	0.21	0.12
6/26/2014	0.69	0.06
6/27/2014	0.49	0.07
6/29/2014	0.35	0.13
6/30/2014	0.43	0.05
7/1/2014	0.27	0.08
7/2/2014	0.52	0.09
7/4/2014	0.31	0.12
7/6/2014	0.24	0.09
7/7/2014	0.49	0.08
7/8/2014	0.20	0.14
7/11/2014	0.41	0.05
7/12/2014	0.34	0.09
7/15/2014	0.25	0.14
7/20/2014	0.42	0.08
7/23/2014	0.44	0.11
7/24/2014	0.23	0.03
7/25/2014	0.21	0.05
7/26/2014	0.58	0.07
7/27/2014	0.53	0.07
7/28/2014	0.32	0.08
8/1/2014	0.25	0.02
8/3/2014	0.28	0.08
8/4/2014	0.24	0.16
8/6/2014	0.20	0.20
8/7/2014	0.23	0.12
8/11/2014	0.40	0.01
8/12/2014	0.24	-0.01
8/13/2014	0.37	0.05
8/14/2014	0.34	0.07
8/15/2014	0.34	0.10
8/17/2014	0.33	-0.02
8/18/2014	0.41	0.05
8/27/2014	0.32	0.07
9/3/2014	0.49	0.04

9/8/2014	0.24	0.17
9/12/2014	0.43	0.09
10/3/2014	0.41	0.09
10/4/2014	0.28	0.13
10/5/2014	0.26	0.15
10/6/2014	0.24	0.17
4/19/2015	0.22	0.35
4/28/2015	0.41	0.20
4/29/2015	0.40	0.20
4/30/2015	0.23	0.27
5/1/2015	0.21	0.29
5/2/2015	0.21	0.36
5/4/2015	0.30	0.32
5/5/2015	0.23	0.31
5/6/2015	0.27	0.23
5/7/2015	0.42	0.20
5/8/2015	0.38	0.20
5/13/2015	0.32	0.22
5/22/2015	0.48	0.17
5/23/2015	0.38	0.15
5/24/2015	0.31	0.13
5/25/2015	0.23	0.22
6/1/2015	0.29	0.35
6/2/2015	0.23	0.57
6/6/2015	0.41	0.23
6/7/2015	0.43	0.25
6/8/2015	0.38	0.13
6/9/2015	0.41	0.10
6/13/2015	0.38	0.09
6/14/2015	0.41	0.09
6/15/2015	0.36	0.15
6/16/2015	0.35	0.10
6/18/2015	0.74	0.04
6/19/2015	0.64	0.08
6/20/2015	0.37	0.18
6/22/2015	0.22	0.10
6/23/2015	0.39	0.06
6/24/2015	0.60	0.10
6/25/2015	0.30	0.19
6/26/2015	0.27	0.14
6/27/2015	0.34	0.10
6/28/2015	0.79	0.05
6/29/2015	0.50	0.11

7/2/2015	0.45	0.12
7/3/2015	0.38	0.09
7/4/2015	0.50	0.10
7/6/2015	0.27	0.24
7/7/2015	0.32	0.18
7/8/2015	0.56	0.20
7/9/2015	0.58	0.18
7/13/2015	0.35	0.09
7/15/2015	0.31	0.26
7/17/2015	0.27	0.26
7/19/2015	0.21	0.20
7/21/2015	0.24	0.21
7/22/2015	0.20	0.32
7/23/2015	0.30	0.24
7/24/2015	0.25	0.34
7/26/2015	0.29	0.16
7/27/2015	0.38	0.18
7/28/2015	0.42	0.10
7/29/2015	0.21	0.32
7/30/2015	0.29	0.14
7/31/2015	0.24	0.11
8/1/2015	0.26	0.24
8/3/2015	0.28	0.18
8/20/2015	0.31	0.17
8/21/2015	0.40	0.16
8/22/2015	0.31	0.20
8/26/2015	0.42	0.08
8/29/2015	0.20	0.26
8/31/2015	0.23	0.24
9/16/2015	0.28	0.14
9/17/2015	0.38	0.12
10/6/2015	0.21	0.39
10/9/2015	0.23	0.19
10/10/2015	0.36	0.09
1/27/2016	0.21	0.19
2/7/2016	0.22	0.32
2/8/2016	0.20	0.38
5/22/2016	0.21	0.21
5/23/2016	0.26	0.30
6/3/2016	0.58	0.07
6/4/2016	0.48	0.06
6/5/2016	0.41	0.18
6/6/2016	0.21	0.20

6/7/2016	0.22	0.16
6/9/2016	0.35	0.18
6/10/2016	0.34	0.18
6/13/2016	0.35	0.10
6/14/2016	0.37	0.07
6/15/2016	0.44	0.11
6/16/2016	0.42	0.06
6/24/2016	0.33	0.19
6/25/2016	0.45	0.10
6/26/2016	0.41	0.17
6/29/2016	0.22	0.22
7/3/2016	0.35	0.13
7/6/2016	0.47	0.07
7/7/2016	0.32	0.15
7/11/2016	0.52	0.10
7/17/2016	0.21	0.23
7/21/2016	0.31	0.11
7/22/2016	0.37	0.09
7/27/2016	0.35	0.10
7/28/2016	0.31	0.13
8/3/2016	0.20	0.28
8/15/2016	0.23	0.23
8/18/2016	0.28	0.25
8/19/2016	0.22	0.28
8/20/2016	0.23	0.38
9/3/2016	0.48	0.10
9/4/2016	0.52	0.07
9/5/2016	0.48	0.06
9/6/2016	0.31	0.12
9/28/2016	0.22	0.16
10/9/2016	0.20	0.12
10/10/2016	0.25	0.18
5/23/2017	0.62	0.07
5/24/2017	0.62	0.07
6/5/2017	0.23	0.20
6/26/2017	0.49	0.09
6/27/2017	0.36	0.09
7/10/2017	0.35	0.10
7/11/2017	0.40	0.10
7/19/2017	0.45	0.07
7/20/2017	0.51	0.05
7/24/2017	0.32	0.09
8/1/2017	0.32	0.13

8/3/2017	0.29	0.08
8/12/2017	0.22	0.20
8/15/2017	0.33	0.16
8/18/2017	0.22	0.07
8/21/2017	0.39	0.23
8/22/2017	0.29	0.30
8/23/2017	0.28	0.37
8/24/2017	0.31	0.19
8/25/2017	0.29	0.18
8/30/2017	0.31	0.15
8/31/2017	0.27	0.23
9/1/2017	0.21	0.18
10/19/2017	0.56	0.10
10/20/2017	0.28	0.17
4/19/2018	0.21	0.50
6/2/2018	0.36	0.20
6/3/2018	0.27	0.12
6/4/2018	0.26	0.16
6/5/2018	0.22	0.17
6/6/2018	0.33	0.23
6/7/2018	0.33	0.09
6/12/2018	0.40	0.05
6/13/2018	0.39	0.05
6/14/2018	0.39	0.08
6/16/2018	0.22	0.25
6/17/2018	0.29	0.33
6/21/2018	0.25	0.17
6/24/2018	0.39	0.06
6/25/2018	0.31	0.07
6/26/2018	0.72	0.04
6/27/2018	0.72	0.04
6/30/2018	0.56	0.08
7/1/2018	0.49	0.07
7/2/2018	0.30	0.10
7/3/2018	0.37	0.08
7/4/2018	0.59	0.05
7/5/2018	0.34	0.14
7/6/2018	0.37	0.09
7/7/2018	0.45	0.11
7/13/2018	0.49	0.07
7/15/2018	0.26	0.13
7/17/2018	0.63	0.07
7/18/2018	0.22	0.17

7/20/2018	0.64	0.11
7/21/2018	0.79	0.16
7/25/2018	0.23	0.13
7/26/2018	0.43	0.10
7/27/2018	0.40	0.14
7/31/2018	0.28	0.22
8/4/2018	0.57	0.11
8/5/2018	0.73	0.12
8/6/2018	0.51	0.15
8/7/2018	0.74	0.13
8/8/2018	0.33	0.29
8/10/2018	0.28	0.24
8/28/2018	0.23	0.32
8/31/2018	0.22	0.28
9/1/2018	0.20	0.41
9/13/2018	0.25	0.15
9/19/2018	0.23	0.23
9/20/2018	0.52	0.10
9/21/2018	0.28	0.18
9/29/2018	0.24	0.37
9/30/2018	0.38	0.18
10/1/2018	0.20	0.40
10/2/2018	0.22	0.38

Appendix C: Ice in Clouds – Tropical (ICE-T), Supplemental Material.

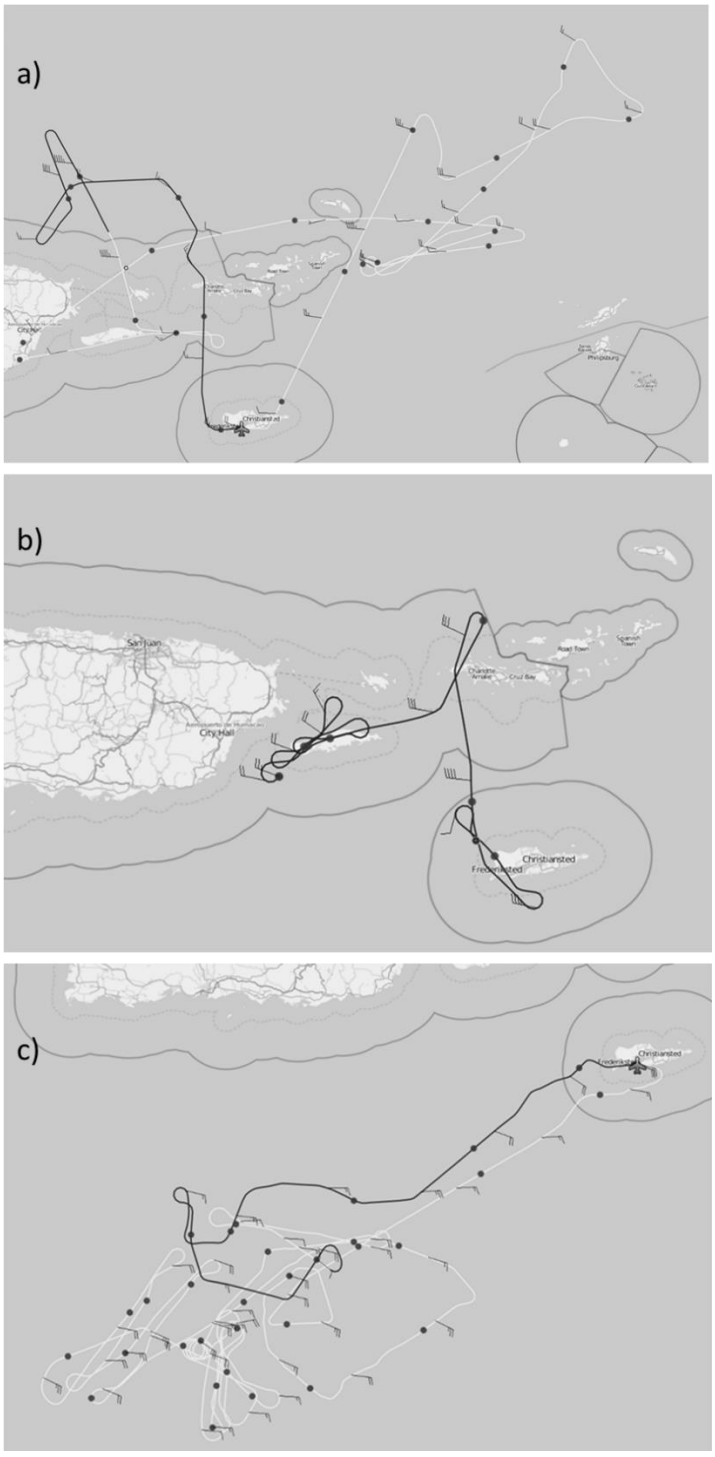

Figure C.1 Ice in Clouds -Tropical (ICE-T) flight paths during Research Flights (RF), a) RF03, b) RF06, and c) RF13. **Yellow line** – *cumulus clouds analyzed*. **Red line** – *no cumulus clouds observed*.

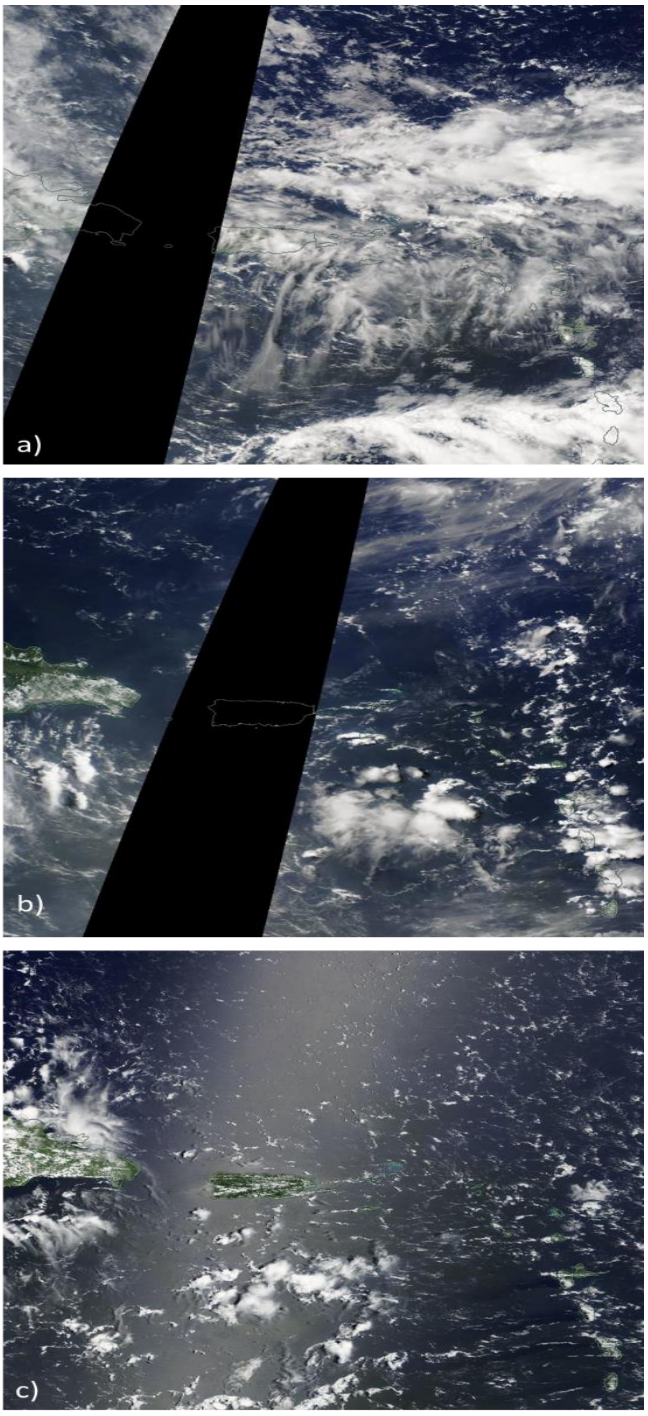

Figure C.2 Snapshot (visible imagery) retrieved from the MODerate Resolution Imaging Spectroradiometer (MODIS) during the days corresponding to Research Flights (RF), a) RF03, b) RF06 and c) RF13. Brownish/darker colors suggest African dust. **No data** – *black area.* **Sunglint,** which is a phenomenon that occurs when sunlight reflects off the surface of the ocean at the same angle that a satellite is viewing the surface – *almost a vertical gray area*.

Appendix D: Rainfall and the Standardized Precipitation Index.

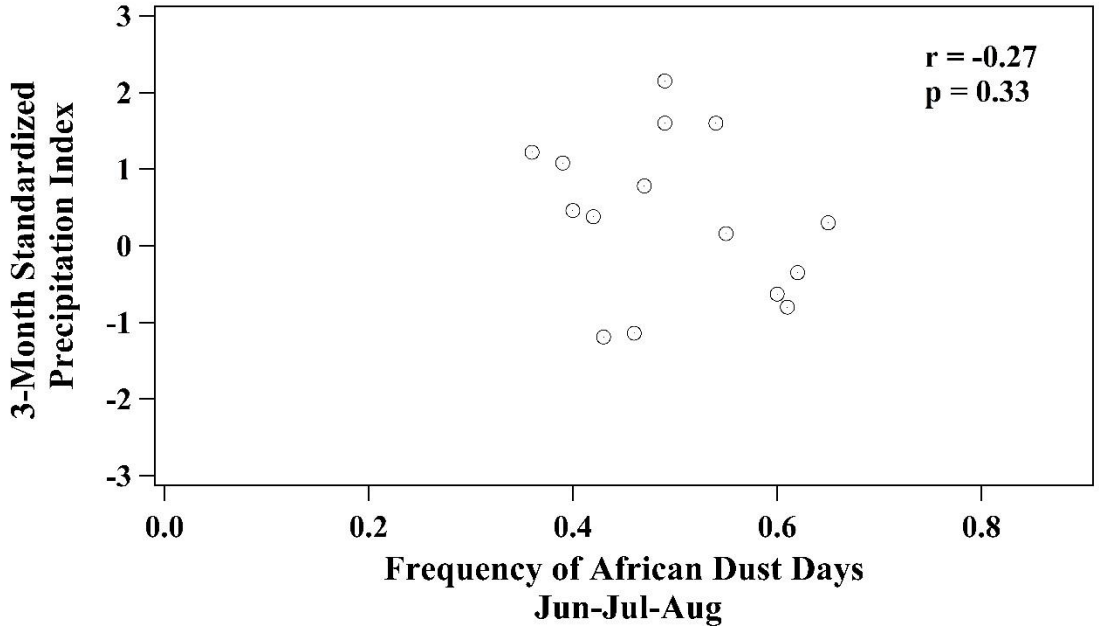

Figure D.1 Correlation between Frequency of African Dust Days (ADD) during Jun-Jul-Aug (JJA) and its corresponding 3-month standardized precipitation index (SPI) ending in August at Adjuntas Substation.

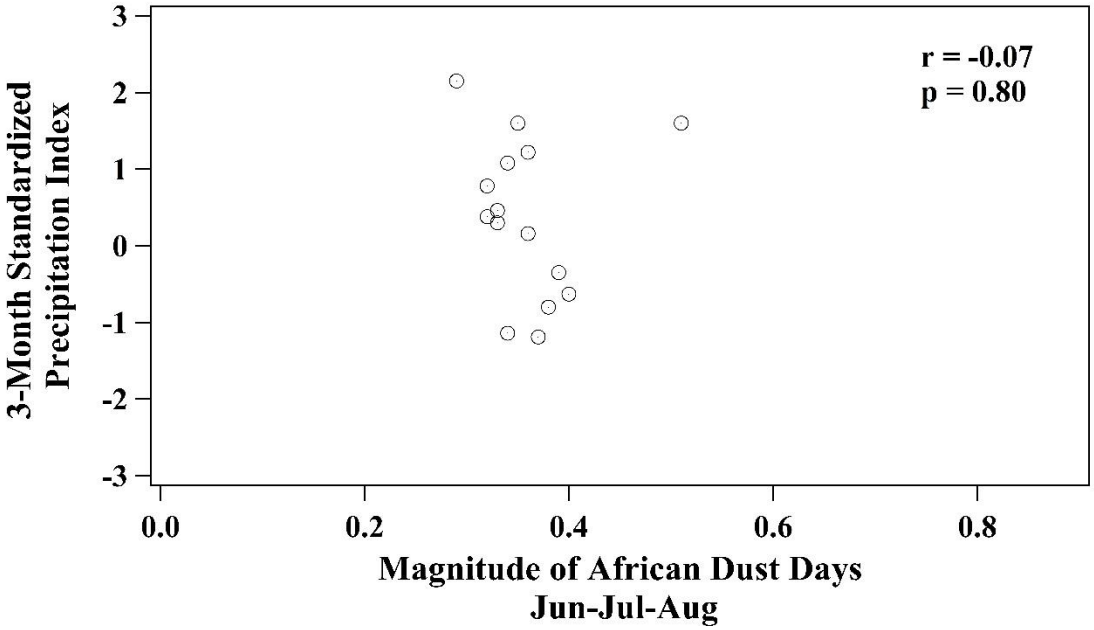

Figure D.2 Correlation between Magnitude of African Dust Days (ADD) during Jun-Jul-Aug (JJA) and its corresponding 3-month standardized precipitation index (SPI) ending in August at Adjuntas Substation.

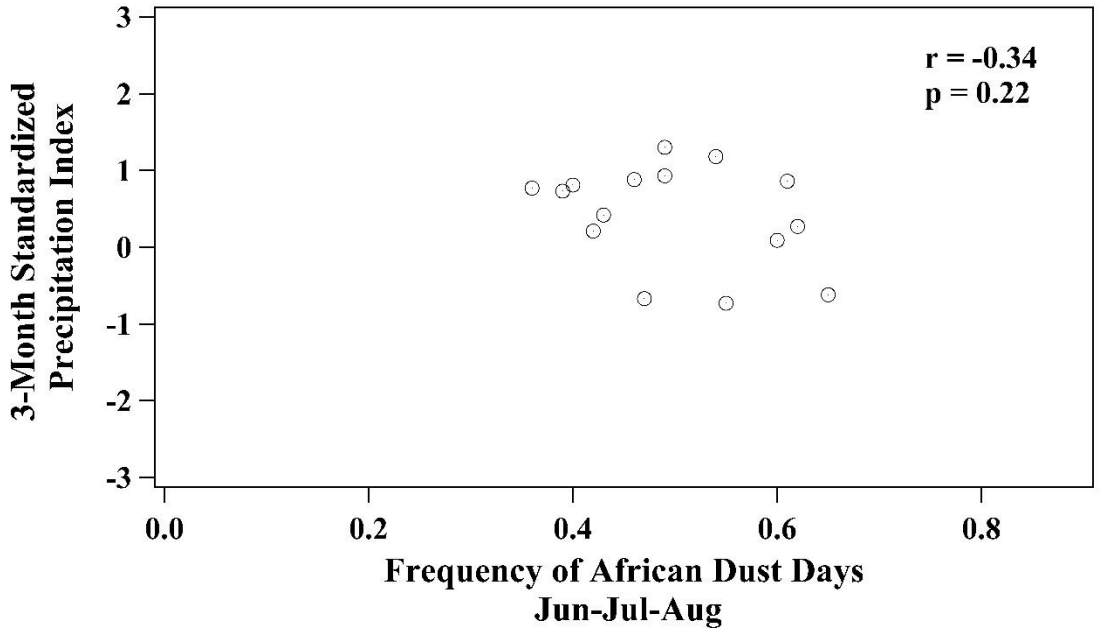

Figure D.3 Correlation between Frequency of African Dust Days (ADD) during Jun-Jul-Aug (JJA) and its corresponding 3-month standardized precipitation index (SPI) ending in August at Arecibo Observatory.

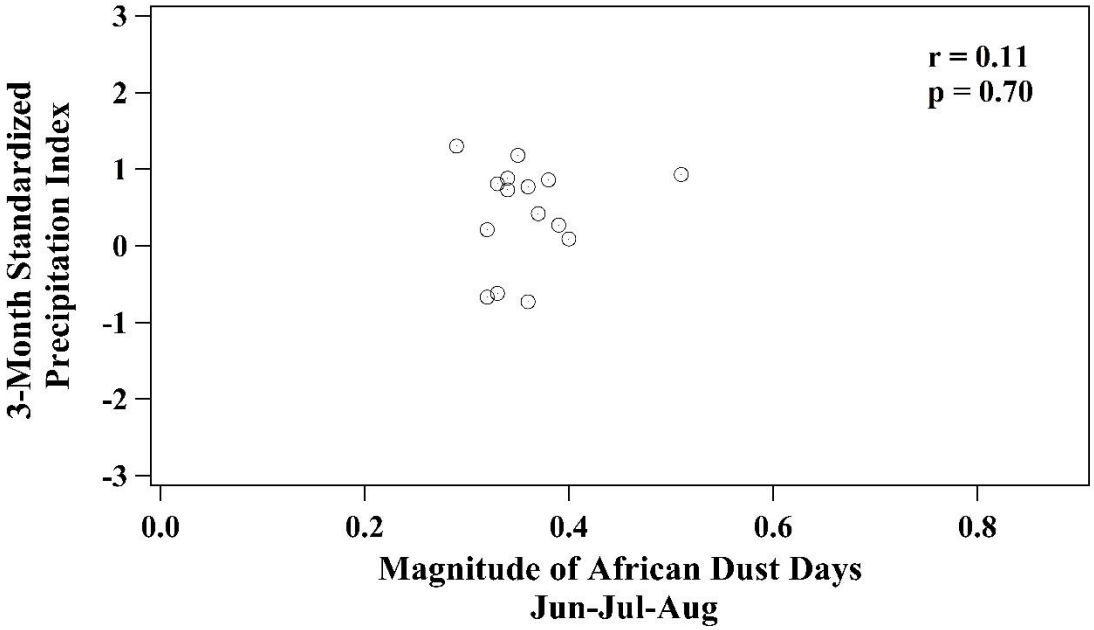

Figure D.4 Correlation between Magnitude of African Dust Days (ADD) during Jun-Jul-Aug (JJA) and its corresponding 3-month standardized precipitation index (SPI) ending in August at Arecibo Observatory.

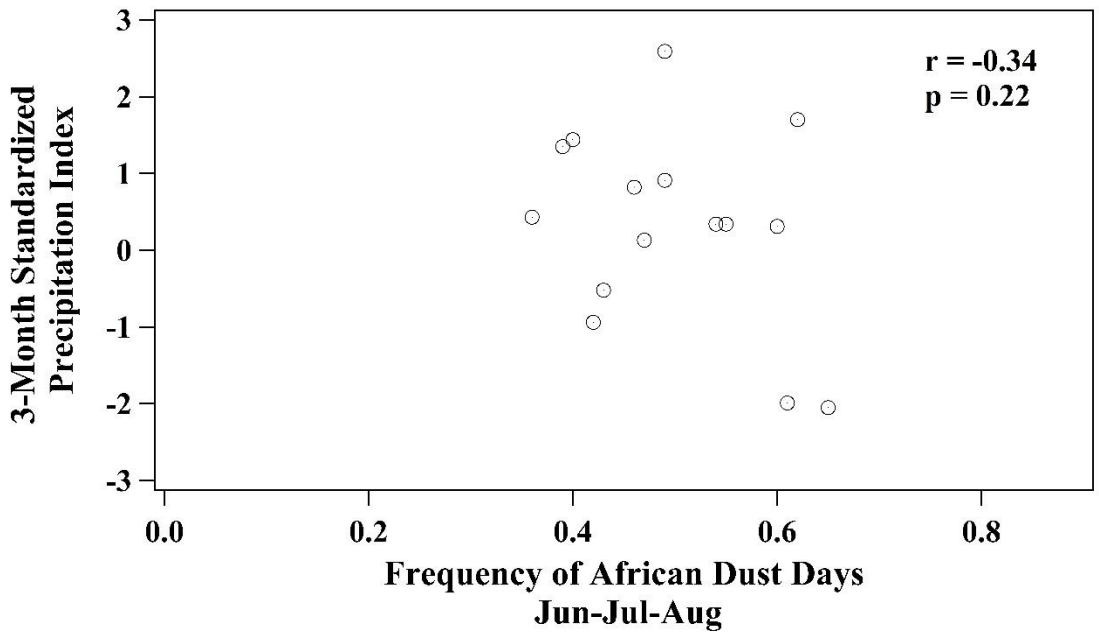

Figure D.5 Correlation between Frequency of African Dust Days (ADD) during Jun-Jul-Aug (JJA) and its corresponding 3-month standardized precipitation index (SPI) ending in August at Coloso.

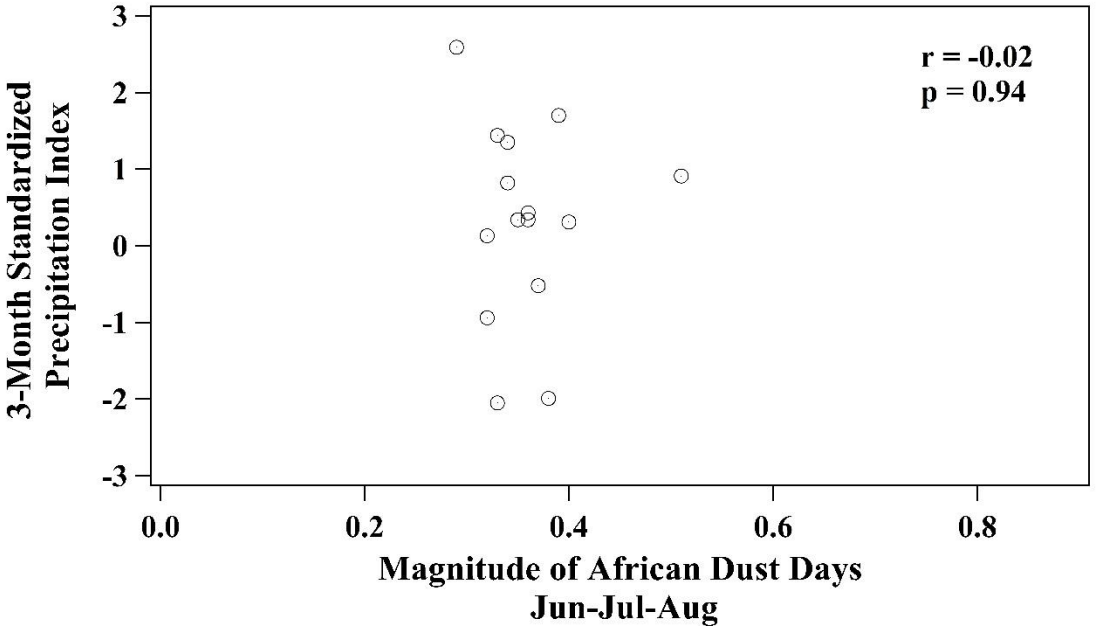

Figure D.6 Correlation between Magnitude of African Dust Days (ADD) during Jun-Jul-Aug (JJA) and its corresponding 3-month standardized precipitation index (SPI) ending in August at Coloso.

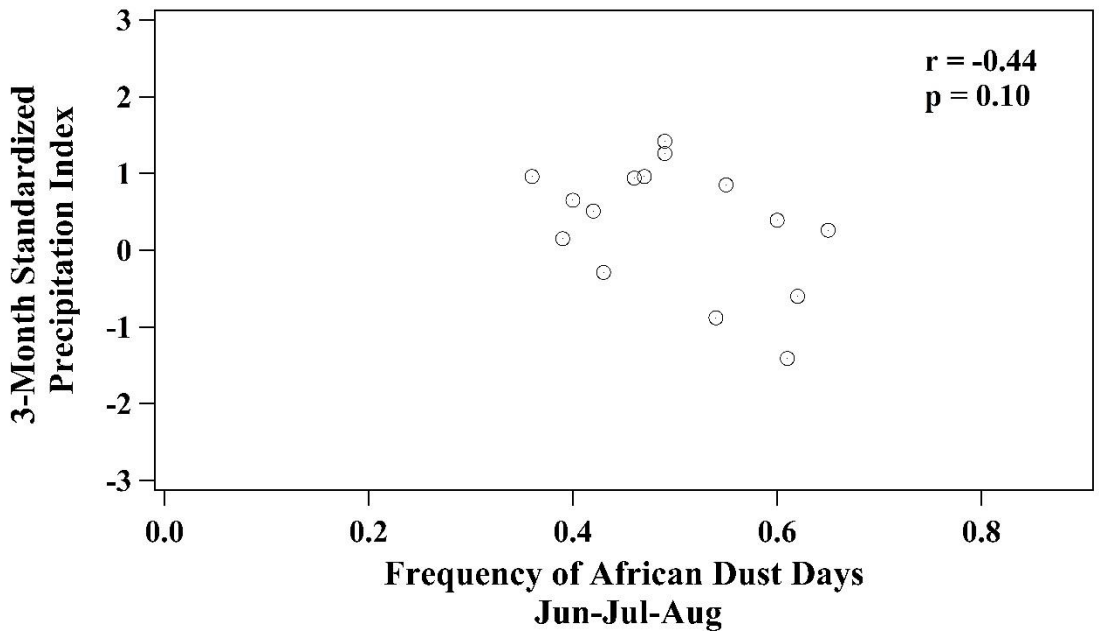

Figure D.7 Correlation between Frequency of African Dust Days (ADD) during Jun-Jul-Aug (JJA) and its corresponding 3-month standardized precipitation index (SPI) ending in August at Hacienda Constanza.

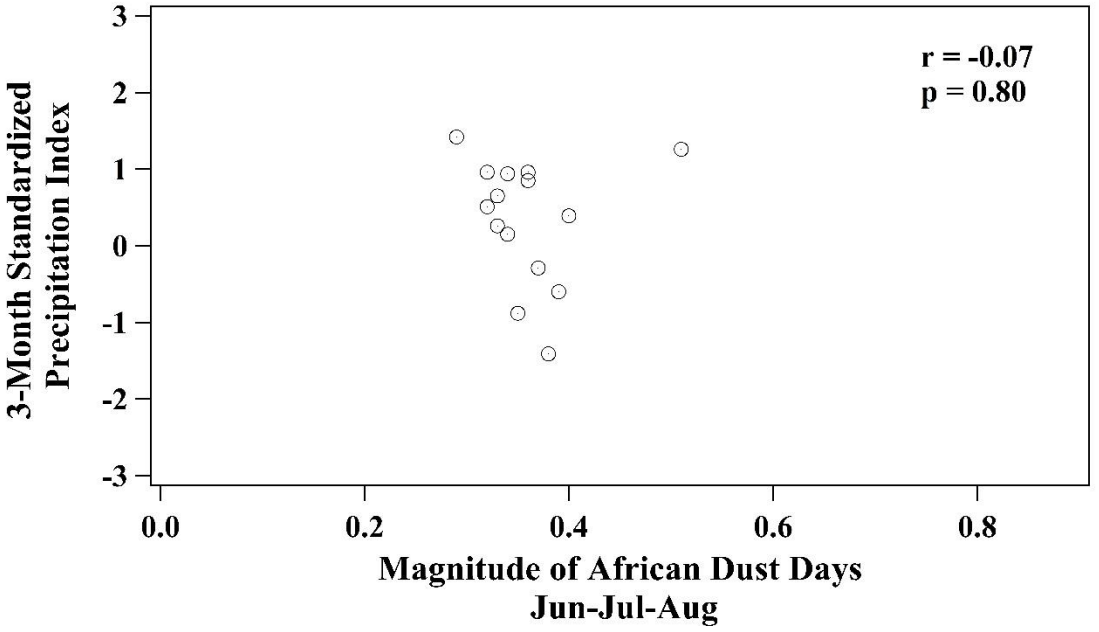

Figure D.8 Correlation between Magnitude of African Dust Days (ADD) during Jun-Jul-Aug (JJA) and its corresponding 3-month standardized precipitation index (SPI) ending in August at Hacienda Constanza.

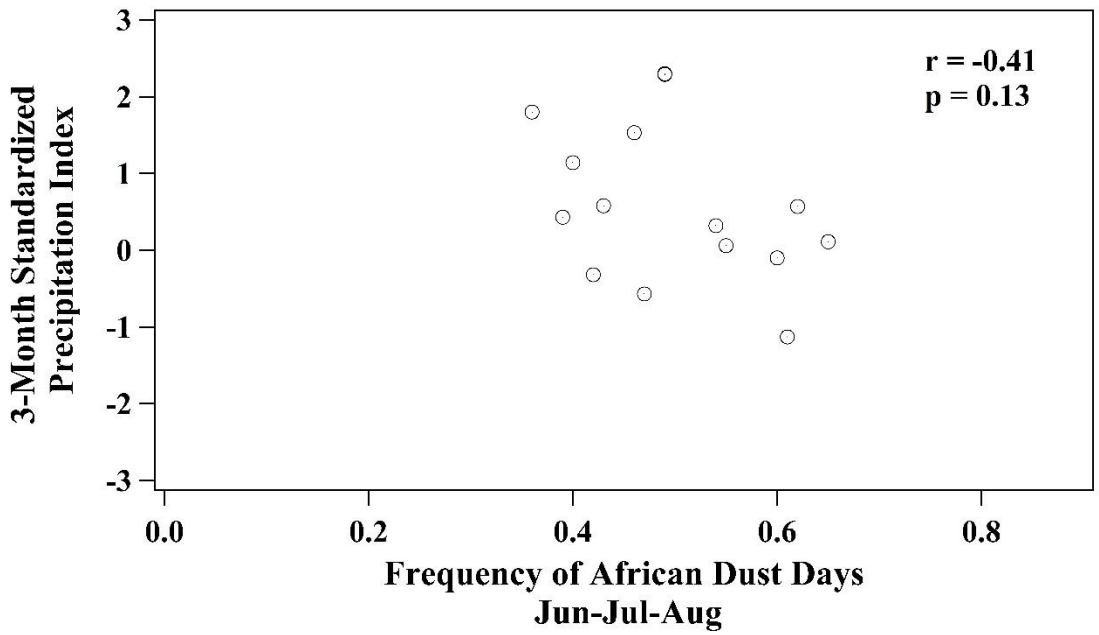

Figure D.9 Correlation between Frequency of African Dust Days (ADD) during Jun-Jul-Aug (JJA) and its corresponding 3-month standardized precipitation index (SPI) ending in August at Manati 2E.

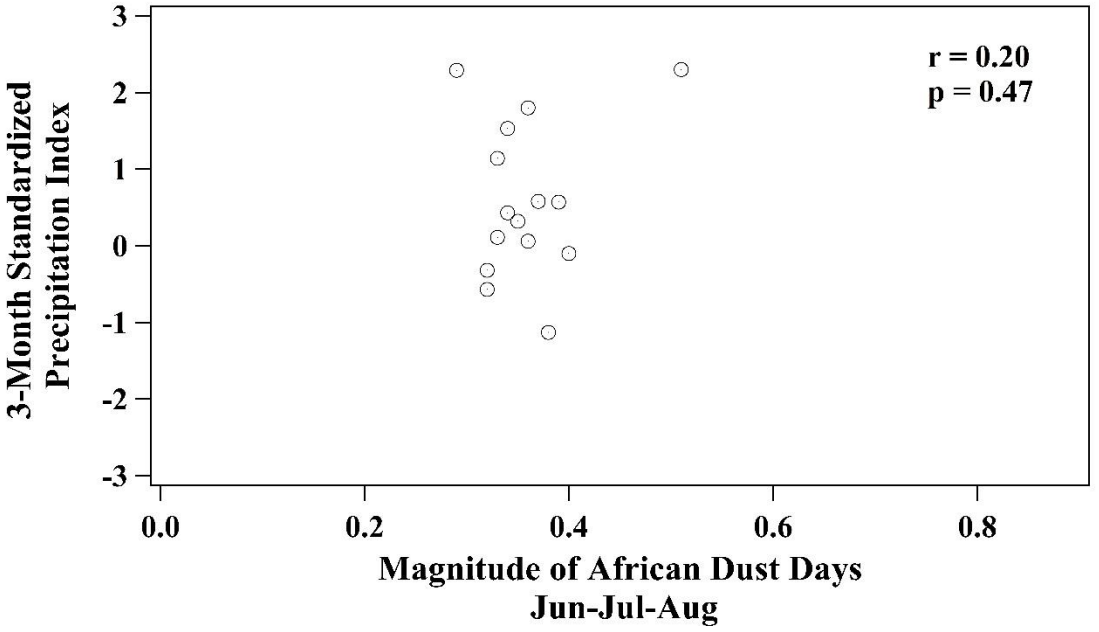

Figure D.10 Correlation between Magnitude of African Dust Days (ADD) during Jun-Jul-Aug (JJA) and its corresponding 3-month standardized precipitation index (SPI) ending in August at Manati 2E.

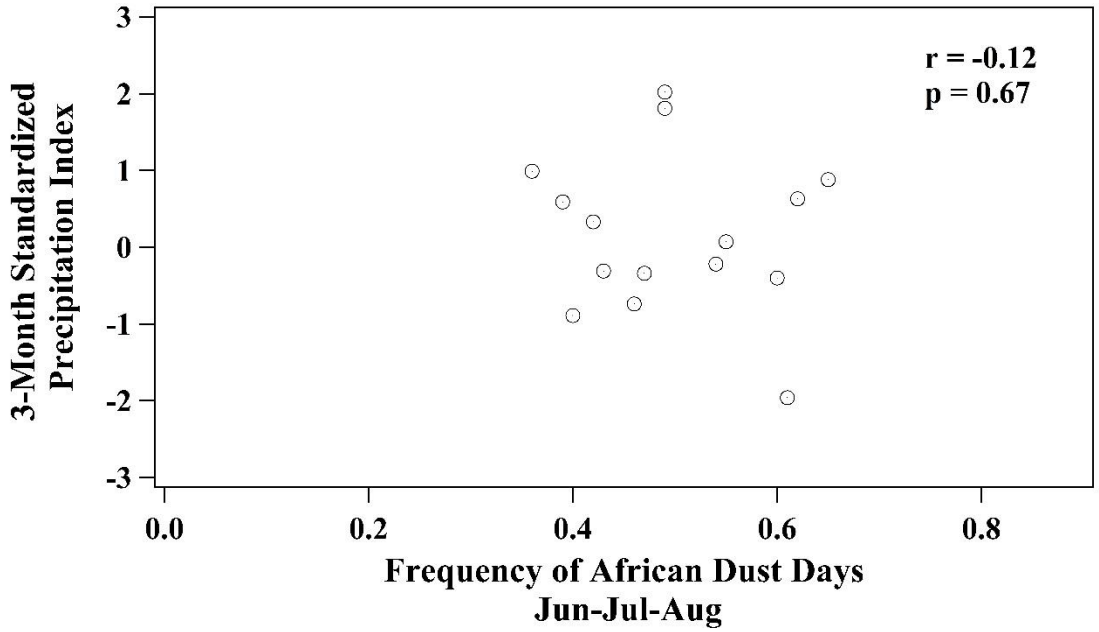

Figure D.11 Correlation between Frequency of African Dust Days (ADD) during Jun-Jul-Aug (JJA) and its corresponding 3-month standardized precipitation index (SPI) ending in August at Ponce 4E.

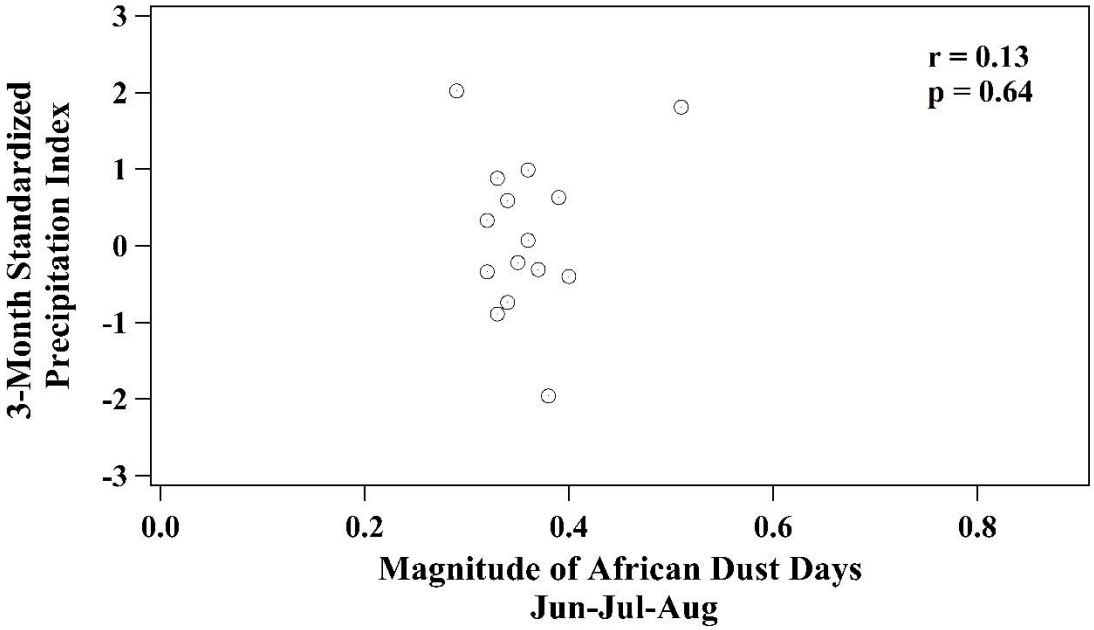

Figure D.12 Correlation between Magnitude of African Dust Days (ADD) during Jun-Jul-Aug (JJA) and its corresponding 3-month standardized precipitation index (SPI) ending in August at Ponce 4E.

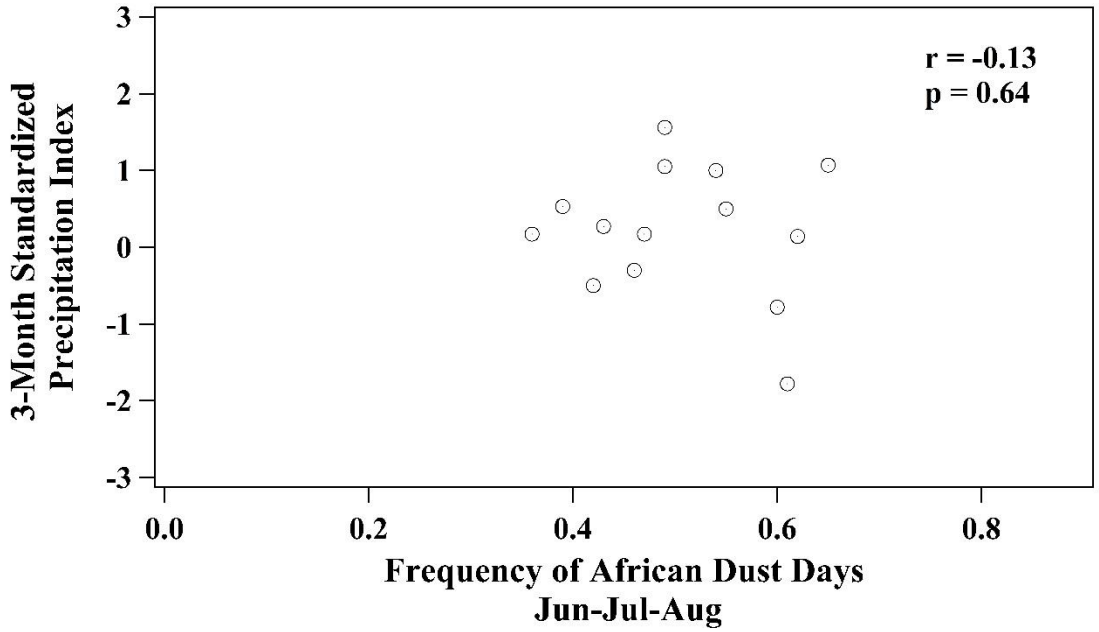

Figure D.13 Correlation between Frequency of African Dust Days (ADD) during Jun-Jul-Aug (JJA) and its corresponding 3-month standardized precipitation index (SPI) ending in August at Lajas Substation.

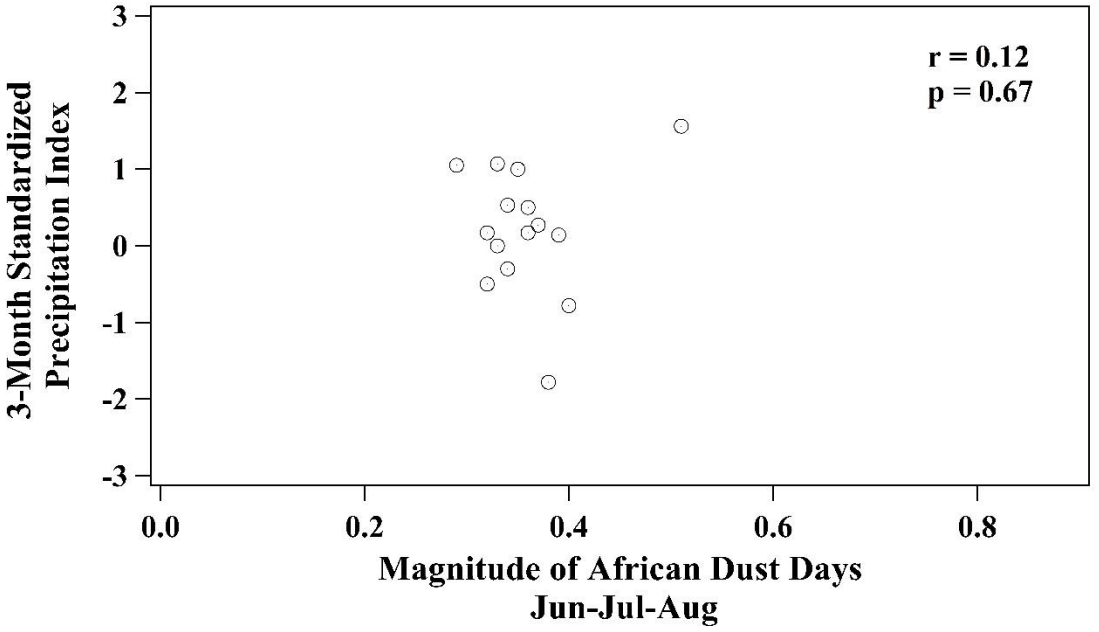

Figure D.14 Correlation between Magnitude of African Dust Days (ADD) during Jun-Jul-Aug (JJA) and its corresponding 3-month standardized precipitation index (SPI) ending in August at Lajas Substation.

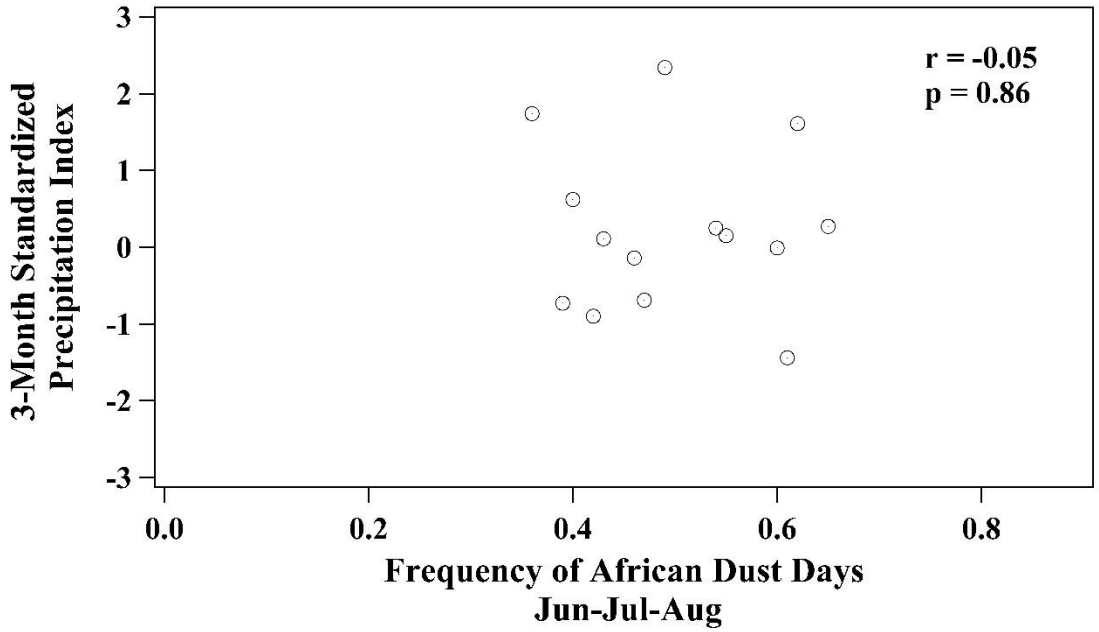

Figure D.15 Correlation between Frequency of African Dust Days (ADD) during Jun-Jul-Aug (JJA) and its corresponding 3-month standardized precipitation index (SPI) ending in August at Guayama 2E.

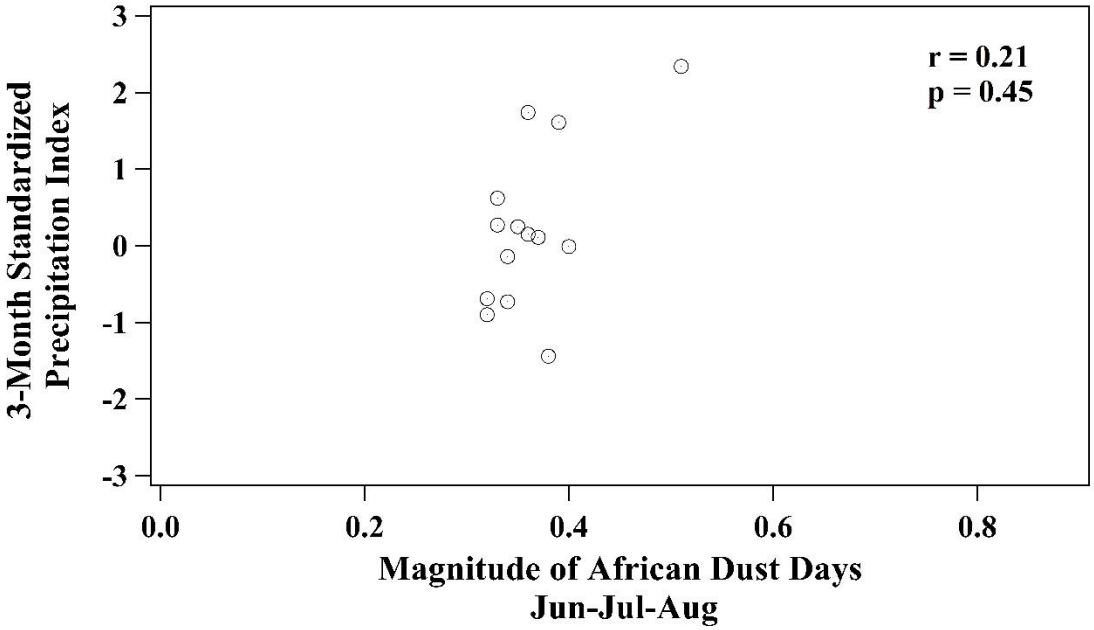

Figure D.16 Correlation between Magnitude of African Dust Days (ADD) during Jun-Jul-Aug (JJA) and its corresponding 3-month standardized precipitation index (SPI) ending in August at Guayama 2E.

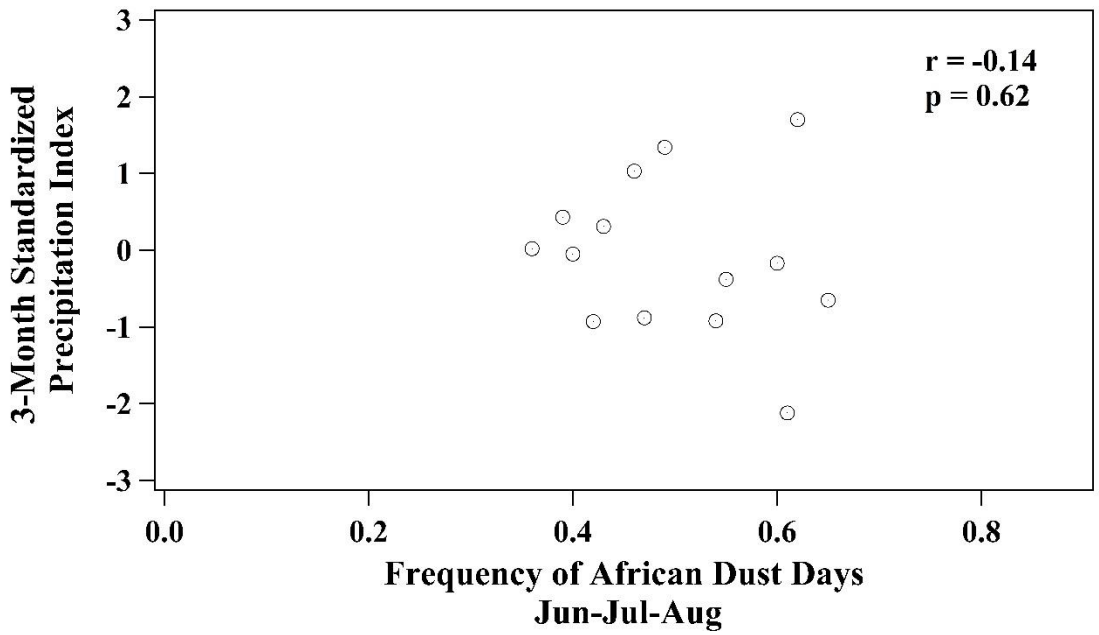

Figure D.17 Correlation between Frequency of African Dust Days (ADD) during Jun-Jul-Aug (JJA) and its corresponding 3-month standardized precipitation index (SPI) ending in August at Juncos.

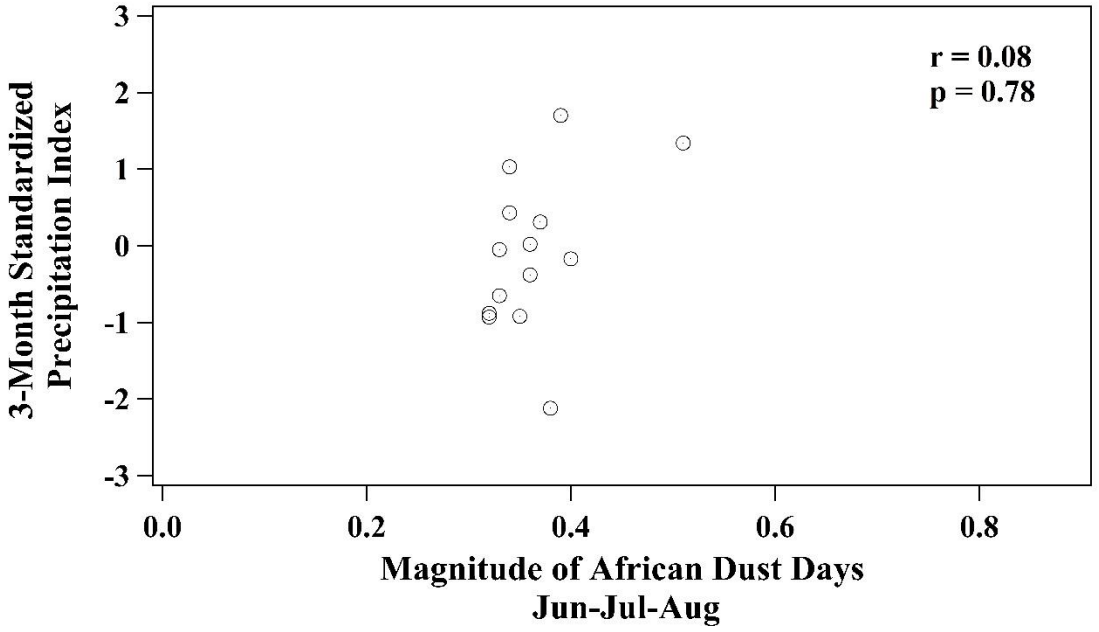

Figure D.18 Correlation between Magnitude of African Dust Days (ADD) during Jun-Jul-Aug (JJA) and its corresponding 3-month standardized precipitation index (SPI) ending in August at Juncos.

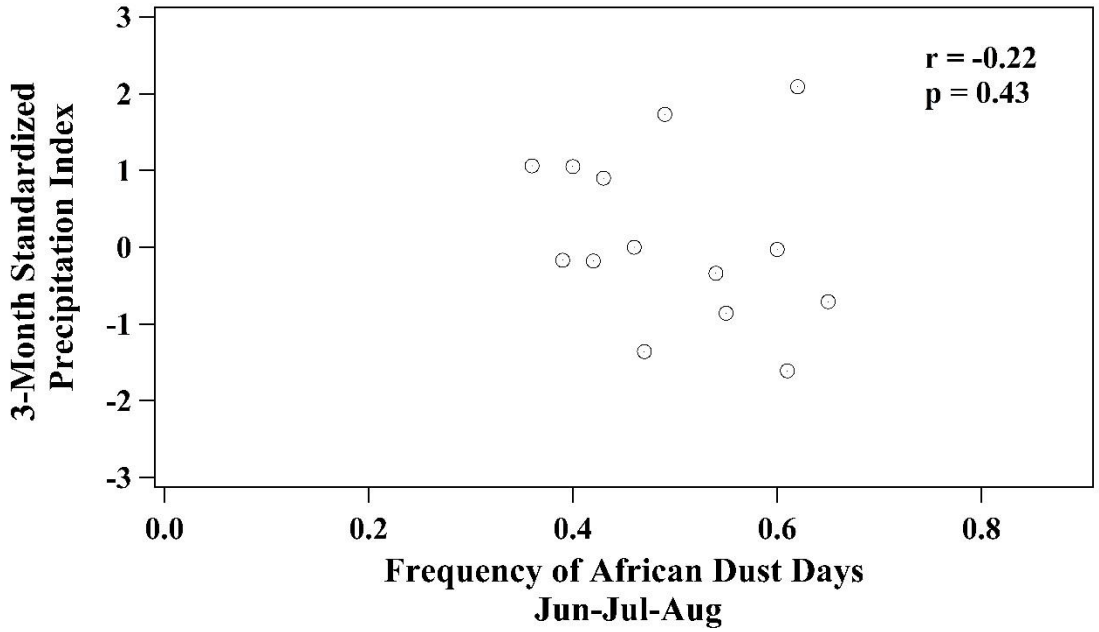

Figure D.19 Correlation between Frequency of African Dust Days (ADD) during Jun-Jul-Aug (JJA) and its corresponding 3-month standardized precipitation index (SPI) ending in August at Paraiso.

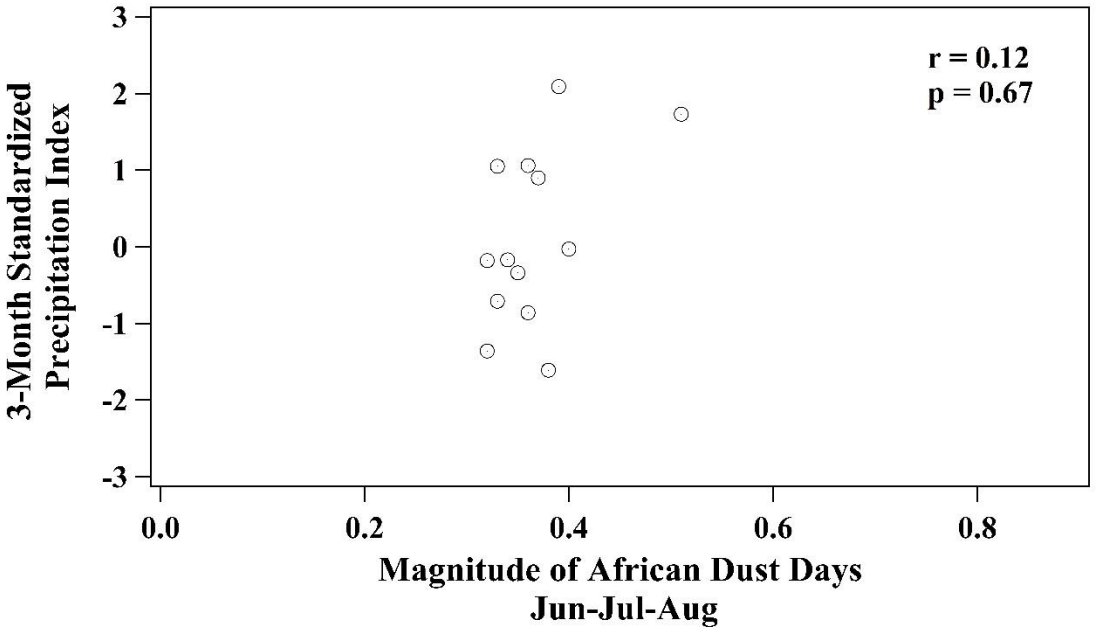

Figure D.20 Correlation between Magnitude of African Dust Days (ADD) during Jun-Jul-Aug (JJA) and its corresponding 3-month standardized precipitation index (SPI) ending in August at Paraiso.

Appendix E: Publications of Odalys Martínez-Sánchez.

Published Journal and Peer-Reviewed Articles

Martínez-Sánchez, O., Cuevas-Agulló, E., Garcia-Cabrera, R.D., Heymfield, A., & Mayol-Bracero, O.L. (2020). A conceptual model of African dust transport into the northeast Caribbean. Manuscript submitted for publication. *Journal of Applied Meteorology and Climatology*.

Gould, W.A., Díaz, E. L., Álvarez-Berríos, N. L., Aponte-González, F., Archibald, W., Bowden, J. H., Carrubba, L., Crespo, W., Fain, S. J., González, G., Goulbourne, A., Harmsen, E., Holupchinski, E., Khalyani, A. H., Kossin, J., Leinberger, A. J., Marrero-Santiago, V. I., **Martínez-Sánchez, O.**, McGinley, K., Méndez-Lázaro, P., Morell, J., Oyola, M. M., Parés-Ramos, I. K., Pulwarty, R., Sweet, W. V., Terando, A., & Torres-González, S. (2018). U.S. Caribbean. In Impacts, Risks, and Adaptation in the United States: Fourth National Climate Assessment, Volume II. U.S. Global Change Research Program, Washington, DC, USA, pp. 809–871.

Martínez-Sánchez, O. (2017). Impacts from Hurricanes Irma and Maria in the Caribbean. *Bulletin of the American Meteorological Society, 99* (8), 202.

Méndez-Lázaro, P. A., Pérez-Cardona, C. M., Rodríguez, E., **Martínez-Sánchez, O**., Taboas, M., Bocanegra, A., & Méndez-Tejeda, R. (2016). Climate change, heat, and mortality in the tropical urban area of San Juan, Puerto Rico. *International Journal of Biometeorology*, 1–9.

Méndez-Lázaro, P., **Martínez-Sánchez, O.**, Mendez-Tejeda, R., Rodriguez, E., Morales, E., & Schmitt-Cortijo, N. (2015). Extreme Heat Events in San Juan Puerto Rico: Trends and Variability of Unusual Hot Weather and its Possible Effects on Ecology and Society. *Climatology & Weather Forecasting*, *3*(135).

Puerto Rico Climate Change Council (PRCCC). (2013). In State of Puerto Rico's Climate 2010-2013. Working Group 1: Geophysical and Chemical Scientific Knowledge Observed Trends and Future Projections. Department of Natural and Environmental Resources, Office of Ocean and Coastal Resource Management (NOAA-OCRM) San Juan, P.R.

Taylor, M A., Stephenson, T., Trotman, A., Spence, J., **Martínez-Sánchez, O.**, Votaw, G., González-García, I., Pérez-Suárez, R., Lapinel-Pedroso, B., León-Lee, A., BoudetRouco, D., & González-Rodríguez, N. (2011). The Caribbean. *Bulletin of the American Meteorological Society, 93* (7), 170–173.

Published Abstracts and Presentations at National and International Conferences

Martínez-Sánchez, O., Mayol-Bracero, O.L., & Heymsfield, A. (2020). Fifteen-Year Trend in African Dust Outbreaks across the Eastern Caribbean. American Meteorology Society, 100th Annual Meeting.

Martínez-Sánchez, O., Mayol-Bracero, O.L., & Heymsfield, A. (2018). Fifteen-Year Trend in African Dust Outbreaks across the Eastern Caribbean. American Geophysical Union, AGU FALL Meeting 2018.

Martínez-Sánchez, O., Mayol-Bracero, O.L., & Heymsfield, A. (2016). Ten-year Trends in African Dust Episodes and its Effects on the Bimodal Rainfall Patterns across the Northeast Caribbean. American Meteorology Society, AMS 32nd Conference on Hurricanes and Tropical Meteorology.

Martínez-Sánchez, O., Mayol-Bracero, O.L., & Heymsfield, A. (2015). Low and mid-level tropical atmosphere characterization during African dust outbreaks using particles size distribution data retrieved from ICE-T and PRADACS. American Geophysical Union, AGU FALL Meeting 2015.